

STRUCTURE / PROPERTY / PROCESSING RELATIONSHIPS IN MOLYBDENUM  
DISILICIDE / SILICON CARBIDE COMPOSITES

BY

SETHURAMAN JAYASHANKAR

A DISSERTATION PRESENTED TO THE GRADUATE SCHOOL  
OF THE UNIVERSITY OF FLORIDA IN PARTIAL FULFILLMENT  
OF THE REQUIREMENTS FOR THE DEGREE OF  
DOCTOR OF PHILOSOPHY

UNIVERSITY OF FLORIDA

1996

Copyright 1996

by

Sethuraman Jayashankar

Dedicated to Amma and Appa  
for their endless sacrifices  
and their unwavering belief in me.

## ACKNOWLEDGEMENTS

The past few years of graduate school have been a truly enlightening experience in all facets of life, for which the author wishes to record his deep appreciation and gratitude to his chair and mentor, Prof. M. J. Kaufman, in no small measure. In addition to providing him with an opportunity to undergo the rigors of a truly interdisciplinary materials curriculum, Prof. Kaufman ensured uninterrupted financial and technical support to the author throughout the duration of his studies. Prof. Kaufman inspired the author through his friendship, his indefatigable spirit and his dedication to purpose. The author also extends his gratitude to the members of his graduate committee, Profs. Reza Abbaschian, Daniel Drucker, Fereshteh Ebrahimi, Jack Mecholsky and Ellis Verink (the "Super Six") for their unwavering commitment of their time and for the selfless dissemination of their technical wisdom and experience toward the genesis of this dissertation. Profs. Ebrahimi and Mecholsky also graciously allowed unrestricted use of their mechanical testing facilities to the author over the years. A special word of thanks is also reserved for Prof. Bhavani Sankar, who agreed to substitute for Prof. Drucker at a very short notice. The author also extends his sincere gratitude to all his fellow graduate students, past and present, who lent him a hand through the years. Special mention is made to the invaluable assistance rendered by Ms. Michelle Somerday, Dr. Kyung-Tae Hong and Dr. Zheng Chen, who patiently introduced the author to the intricacies of high temperature testing and endured his questions. The author is also indebted in no small measure to the staff of the Major Analytical Instrumentation Center, and particularly to Dr. Augusto Morrone for their cheerful attitude and for the help they have rendered him over the years. The author would also like to acknowledge Gary Scheffele for his assistance



with the thermogravimetric analysis. Mr. P.N. Vaidyanathan lent his counsel on matters worldly, and for this he is gratefully acknowledged. Thanks are also due to Ryan Kaufman, whose ever-cheerful spirit and positive outlook the author found contagious.

Friends provide a respite from the vagaries of graduate school, and here again, the author has been fortunate enough to have been blessed with a small but reliable network of fantastic individuals who provided intellectual, inspirational and spiritual support during his stay in Gainesville. Special mention must be made to Dr. Madhukar and Viji Rao, Dilip and Swapna Shinde, Rajan and Vindhya Nagabushnam and Neal Parker Jr., whose camaraderie and positive spirit proved invaluable.

The local Indian community has also provided its measure of support and understanding. Special mention is made to Profs. Ranga and Vasudha Narayan, Prof. Bhavani and Meera Sankar and Prof. Ramu Ramaswamy, who not only lent tremendous professional encouragement, but were instrumental in providing the author with a home away from home.

Last but not the least, the author is indebted to his mother and father and his sister for their endless moral support and unconditional love and affection they have extended to him throughout his life. And lastly, the author gives thanks to the Almighty for having given him the spirit, the will, the endurance, the self-confidence and the moral courage to take this endeavor to fruition.

## TABLE OF CONTENTS

ACKNOWLEDGEMENTS .....	iv
LIST OF TABLES.....	ix
LIST OF FIGURES .....	x
ABSTRACT .....	xv
INTRODUCTION .....	1
1.1 Background.....	1
1.2 Approach .....	9
LITERATURE REVIEW.....	11
2.1. Phase Equilibria.....	11
2.1.1 System Mo-Si.....	11
2.1.2 System Mo-Si-C.....	18
2.2 Issues involved in the Processing of MoSi <sub>2</sub> .....	22
2.3 Elimination of Silica.....	24
2.4 The Carbothermal Reduction of Silica.....	27
2.5 Physical Properties .....	28
2.5.1 Elastic Modulus .....	28
2.5.2 Diffusivity.....	30
2.6 Oxidation Characteristics .....	33
2.7 Mechanical Properties.....	35
2.7.1 Single Crystals.....	35
2.7.2 Polycrystals .....	37
2.7.2.1 Strength.....	37
2.7.2.2 BDDT.....	43
2.7.3 High Temperature Deformation and Creep.....	43
2.7.4 Summary of Mechanical Properties.....	47
2.8 Creep Deformation Mechanisms in Polycrystalline Materials.....	47
2.8.1 Phenomenological Equation.....	47
2.8.2 Creep Mechanisms .....	48
2.8.2.1 Lattice Mechanisms .....	48
2.8.2.2 Boundary Mechanisms .....	49
2.9 Liquid Enhanced Creep .....	50
2.9.1 Mechanisms of Liquid Enhanced Creep.....	53
2.9.1.1 Lubricated Flow (Viscous Flow).....	53
2.9.1.2 Solution Reprecipitation Creep.....	54

2.10 Superplasticity .....	56
2.10.1 Stress-Strain Rate Variations.....	57
2.10.2 Materials Considerations for Superplastic Deformation .....	57
2.10.3 Characteristics of Superplastic Deformation .....	60
2.10.4 Effect of a Second Phase on the Superplastic Deformation Characteristics .....	61
2.10.5 The Threshold Stress and Its Origin in Superplastic Materials.....	62
PROCESSING .....	65
3.1 Introduction.....	65
3.2. Background.....	67
3.2.1 Phase Equilibria.....	67
3.2.2 Processing Rationale.....	68
3.3 Experimental Procedure.....	72
3.3.1 Raw Materials .....	72
3.3.2 <i>In-situ</i> Composites.....	73
3.3.2.1 Mechanical Alloying .....	73
3.3.2.2 Thermogravimetry.....	74
3.3.2.3 Powder Consolidation.....	74
3.3.3 Conventionally Processed (CP) Composites.....	79
3.3.4 Microstructural Characterization .....	80
3.3.4.1 TEM Sample Preparation .....	81
3.4. Results and Discussion .....	81
3.4.1 <i>In-situ</i> Composites.....	81
3.4.1.1 Powder Microstructure.....	81
3.4.1.2 Phase Evolution.....	87
3.4.1.3 Consolidated Microstructures.....	93
3.4.1.4 Contamination Effects due to Milling Media.....	100
3.4.1.5 Thermogravimetric Analysis.....	102
3.4.2 Microstructural Comparisons: <i>In-situ</i> vs. Conventionally Processed MoSi <sub>2</sub> /SiC .....	104
3.4.2.1 <i>In-situ</i> Processed (UF) Composites.....	104
3.4.2.2 Conventionally Processed (CP) Composites.....	106
3.4.3 Oxygen and Carbon Analysis.....	106
3.5. Significance of the <i>In-situ</i> Reactions.....	110
3.6 Summary and Conclusion.....	112
MECHANICAL PROPERTIES.....	114
4.1 Introduction.....	114
4.2 Experimental.....	115
4.2.1 Hardness and Fracture Toughness Measurements.....	115
4.2.2 Flow Characterization.....	116
4.2.2.1 Specimen Preparation and Testing.....	117
Compression Testing .....	117
Bend Strength Measurements .....	119
4.2.2.2 Data Analysis.....	119

4.3 Results and Discussion .....	122
4.3.1 Microstructure .....	122
4.3.2 Hardness and Fracture Toughness .....	122
4.3.3 Microstructural Effects on Flow Parameters .....	129
4.3.3.1 Stress-Strain Curves .....	129
4.3.3.2 CP MoSi <sub>2</sub> /20 SiC Composites .....	130
Strain Rate Sensitivity Variations .....	132
4.3.3.3 UF MoSi <sub>2</sub> / 20 SiC Composites .....	134
4.3.3.4 UF MoSi <sub>2</sub> / 5 SiC Composites .....	135
4.3.3.5 Silica Effects on Flow Characteristics .....	137
4.3.4 Microstructural Effects on Deformation Mechanisms .....	139
4.3.4.1 UF MoSi <sub>2</sub> / 20 SiC .....	139
4.3.4.2 CP MoSi <sub>2</sub> /20 SiC .....	144
4.3.4.3 Coarse Grain-Sized Material .....	151
4.3.5 Superplastic Behavior .....	154
4.3.6 Implications of Superplastic Behavior .....	159
4.4 Application of the Flow Property Measurements to Process Development .....	162
4.5 Property Comparisons with Other Materials Systems .....	164
4.6.1 Fracture .....	171
4.6.2 Flow .....	171
CONCLUSION .....	173
APPENDIX .....	177
LIST OF REFERENCES .....	181
BIOGRAPHICAL SKETCH .....	190

## LIST OF TABLES

<u>Table</u>	<u>page</u>
2-1 Summary of the binary and ternary phases of the Mo-Si-C system.....	12
2-2 Elastic modulus of MoSi <sub>2</sub> .....	30
2-3 Short Time Tensile Strengths of MoSi <sub>2</sub> .....	41
2-4 Bend Strength of MoSi <sub>2</sub> as a Function of Temperature.....	41
2-5 Summary of creep data of MoSi <sub>2</sub> and MoSi <sub>2</sub> composites .....	44
2-6 Creep parameters for lattice mechanisms with p=0.....	49
2-7 Creep parameters for boundary mechanisms.....	51
3-1 Specifications of the raw materials used .....	72
3-2 Microstructural characteristics of the consolidated samples derived from the ternary MA MoSi <sub>2</sub> powders.....	95
3-3 Carbon and Oxygen Analysis of the Starting Powders.....	107
3-4 Oxygen Analysis of the Consolidated Microstructures.....	108
4-1 Oxygen analysis of the consolidated microstructures.....	115
4-2 Strain rates corresponding to SRS peak for the UF and CP MoSi <sub>2</sub> / 20 v/o SiC as a function of temperature .....	132

## LIST OF FIGURES

<u>Figure</u>	<u>page</u>
2-1 The Mo-Si binary diagram .....	14
2-2 Unit cell of MoSi <sub>2</sub> .....	15
2-3 Dissociation pressure of silicon over molybdenum silicides .....	17
2-4 Dissociation pressure of silicon over Mo <sub>3</sub> Si and Mo <sub>5</sub> Si <sub>3</sub> .....	17
2-5 Schematic of the ternary isotherms of the Mo-Si-C system as proposed by (a) Nowotny et al. at 1600°C and (b) van Loo et al. at 1200°C .....	19
2-6 The liquidus projection of the Mo-Si-C system showing the quasi-binary and ternary eutectics of interest .....	21
2-7 Schematic depicting the regimes of thermodynamic stability of the various phases for the carbothermal reduction of silica .....	29
2-8 Stress-strain curves of single crystal MoSi <sub>2</sub> along various crystallographic orientation .....	36
2-9 Temperature dependence of compressive strengths for different orientations of single crystal MoSi <sub>2</sub> .....	38
2-10 Short term tensile strengths of MoSi <sub>2</sub> .....	39
2-11 Yield strength of MoSi <sub>2</sub> - based materials (four-point bend tests) .....	40
2-12 Schematic representation of the typical flow characteristics of a superplastic material showing the sigmoidal flow stress- strain rate relationship .....	58
2-13 Schematic of the grain switching mechanism for superplastic material .....	63

3-1	Schematic of the hot consolidation cycle for the processing of MoSi <sub>2</sub> /SiC composites.....	77
3-2	Backscattered electron image of area of hot pressed sample from UF MoSi <sub>2</sub> /40 SiC, showing a silicon depleted surface layer. ....	78
3-3	Morphological evolution of the MA MoSi <sub>2</sub> powders as a function of milling time showing the progressive reduction in powder size and subsequent stabilization of powder size after 29 h .....	82
3-4	Structural evolution of the ternary MA MoSi <sub>2</sub> powder as a function of milling time .....	84
3-5	(a) Dark field TEM of the unannealed, as mechanically alloyed powder after 40 h milling, showing the distribution of fine crystallites of Mo, $\alpha$ - and $\beta$ -MoSi <sub>2</sub> in the micron-sized MA powder. Also note the presence of an amorphous layer surrounding the powder particle. (b) Selected area diffraction pattern from the above powder particle .....	85
3-6	XRD of the (a) MA binary stoichiometric MoSi <sub>2</sub> and (b) MA ternary MoSi <sub>2</sub> (Si-28Mo-14C) after 40 h of milling.....	86
3-7	DTA of binary stoichiometric MoSi <sub>2</sub> under flowing argon.....	88
3-8	XRD of the MA binary stoichiometric MoSi <sub>2</sub> powders heated under flowing argon.....	89
3-9	DTA of ternary MoSi <sub>2</sub> under flowing argon.....	91
3-10	XRD of the MA ternary MoSi <sub>2</sub> powders heated under flowing argon.....	92
3-11	Scanning Electron Micrograph (SEM) of the microstructure of the hot-pressed binary MA MoSi <sub>2</sub> .....	94
3-12	Bright Field Transmission Electron Micrograph (BFTEM) and SADP of silica particles in hot-pressed binary MA MoSi <sub>2</sub> .....	94
3-13	Backscattered electron image of the hot-pressed ternary MA MoSi <sub>2</sub> (Si-28Mo-14C) .....	96

3-14	(a) BFTEM of the ternary MA MoSi <sub>2</sub> . (b) SADP of $\beta$ -SiC along B=[011] (region A). (c) SADP of the Nowotny phase along B=[10 $\bar{1}$ 0] (region B).....	98
3-15	BFTEM of a $\beta$ -SiC particle formed in-situ in the ternary MA MoSi <sub>2</sub> .....	99
3-16	BFTEM of the ternary MA MoSi <sub>2</sub> showing the absence of grain boundary SiO <sub>2</sub> .....	99
3-17	X-Ray elemental maps showing location of (a) Fe (b) Si (c) Mo, along with (d) a backscattered electron image of the UF MoSi <sub>2</sub> /SiC. ....	101
3-18	TGA of binary stoichiometric MA MoSi <sub>2</sub> and ternary MA MoSi <sub>2</sub> (Si-28Mo-14C).....	103
3-19	Backscattered electron images of consolidated microstructures of UF MoSi <sub>2</sub> /SiC containing (a) 20 v/o and (b) 40 v/o SiC. ....	105
3-20	Backscattered electron images of consolidated microstructures of CP MoSi <sub>2</sub> /SiC containing (a) 20 v/o and (b) 40 v/o SiC. ....	105
4-1	SEM of the undeformed (a) UF MoSi <sub>2</sub> /20SiC (b) CP MoSi <sub>2</sub> /20SiC.....	123
4-2	Vickers hardness of the CP and UF MoSi <sub>2</sub> / SiC composites .....	124
4-3	Indentation fracture toughnesses of (a) UF and (b) CP MoSi <sub>2</sub> /SiC.....	126
4-4	Crack path arising from a Vickers indent in (a) UF MoSi <sub>2</sub> /20SiC and (b) CP MoSi <sub>2</sub> / 40SiC.....	128
4-5	(a) Flow stress variations with strain rate, CP MoSi <sub>2</sub> / 20 SiC (b) Strain rate sensitivity variations as a function of strain rate .....	131
4-6	(a) Flow stress variations with strain rate, UF MoSi <sub>2</sub> /20SiC (b) Strain rate sensitivity variations as a function of strain rate.....	133
4-7	(a) Flow stress variation with strain rate,	



	UF MoSi <sub>2</sub> / 5 SiC (b) Strain rate sensitivity variations as a function of strain rate.....	136
4-8	Comparison of the flow characteristics of the UF and CP MoSi <sub>2</sub> / 20 SiC at 1300°C.....	137
4-9	Variation of the stress exponent with temperature for MoSi <sub>2</sub> /SiC composites.....	140
4-10	Temperature dependence of strain rate for MoSi <sub>2</sub> /SiC composites.....	141
4-11	Polarized light micrographs of UF MoSi <sub>2</sub> / 20 v/o SiC (a) undeformed microstructure (b) deformed at 1300°C to $\epsilon = 0.23$ at $\dot{\epsilon} = 3.2 \times 10^{-4} \text{ s}^{-1}$ .....	143
4-12	Polarized light micrographs of CP MoSi <sub>2</sub> / 20 v/o SiC (a) undeformed microstructure (b) deformed at 1300°C to $\epsilon = 0.28$ at $\dot{\epsilon} = 1.2 \times 10^{-4} \text{ s}^{-1}$ .....	146
4-13	Polarized light micrographs of UF MoSi <sub>2</sub> / 5v/o SiC (a) undeformed microstructure (b) deformed at 1300°C to $\epsilon = 0.26$ at $\dot{\epsilon} = 4 \times 10^{-6} \text{ s}^{-1}$ .....	153
4-14	Composition-structure-flow relationships of some MoSi <sub>2</sub> /SiC materials.....	157
4-15	Temperature dependence of yield strength of MoSi <sub>2</sub> /SiC composites from four-point bend tests.....	165
4-16	Yield strength (four-point bend) comparisons of UF MoSi <sub>2</sub> / 5 SiC with other MoSi <sub>2</sub> based systems.....	166
4-17	Comparison of the yield strength of UF MoSi <sub>2</sub> /5 SiC with the Ultimate strength of competitive ceramic systems.....	167
4-18	Comparison of the creep rates of UF MoSi <sub>2</sub> / 5 SiC with other MoSi <sub>2</sub> - based materials at 1300°C.....	169
4-19	Comparison of the creep rates of UF MoSi <sub>2</sub> / 5 SiC with other ceramic systems.....	170
A-1	True stress-strain curves of strain rate change compression tests of CP MoSi <sub>2</sub> / 20 SiC at 1180°C, at nominal strain rates of $1 \times 10^{-4} \text{ s}^{-1}$ , $2 \times 10^{-4} \text{ s}^{-1}$ , $4 \times 10^{-4} \text{ s}^{-1}$ , and $8 \times 10^{-4} \text{ s}^{-1}$ .....	178

A-2	True stress-strain curves of strain rate change compression tests of UF MoSi <sub>2</sub> / 20 SiC at 1240°C, at nominal strain rates of $4 \times 10^{-5} \text{ s}^{-1}$ , $7 \times 10^{-5} \text{ s}^{-1}$ , $1.225 \times 10^{-4} \text{ s}^{-1}$ , $2.14 \times 10^{-4} \text{ s}^{-1}$ , $3.75 \times 10^{-4} \text{ s}^{-1}$ , $6.56 \times 10^{-4} \text{ s}^{-1}$ , $1.149 \times 10^{-3} \text{ s}^{-1}$ and $2.01 \times 10^{-3} \text{ s}^{-1}$ .....	179
A-3	True stress-strain curves of strain rate change compression tests of UF MoSi <sub>2</sub> / 5 SiC at 1330°C, at nominal strain rates of $2 \times 10^{-6} \text{ s}^{-1}$ , $4 \times 10^{-6} \text{ s}^{-1}$ , $8 \times 10^{-6} \text{ s}^{-1}$ , $1.6 \times 10^{-5} \text{ s}^{-1}$ and $3.2 \times 10^{-5} \text{ s}^{-1}$ .....	180

Abstract of Dissertation Presented to the Graduate School  
of the University of Florida in Partial Fulfillment of the  
Requirements for the Degree of Doctor of Philosophy

STRUCTURE/PROPERTY/PROCESSING RELATIONSHIPS IN MOLYBDENUM  
DISILICIDE/SILICON CARBIDE COMPOSITES

By

Sethuraman Jayashankar

December, 1996

Chairman: Michael J. Kaufman

Major Department: Materials Science and Engineering

The structure- processing- property relationships of  $\text{MoSi}_2/\text{SiC}$  composites is presented, with emphasis on grain size and silica effects on the ambient and elevated temperature mechanical behavior.. The program seeks to improve the properties of the silicide from considerations of formability, high temperature strength, and ambient toughness.

An innovative processing methodology was developed to synthesize near-stoichiometric, silica-free  $\text{MoSi}_2/\text{SiC}$  composites utilizing a combination of mechanical alloying and *in-situ* carbothermal reduction reactions, starting from elemental powders. Through this method, the grain size and silica content were systematically controlled for property studies. The effects of the non-wetting intergranular silica and grain size on the deformation mechanisms of  $\text{MoSi}_2/\text{SiC}$  composites were thus investigated utilizing a

combination of indentation, four point bend, single strain rate and multiple strain rate compression tests spanning the range of temperatures from ambient to 1450°C.

The silica content and the MoSi<sub>2</sub> grain size are shown to control the high temperature deformation in the temperature range of 1180-1400°C. In the grain size regimes of 5-7 μm and in the presence of the non-wetting intergranular silica phase, stress exponents of unity, activation energy decreases with increasing temperature, and retention of equiaxed microstructures through deformation are observed in MoSi<sub>2</sub>/ 20 SiC, indicating the occurrence of liquid-enhanced grain boundary sliding or viscous-sliding-aided solution-precipitation creep. For the silica-free MoSi<sub>2</sub>/SiC in a similar grain size regime, stress exponents of ~1.5 and equiaxed microstructure retention through the deformation are observed, indicating the likely occurrence of interface reaction-controlled grain boundary sliding. For silica-free MoSi<sub>2</sub>/ 5SiC with a larger grain size (~40 μm), interface-controlled grain boundary sliding operates at temperatures below 1330°C, while climb-controlled dislocation creep predominates above this temperature.

The addition of SiC weakens the high temperature strength of the material, contrary to expectations of strengthening due to their presence at the grain boundaries. The grain refinement effect and the resultant creep strength degradation due to SiC addition overweighs the potential resistance to grain boundary sliding offered by the SiC particles at the grain boundaries.

## CHAPTER I INTRODUCTION

### 1.1 Background

The quest for improvements in fuel efficiency, performance, higher strength to weight ratios and reduced direct operational costs has always led aircraft engine designers in pursuit of improved and ingenious engine designs incorporating reliable, high performance materials. While nickel-based superalloys have been the principal workhorse for high temperature structural applications for the past five decades, chiefly through alloying additions, directional solidification, and the use of single crystals, their development has advanced to the point that the operating temperature of gas turbine engines now approach the melting temperature of these alloys. Consequently, interest has focused on the development of intermetallics and ceramics for potential engine applications in the temperature range of 1000 - 1600°C. These compounds are broadly characterized by their ordered crystal structure, directional bonding, high bond strengths (due mostly to the covalent or hybrid metallic-covalent bonding) and good oxidation resistance.

Silicides of transition refractory metals such as molybdenum are a class of materials thus under scrutiny as potential structural materials. Although their high melting points, excellent environmental (oxidation and corrosion) stability, low densities and good electrical and thermal conductivity make them attractive candidate materials, their transition to commercial realization has been severely impeded, due in part to issues such as their low ambient temperature fracture toughness, poor elevated temperature

strength and the lack of suitable low-cost net-shape forming techniques. While significant efforts have been focused on the use of refractory reinforcement phases (both ceramics and refractory metals) and alloying additions in order to address the room temperature ductility and high temperature strength issues, success has been somewhat limited, due to a host of unresolved issues including those pertaining to the thermodynamic stability of some of these systems. An additional complication is the interaction of the secondary matrix phases with reinforcement systems. For example, diffusion barrier coatings in ductile fiber reinforced composites have been shown to be degraded due to attack by secondary matrix phases such as silica [Xia 92], effectively shortening the useful life. Furthermore, the compositing studies have demonstrated their ineffectiveness in preventing the drastic strength drop of these materials above 1300°C, the "reinforcing" effects of these phases notwithstanding.

Considerable uncertainty also shrouds our understanding of such material parameters as the actual brittle-ductile transition temperature<sup>@</sup> (BDTT), the precise determination of which is essential to successful component design. In contrast to conventional materials such as steels where the reported range of BDTTs are usually within 10-20°C for a given alloy composition, considerable scatter surrounds the BDTT reported for MoSi<sub>2</sub>, with values quoted anywhere in the regime from 1000°C to 1400°C. Such discrepancies are not attributable to statistical variations, and are more likely the result of a complex interplay between microstructural variables (such as the grain size and distribution and volume fraction of the intergranular silica) and the testing parameters (type of test, strain rates, test temperatures, etc.).

Processing is another area where silicides pose interesting challenges. The high melting point of MoSi<sub>2</sub>, coupled with its line-compound characteristics and relatively high vapor pressure at high temperatures, is responsible for some of the difficulties

---

<sup>@</sup> Here we acknowledge that the actual value of the BDTT may depend on how we define and experimentally determine it.

encountered. Consequently, powder-based routes have been preferred due to the potentially lower processing temperatures that they afford. However, powder processing routes are limited by the difficulties encountered in the densification of coarse powders. Moreover, a thin, native surface layer (the very characteristic which imparts the silicide with its excellent oxidation resistance) covers each powder particle, which subsequently is incorporated into the bulk body in the form of discrete intergranular pockets during consolidation. This problem is exacerbated at the smaller powder size ranges (normally preferred for powder processing), when the larger specific surface areas contribute significantly to oxygen contamination.

The role of viscous intergranular siliceous phases on the elevated temperature mechanical properties of structural ceramics such as SiC, Si<sub>3</sub>N<sub>4</sub>, Al<sub>2</sub>O<sub>3</sub>, has been a subject of continued interest and considerable study by numerous workers over the past three decades, particularly because of their softening characteristics above 1200°C. Liquid-enhanced grain boundary sliding and cavitation are among the various mechanisms by which such intergranular phases manifest their effect on the elevated temperature properties. The ambient toughness could also be degraded through the presence of discrete silica particles embedded along the grain boundaries, which could serve as potential crack nucleation sites. Thus, control and reduction of the glassy intergranular silica is essential in order to improve the ambient and high temperature properties of MoSi<sub>2</sub>.

While there has been general agreement on the debilitating effect of silica on elevated temperature properties, it has also been argued that in such ceramic materials which usually display negligible dislocation plasticity at elevated temperatures, the presence of glassy phases enhances nonlinear deformation processes and promotes substantial stable crack growth, and, hence, damage tolerance. Enhanced formability and sinterability are also considered among the beneficial effect of such phases. Deliberate additions of low melting glass phases have been found to enhance the superplastic

formability in ceramic systems such as yttria stabilized tetragonal zirconia polycrystals (Y-TZP),  $\text{ZrO}_2$ , etc.

Of possible interest is the distinction to be drawn concerning the morphology and distribution of the glassy intergranular silica phase in  $\text{MoSi}_2$ . In contrast to other ceramic materials where intergranular phases are usually known to wet the grain boundaries (near-zero angle of wetting), silica exists in  $\text{MoSi}_2$  as spheroidal inclusions at the grain boundaries and triple points. The effect of this difference in silica morphology on the deformation mechanisms is yet unclear, although prior studies have revealed considerable improvements in mechanical properties resulting from silica elimination.

The effects of silica on the mechanical properties of  $\text{MoSi}_2$  were first documented in the pioneering studies of Maxwell [Max 52] in the early fifties, when it was shown that carbon additions to a fine grained material enhanced the creep resistance, while decreasing the observed "plasticity." Recent studies by Maloy and coworkers [Mal 91] showed considerable improvement in the elevated temperature fracture toughness of carbon-modified  $\text{MoSi}_2$ . In an extensive study of  $(\text{Mo,W})\text{Si}_2/\text{SiC}$  composites to which carbon was added, Ramamurthy and coworkers [Ram 93] reported increased crack growth initiation thresholds, lowered crack growth rates, and reduced crack tip cavitation as a result of the carbon additions. Many other investigations [Sch 92, Hyn 91, Wol 94, Har 93] have examined the role of silica on the deformation of  $\text{MoSi}_2$  materials, with respect to creep and BDTT. A degree of disagreement surrounds the influence of silica on BDTT. For example, Srinivasan et al. [Sri 92] report an upward shift in the BDTT from  $1050^\circ\text{C}$  to  $1250^\circ\text{C}$  and increased yield strengths with the removal of silica in fine grained mechanically alloyed material, while Aikin et al. [Aik 92] report no difference in the BDTT ( $\sim 1400^\circ\text{C}$ ) with the presence of spheroidal silica in the material. These results suggest the influence of subtle microstructural effects in determining the properties of the silicide.



Although some effort has been expended on studies of the effect of silica on MoSi<sub>2</sub> based materials, few of these studies have dealt with comparable microstructures, i.e. similar grain size, reinforcement content, etc., so as to isolate the effects of silica. For example, addition of deoxidants (C, Al, etc.), while definitively resulting in cleaner matrices, also result in the incorporation of ternary phases. Analysis of silica effects on properties thus becomes arduous, owing not only to the yet-unknown properties of these ternary phases, but also the additional microstructural complications due to the unknown degree of grain refining effects which these phases would provide. Moreover, complexities such as liquation, volatilization, pest oxidation, etc. have been reported during the processing of such microstructurally modified materials, thereby adding to the uncertainties in stoichiometry, phase content, and the stable existence of these materials.

In view of the potential property improvements that silica-free matrices offer, it is not surprising that considerable focus has been devoted recently toward processing improvements aimed at achieving the above goal. These followed the work of Cotton et al. [Cot 91], who pointed out the occurrence of 5-10 volume percent silica particles in hot pressed MoSi<sub>2</sub> matrices (derived from arc-melted and ground powders) as an intrinsic artifact of powder processing. Several processing approaches, both traditional and novel, involving such techniques as carbothermal reductions, reactive synthesis, inert atmospheric processing, surface silica etching, hydrogen sintering, and *in-situ* reactions have been successfully implemented since; such and related techniques have been succinctly reviewed recently by Costa e Silva and Kaufman [Cos 95]. It should be noted that while these approaches have been largely successful on a laboratory scale, they are largely impracticable from the standpoint of processing bulk structural parts due to the elaborate care required for powder handling operations and the difficulties involved in scaling up of these processes.

*In-situ* reactions thus offer a potentially low-cost route to the processing of MoSi<sub>2</sub>-based composites. In contrast to conventional "blend and consolidate"

approaches of composite processing, *in-situ* reactions are potential single step processes which result in the incorporation of thermodynamically stable reinforcement phases (and diffusion barrier coatings on refractory metal fibers) during the bulk forming processes. In addition to offering the possibilities of lowering processing costs, such procedures are also amenable to the "tailored" formation of desirable elongated reinforcement morphologies such as whiskers in the matrix. The development of whisker-reinforced materials has been severely hampered in the past because of environmental considerations. Yet another advantage is the possibility of combining *in-situ* reactive approaches with well established techniques such as mechanical alloying and superplastic forming in order to tailor microstructure and properties. Finally, *in-situ* reactions also offer the versatility and luxury of close compositional control (including the possible incorporation of alloy additions) during processing. The latter attribute is critical not only with respect to the synthesis of line compounds of stoichiometric composition, but also in considering the benefits that accrue in terms of the close control of the grain size and second phase volume fractions during processing. The generic nature of such reactions also make them adaptable for extension to other systems.

Fabrication to close tolerances is yet another factor critical to the utility of a material on an economically feasible scale for aerospace applications. The rotational functional requirement of most engine components demands close tolerances not only in initial assembly, but also during subsequent use at service temperatures. Therefore, the use of near-net-shape forming techniques to form parts to within tight dimensional tolerances would greatly enhance the economic and technical viability of MoSi<sub>2</sub>.

Unfortunately, shape-forming of MoSi<sub>2</sub> also poses significant challenges in view of its hard and brittle nature at room temperature. The resultant poor machinability limits the room temperature shape forming of MoSi<sub>2</sub> to such processes as grinding and polishing, which, in addition to being expensive and time consuming, result in

considerable wastage of expensive material, thereby increasing production costs and hindering large volume production.

While a variety of conventional shape-forming processes such as sintering, chemical vapor infiltration, liquid metal reactive infiltration and injection molding, have been utilized in the fabrication of  $\text{MoSi}_2$  bodies, these processes each have their intrinsic limitations, such as post-sintering shrinkage (sintering), potentially explosive processing atmospheres (hydrogen sintering), presence of residual silicon phases in the microstructure (liquid metal infiltration), slow deposition rates (CVD) and inefficient binder burnout (injection molding).

In view of the difficulties experienced in the traditional ceramic processing routes, traditional plastic deformation processes offer an attractive, low-cost alternative to the net shape manufacture of  $\text{MoSi}_2$ , due in part to its ductile deformation characteristics above  $\sim 1200^\circ\text{C}$ . Such processes offer possibilities of drastic reduction in the production costs, while simultaneously enabling scaleup of  $\text{MoSi}_2$  components for use in structural applications.

The phenomenon of intermetallic and ceramic superplasticity has been under investigation for the past ten years. As in metallic materials, it is also possible to shape ceramics and intermetallics by initially deriving materials comprising fine grain structures and subsequently deforming them under controlled conditions of strain rate and temperature, thereby utilizing their favorable (superplastic) deformation characteristics. Such deformation occurs at stress levels far lower than the usual yield points (in coarse grained material) without the instabilities associated with necking. Thus, large, uniform, crack-free deformations (of the order of several hundred percent) can be obtained as a result.

Low stress, high ductility-imparting superplastic deformation operations such as the "Gatorizing" process have been successfully used in the past for the production of high strength superalloy forgings having complex configurations and close tolerances

through a judicious combination of deformation processing and post deformation grain growth heat treatments. However, the work-hardening characteristic of  $\text{MoSi}_2$  makes shape-forming impracticable. While desirable from service considerations, work hardening is detrimental from a processing standpoint since it implies increasing resistance to deformation. The problem is exacerbated considering that the deformation processing of the silicide is usually in the regime of  $1250^\circ\text{C}$  and above, where the choice of die and plunger tooling materials is restricted and expensive with an increase in the operating stress levels of the forming presses. Furthermore, work hardening also increases the fracture tendency of the body with increasing strain levels, thereby limiting the extent of deformation imparted in the forming operation. Furthermore, plastic instabilities (necking) may occur during the deformation process and limit the useful attainable strains.

The design criteria for high temperature structural components, to which structural materials in general and  $\text{MoSi}_2$  in particular have specific relevance, require the use of alloys that maintain a high degree of strength at high temperature, in addition to oxidation resistance. Unfortunately, the very improvements in the service properties that are required of these materials are most easily achieved at the expense of alloy fabricability. For instance, substantial difficulties, as encountered during the sintering of high strength borides and carbides, have been attributed to their covalent-bond characteristics, which, while causing enhanced resistance to deformation, also restrict diffusion, so essential for the sintering operation. Fabrication of such bodies has thus been traditionally performed under conditions of high temperature and pressure, which increase the processing costs. Likewise, conventional casting routes, while generally providing the large grain sizes desirable for high temperature use, are unsuitable for high melting materials due to problems of crucible-melt interactions (in addition to lack of suitable containment materials) and the ubiquitous segregation problems. In addition, volatilization of certain elemental components is also frequently encountered while melting these materials. Powder routes, as discussed earlier, are also constrained by

densification problems, especially at coarser starting powder sizes. The primary reason is that the governing mechanisms for strengthening are the same as those of deformation in the service and processing temperature regimes. Such difficulties in processing seriously hinder the development of viable structural materials due to unfavorable economics involved in their processing.

## 1.2 Approach

The foregoing discussion thus tends to lead us to the conclusion that successful realization of  $\text{MoSi}_2$  based materials are possible only if significant improvements in high temperature strength and ambient fracture toughness are achieved, along with the development of cost effective processing strategies. Furthermore, it is also clear that various aspects of room and elevated temperature deformation such as the strength, BDTT and the creep mechanisms are significantly influenced not only by the presence and distribution of the intergranular phase, but also by the grain size and its distribution. Successful materials development and property enhancements, either through compositing, alloying or other approaches, are possible only through a sound understanding of the processing-structure-property relationships.

Accordingly, this investigation has focused on the following objectives:

- (1) Development of a processing rationale(s) to synthesize silica-free, near stoichiometric  $\text{MoSi}_2/\text{SiC}$  composites, using *in-situ* reactions, to transform the glassy silica phase to stable crystalline phases. Additionally, (2) develop a methodology to vary the volume fraction of reinforcement and develop a rationale for systematically varying the grain size in such composites. (Chapter III)
- (3) Elucidate the influence of the chief microstructural parameters, (silica content and the grain size) on the ambient and elevated temperature deformation (Chapter IV), and,

(4) Utilize the understanding gleaned from the results of steps 1, 2 and 3 as part of an iterative materials development effort to address the strength, toughness, and formability challenges, to provide a viable method to process "performance capable" materials.

## CHAPTER 2 LITERATURE REVIEW

In the following sections, literature pertaining to the various physical, chemical, and mechanical properties of molybdenum disilicide, forming the bulwark to the contents of Chapters 3 and 4, is reviewed.

### 2.1. Phase Equilibria

#### 2.1.1 System Mo-Si

The Mo-Si binary diagram is shown in Fig. 2-1, and relevant structural information is provided in Table 2-1. Three intermetallic compounds,  $\text{Mo}_3\text{Si}$ ,  $\text{Mo}_5\text{Si}_3$ , and  $\text{MoSi}_2$  exist, as do three eutectics, between Mo and  $\text{Mo}_5\text{Si}_3$  (2025°C),  $\text{Mo}_5\text{Si}_3$  and  $\text{MoSi}_2$  (1900°C) and between  $\text{MoSi}_2$  and Si (1414°C) [91 Gok].  $\text{MoSi}_2$  crystallizes into the  $\text{C11}_b$  (tetragonal) structure (Fig. 2-2), which is a long period ordered structure derived by stacking up three b.c.c. lattices and then compressing them along their long period axes, thereby leading to a c/a ratio significantly smaller than 3. The lattice parameters are  $a = 0.3205$  nm and  $c = 0.7845$  nm with  $c/a = 2.452$ . Of interest is the narrow range of stabilities of the disilicide (2.5 % Si maximum at 1500°C, according to Nechiporenko and coworkers [Nec 73]). Until recently, it was believed that  $\text{MoSi}_2$  exhibits the tetragonal  $\text{C11}_b$  structure below ~2173 K and the hexagonal  $\text{C40}$  structure between 2173 K and its melting temperature of around 2300 K. Two recent ternary equilibria studies [Fra 91; Boe 92] by the Perepezko and Boettinger groups, however, counter this possibility and lend credence to the notion that the  $\text{C11}_b$  structure is maintained to melting. Specifically,

Table 2.1 Summary of the Binary and Ternary Phases of the Mo-Si-C System

System	Formula	Temperature (°C)	Crystal System	Structure	Lattice Parameters (nm)	Reference	Comments
Mo-Si	Mo <sub>3</sub> Si	2025	Cubic	Pm $\bar{3}$ n	a = 0.4890	[Gok 91]	Forms by peritectic reaction, L + $\alpha$ = Mo <sub>3</sub> Si.
	Mo <sub>5</sub> Si <sub>3</sub>	2100	Tetragonal	I4/mcm	a = 0.9648 c = 0.4910	[Gok 91]	Incorrectly identified as Mo <sub>3</sub> Si <sub>2</sub> until Aronsson [Aro 55]. Solubility range ~3 at. %.
	$\alpha$ -MoSi <sub>2</sub>	1900	Tetragonal	I4/mmm	a = 0.3202 c = 0.7843	[Gok 91]	$\alpha$ - $\beta$ transformation is polymorphic. However, [Bre 80] considers $\beta$ decomposition to $\alpha$ and Mo <sub>5</sub> Si <sub>3</sub> through a eutectoidal reaction. $\beta$ may be stabilized by impurities.
	$\beta$ -MoSi <sub>2</sub>	2020	Hexagonal	P6 <sub>3</sub> 22	a = 0.4642 c = 0.6529	[Gok 91]	
Si-C	$\alpha$ -SiC	-2800	Hexagonal	P6 <sub>3</sub> mc	a = 0.3081 c = 1.511	[Vil 85]	Numerous other polytypes exist.
	$\beta$ -SiC	-2800	Cubic	F $\bar{4}$ 3 m	a = 0.4358	[Vil 85]	
	MoC	2650	Hexagonal	P6 <sub>3</sub> /mmc	a = 0.2932 c = 1.097	[Now 54]	
Mo-C	$\beta$ -Mo <sub>2</sub> C	2520	Hexagonal	P6 <sub>3</sub> /mmc	a = 0.3006 c = 0.4753	[Vil 85]	Forms by the peritectic reaction, L + MoC = Mo <sub>2</sub> C.
							Other metastable forms which are slightly carbon rich such as $\alpha$ - and $\eta$ -carbides exist at high temperatures and transform at lower temperature by eutectoid reaction to $\beta$ -Mo <sub>2</sub> C + C.



Table 2.1 - (continued)

System	Formula	Temperature (°C)	Crystal System	Structure	Lattice Parameters (nm)	Reference	Comments
Mo-Si-C	$C_{\leq 1}Mo_{\leq 5}Si_3$	2000-2060 (composition dependant)	Hexagonal	P6 <sub>3</sub> /mcm	a = 0.7286 b = 0.7287 c = 0.5002	[Par 65]	c/a changes slightly with carbon content. First structure determination made by Schachner et al. [Sch 54], but incorrectly identified as Mo <sub>5</sub> Si <sub>3</sub> .

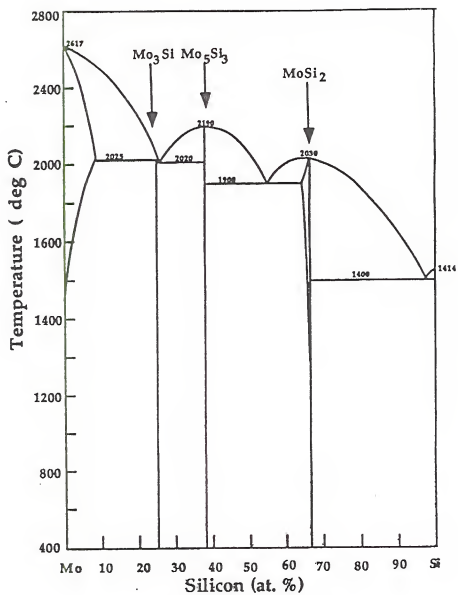
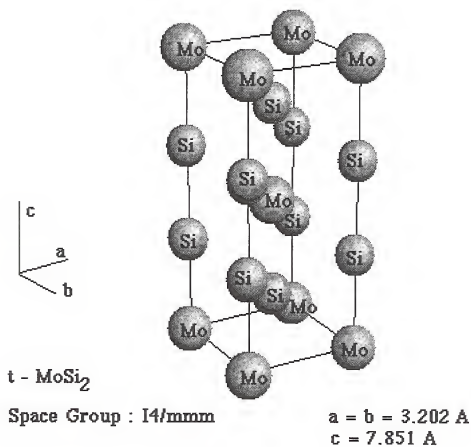
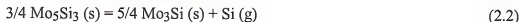
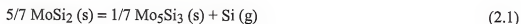


Figure 2-1 The Mo-Si binary diagram [Gok 91]

Figure 2-2 Unit cell of MoSi<sub>2</sub>

the analysis of their experimentally determined MoSi<sub>2</sub>-TiSi<sub>2</sub> quasi-binary diagram and the solidification paths clearly indicates the absence of the C11<sub>b</sub> - C40 polymorphic transformation in pure MoSi<sub>2</sub>. The earlier observations of the C40 structure are then ascribed to the presence of impurities .

All molybdenum silicides exhibit relatively high vapor pressures at high temperatures. Under conditions which exist under dynamic vacuum and high temperatures, the silicide decomposes to the next lower silicide through the following series of reactions:



and



with heats of reaction of  $117.2 \pm 0.6$  KCal,  $131.1 \pm 0.7$ , and  $131.9 \pm 1.2$  KCal, respectively. The dissociation pressures of silicon over MoSi<sub>2</sub>, Mo<sub>5</sub>Si<sub>3</sub>, and Mo<sub>3</sub>Si, corresponding to the above reactions were measured by Searcy and Tharp [Sea 60] using the Knudsen effusion method in the range of temperatures from 1900 K to 2300 K (1627°C to 2027°C); the results of these measurements are summarized in Figs. 2-3 and 2-4. Of particular interest are the measurements pertaining to MoSi<sub>2</sub>, which indicate that the disilicide exhibits dissociation pressures at least an order of magnitude higher than Mo<sub>5</sub>Si<sub>3</sub> or Mo<sub>3</sub>Si, as shown in Fig. 2-4. As will be shown later in Chapter 3, high vapor pressures result in silicon depletion from the sample surface and consequent weight losses, in addition to the establishment of a silicon gradient in the sample (high silicon in the interior to low silicon in the exterior) at high temperatures under dynamic vacuum.

At this stage, attention is also drawn to the isomorphous and miscible compound, WSi<sub>2</sub>, which exhibits a slightly higher melting point and higher density than MoSi<sub>2</sub>; WSi<sub>2</sub> has been the focus of the alloying efforts of some investigators as a potential high temperature strengthener [Sch 92].

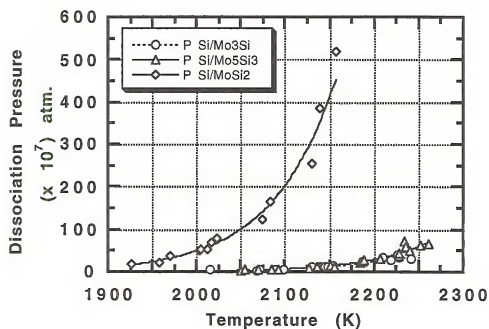


Figure 2-3 Dissociation pressure of silicon over molybdenum silicides

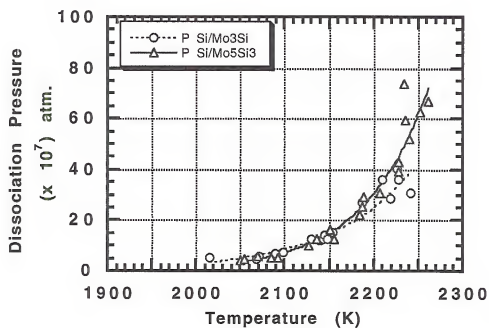


Figure 2-4 Dissociation pressure of silicon over  $\text{Mo}_3\text{Si}$  and  $\text{Mo}_5\text{Si}_3$

Of the three silicides in the Mo-Si system,  $\text{MoSi}_2$  is best suited for high temperature applications because of its superior resistance to oxidation, relatively low densities (6.21 g/cc) and high melting point (2020°C). These characteristics have enabled the extensive use of  $\text{MoSi}_2$  in heating elements.

$\text{MoSi}_2$  also finds application as an interconnect material in semiconductor devices.

### 2.1.2 System Mo-Si-C

A concise description of the phase equilibria and crystal chemistry of the Mo-Si-C system can be found in Table 2-1. While numerous phase relationship studies have been conducted over the last 50 years on this system in view of its technical and engineering importance, unfortunately, many of the earlier thermodynamic and structural determinations of the binary and ternary phase diagrams in this system were plagued by oxygen and carbon contamination as well as the high melting points of the compounds.

Ternary isotherms of the Mo-Si-C system, as shown in Fig. 2-5a, were constructed by Nowotny and co-workers [Now 54] through the use of powder sintering techniques at 1600°C and by Brewer and Krikorian [Bre 56] at around 1727°C. Subsequently, Van Loo and co-workers [Van 82] constructed a 1200°C isotherm (see Fig. 2-5b) after examining arc melted alloys and diffusion couples. The only ternary phase in the Mo-Si-C system is the "Nowotny phase" which has the approximate formula  $\text{C}_{\leq 1}\text{Mo}_{\leq 5}\text{Si}_3$  and a relatively wide homogeneity range [Now 54, Par 65, Bre 56, Van 82]. Minor amounts of carbon additions to  $\text{Mo}_5\text{Si}_3$  destabilize its tetragonal structure and result in the formation of a carbon stabilized hexagonal Nowotny phase. Nowotny phases of this type have the general formula,  $\text{T}^{\text{I}}_3\text{T}^{\text{II}}_{<2}\text{M}_3\text{X}_{<1}$ , where T denotes a

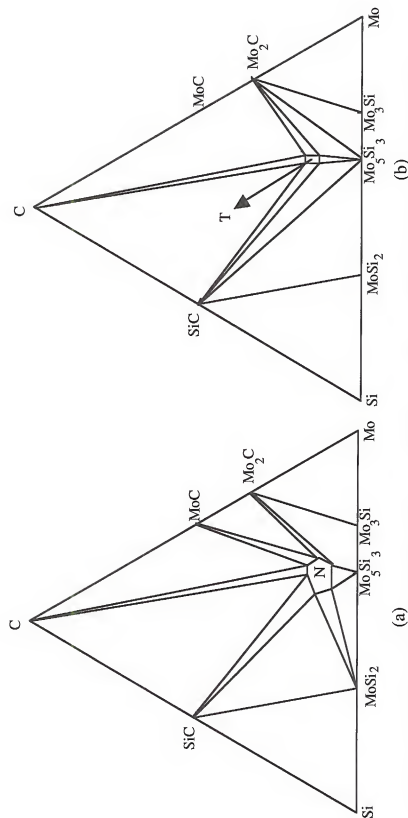


Figure 2-5 Schematic of the ternary isotherms of the Mo-Si-C system as proposed by : (a) Nowotny et al. [Now 54] at 1600°C (b) van Loo et al. at 1200°C [Van 82] (N in Fig. 2-5a and T in Fig. 2-5b denote the  $\text{C}_1$ ,  $\text{Mo}_5\text{Si}_3$  phase)

transition metal, M represents Ge or Si, and X denotes a non metal such as C, O, B or N [Par 65]. The presence of carbon-centered tetrahedra is characteristic of the Nowotny phases and accounts for their stability.

Examination of the phase relationship data reveals that these isotherms are in general agreement except in the region whose composition range is delimited by  $\text{MoSi}_2$ ,  $\text{SiC}$ ,  $\text{Mo}_5\text{Si}_3$  and  $\text{C}_{\leq 1}\text{Mo}_{\leq 5}\text{Si}_3$ . Specifically, while the isotherms of Nowotny et al. and Brewer et al. are in good agreement with each other in their prediction of the existence of a three-phase field between  $\text{MoSi}_2$ ,  $\text{C}_{\leq 1}\text{Mo}_{\leq 5}\text{Si}_3$  and  $\text{SiC}$ , the results of Van Loo indicate the coexistence of  $\text{Mo}_5\text{Si}_3$ ,  $\text{SiC}$ , and  $\text{C}_{\leq 1}\text{Mo}_{\leq 5}\text{Si}_3$  at  $1200^\circ\text{C}$ . Attention is also drawn to two aspects: (a) the Nowotny isotherm represents the existence of  $\text{MoC}$  at  $1600^\circ\text{C}$  in contradiction to the presently accepted Mo-C diagram and (b) the currently accepted  $\text{Mo}_5\text{Si}_3$  phase has been represented as  $\text{Mo}_3\text{Si}_2$ . Recently, it has been postulated by Costa e Silva [Cos 94] that the Van Loo and Brewer isotherms are consistent with each other only if a Class II, 4-phase reaction isotherm\* ( $\text{MoSi}_2 + \text{C}_{\leq 1}\text{Mo}_{\leq 5}\text{Si}_3$  (Nowotny)  $\rightarrow$   $\text{SiC} + \text{Mo}_5\text{Si}_3$ ) exists between the temperatures at which these isotherms were constructed, i.e.  $1200^\circ\text{C}$  and  $1727^\circ\text{C}$ .

Of considerable consequence are the liquidus surface projections (Fig. 2-6) for the ternary alloys, the earliest estimates of which were performed by Nowotny and coworkers [Now 54]. Attention is drawn to the ternary eutectic  $E_1$  between  $\text{MoSi}_2$ ,  $\text{C}_{\leq 1}\text{Mo}_{\leq 5}\text{Si}_3$  and  $\text{SiC}$  at  $1850^\circ\text{C}$ , the significance of which will be elaborated in the following Chapter. In addition, the reader is also referred to the quasi-binary eutectic reaction between  $\text{MoSi}_2$  and  $\text{SiC}$  at the liquidus valley at  $1900^\circ\text{C}$ . A ternary liquid

---

\* A class II, four phase equilibrium, according to Rhines's nomenclature, is generally represented by a reaction of the type  $\alpha + \beta = \gamma + \delta$ . For detailed description on ternary equilibria, see Rhines's treatment of phase equilibria [F.N. Rhines, Phase Diagrams in Metallurgy - Their Development and Application, 1956, McGraw-Hill, New York].





corresponding to this composition would freeze naturally into a mixture of  $\text{MoSi}_2$  and  $\text{SiC}$  phases.

## 2.2 Issues involved in the Processing of $\text{MoSi}_2$

Processing of silicides pose interesting challenges. The high melting point, coupled with their line compound characteristics and relatively high vapor pressure at high temperatures, is responsible for some of the difficulties encountered. Thus, conventional casting routes, while generally desired in view of their economy and net-shape capabilities and the potential for providing the large grain sizes desirable for high temperature use, are largely unsuitable due to problems of crucible-melt interactions at high temperatures and the ubiquitous segregation problems. In addition, the high vapor pressures also cause volatilization of certain elemental components and resultant deviations from stoichiometry. In view of the line-compound characteristics, such deviations cause significant microstructural changes and are generally avoided if possible, at least on the silicon-rich side, where the presence of the low melting  $\text{MoSi}_2$ -Si eutectic could degrade the high temperature strength. Consequently, considerable care has to be exercised while processing, with frequent resort to educated jugglery of starting compositions to arrive at the single phase microstructure [Ros 95].

Consequently, powder-based routes such as sintering, hot-pressing, HIPping, and reactive sintering have been preferred due to the potentially lower processing temperatures that they afford, in addition to the potentially tight stoichiometric control that they provide. More novel routes such as liquid metal infiltration, chemical vapor deposition and plasma spraying have also been studied to synthesize  $\text{MoSi}_2$  and  $\text{MoSi}_2$  based composites.

However, powder processing routes pose some interesting challenges, due in part to the high specific area characteristics of the powders. Specifically, a thin native surface layer is formed on the powder particle surface due to the very characteristics which

impart the silicide with its excellent oxidation resistance. Subsequent powder consolidation operations result in the incorporation of silica into the bulk body. In addition to contributing to the presence of a low melting silica phase in the microstructure, surface oxidation also causes overall compositional shifts towards the silicon-lean side with the resultant formation of the  $\text{Mo}_5\text{Si}_3$  phase, whose mechanical properties are not well known [Ant 91]. Such compositional shifts have also been shown to affect the intermediate temperature oxidation resistance of the silicide [Mes 92]. The powder surface oxide problem is exacerbated at the smaller powder size ranges which are normally preferred in powder processing in view of their larger specific surface areas. While an increase in the powder particle size (coarser powders) would seem to alleviate the level of oxide contamination, this approach is perilous because larger powders are notoriously difficult to sinter and hot-press to full density. This is due in part to their poor green packing characteristics and the fact that these processes largely rely on surface diffusion mechanisms for material redistribution in the compacted body.

The occurrence of silica in powder-processed  $\text{MoSi}_2$  was first discussed by Maxwell [Max 49, Max 52a, Max 52b], who devised methods of its elimination. The influence of the powder size, oxygen content, and processing conditions on the volume fraction of silica and the mechanical properties has been documented in early reports by Long [Lon 50], Fitzer [Fit 55], and Maxwell [Max 49]. The intrinsic presence of the silica as a powder processing artifact was confirmed by Cotton and coworkers [Cot 91], who reported 5-10 v/o silica in arc-melted and ground hot pressed samples. Subsequent investigations, while concurring with the presence of silica, differ in the nature of its morphological presence, with some groups claiming that it wets the grain boundaries (low  $\text{MoSi}_2$ -silica interfacial energy) and thus exists as a continuous film, while others report its existence as discrete particles along grain boundaries and triple points (non wetting characteristics due to high  $\text{MoSi}_2$ - $\text{SiO}_2$  interfacial energy). However, recent Auger analysis of *in-situ* fractured  $\text{MoSi}_2$  specimens by Costa e Silva et. al [Cos 95] show the

absence of oxygen enrichment along grain boundaries, thereby lending credence to the evidence of its globular existence. This was supported by earlier TEM observations [Jay 92].

Regardless of its morphology, the presence of silica is thought to be detrimental, since discrete particles may serve as crack nucleation sites at lower temperatures and thus degrade fracture toughness, while continuous silica films could enhance high temperature deformation ( $T > 1200^{\circ}\text{C}$ ) via grain boundary sliding when the silica softens appreciably. These aspects are reviewed in section 2-9. Finally, silica has also been reported to cause the degradation of the diffusion barrier coatings at the fiber-matrix interface in ductile fiber reinforced  $\text{MoSi}_2$  [Xia 92]

There have been arguments supporting the beneficial effects of silica as well. For instance, in ceramic materials which usually display negligible dislocation plasticity at elevated temperatures, the presence of glassy phases is believed to enhance nonlinear deformation processes and promote substantial stable crack growth and, hence, damage tolerance. Enhanced formability and sinterability due to viscous flow are also the resultant beneficial effects of siliceous phases.

### 2.3 Elimination of Silica

In view of the need to produce clean matrices, it is not surprising that considerable efforts have been focused toward processing low silica  $\text{MoSi}_2$ . These approaches can be broadly classified as (a) passive and (b) reactive silica elimination approaches.

"Passive processing" approaches to silica elimination, as the name implies, seek to minimize the oxygen content of the matrix through the use of controlled atmospheres during processing and the use of clean starting materials.

"Active (or reactive) processing" approaches use a host of chemical reactions, either at the powder surface prior to consolidation, or inside the compact during the sintering or consolidation operation, to minimize the oxygen content. Examples of active

processing include reactive synthesis, surface etching, hydrogen sintering, carbothermal reduction, and *in-situ* deoxidization. Some processes combine both active and passive approaches as will be described below.

Surface etching of the powders by NaOH or HF followed by hot consolidation has been advocated by Maxwell [Max 49, Max 52a] and Long [Lon 50]. However, the method suffers from an important drawback in that the post-etched powders need considerable care while handling and consolidation in view of their oxidation-susceptible surface characteristics. In addition to needing protective atmospheres, surface etching techniques are also plagued by environmental concerns involving the handling, storage and disposal of the caustic reagents.

Hydrogen sintering of MoSi<sub>2</sub> powders was employed by Fitzer and coworkers, who reported significant reductions in the silica content of the sintered products, especially in the finer powder size ranges. Hydrogen sintering results in faster sintering rates, perhaps as the result of the elimination of the surface silica in the powders. However, the potentially explosive atmospheres required by this process pose serious safety considerations that inhibit the scaleup of this process.

Hardwick and coworkers [Har 92] processed oxygen-free MoSi<sub>2</sub> by the reactive HIPping of high purity elemental powders, wherein all the powder handling and consolidation operations (such as powder blending, transfer to CIP bags, green compact turning, etc.) were conducted under vacuum or inert atmospheres. The lowest reported oxygen content in materials derived through their process was 0.16 wt. %. In a similar study, Srinivasan and Schwarz [Sch 92] used inert atmospheric handling methods in conjunction with mechanical alloying and hot pressing to synthesize MoSi<sub>2</sub>; they reported oxygen contents of 310 ppm wt. % for their best material.

Carbon additions have long been explored as a route to synthesize high strength MoSi<sub>2</sub>, starting with the pioneering efforts of Maxwell in the early fifties. In attempting to control the oxygen content of MoSi<sub>2</sub> by varying the starting powder size and carbon

additions to the  $\text{MoSi}_2$  powder, Maxwell found that a fine grained material with carbon additions had better creep properties and lower high temperature plasticity than a similar grain size material without carbon. As a result, Maxwell [Max 52a] reported reductions in the oxygen content of his material from 1.4 wt. % (no carbon added) to 0.15 wt. % (with carbon added). However, an increase in the porosity of the samples was observed in the carbon modified samples. More recent work along the same lines (i.e., carbon additions to  $\text{MoSi}_2$  powders) by Maloy and coworkers [Mal 91] also resulted in low silica material with improved elevated temperature fracture properties. However, severe weight losses of up to 40 wt. % leading to microstructures with indeterminate phase content were reported by these authors. While some of the weight losses were initially ascribed to volatile species such as  $\text{SiO}$  and deoxidization products such as  $\text{CO}$  and  $\text{CO}_2$ , subsequent analysis of their results by Jacobson and coworkers [Jac 93] has suggested that the weight losses could be due to the formation and consequent loss from the hot pressing dies of a eutectic liquid between  $\text{MoSi}_2$ ,  $\text{SiC}$  and  $\text{C}_{\leq 1}\text{Mo}_{\leq 5}\text{Si}_3$  at the high hot pressing temperatures ( $\sim 1850^\circ\text{C}$ ).

As an alternative processing route in the Mo-Si-C system, Henager and coworkers utilized an *in-situ* reaction scheme to synthesize  $\text{MoSi}_2$ -SiC composites starting from  $\text{Mo}_2\text{C}$  and elemental Si [Hen 92, Hen 93, Hen 95]. While particulate and elongated plate like reinforcement morphologies were obtained, this approach is constrained by the fixed volume fraction of SiC reinforcement obtainable, in view of the participation of only 2 components in the determination of the stoichiometry of the displacement reaction. For the Mo-Si-C system, this corresponds to volume fractions of 30 v/o, for which equilibrium grain sizes are in the range of 1  $\mu\text{m}$ . Such fine grain sized microstructures are desirable from formability considerations but possess inadequate creep strength for high temperature applications, the primary reason for their development. Attempts to have greater latitude in the control of compositions through the use of an additional reactant (carbon) resulted in the production of porous, finer grained bodies, with compositions

farther inside the three phase field delimited by  $\text{MoSi}_2$ ,  $\text{C} \leq \text{Mo} \leq \text{Si}_3$  and  $\text{SiC}$ . [Hen 93; Hen 95]. Furthermore, the fracture toughness was degraded through such carbon additions.

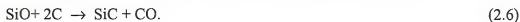
The use of *in-situ* reactions to effect a host of microstructural modifications in  $\text{MoSi}_2$  materials was demonstrated by Costa e Silva and Kaufman [Cos 95]. In their study, they pointed out the feasibility of utilizing not only carbon, but a plethora of stable oxide-forming elements (stable with respect to silica) such as aluminum, zirconium, calcium, magnesium and the rare earths to synthesize silica-free microstructures with the *in-situ* formed stable reinforcing phases derived from the silica. An added advantage that such *in-situ* reactions offer is the unique opportunity for phase modification. For instance, it was demonstrated that aluminum additions, while reducing the silica to alumina, also resulted in the modification of the  $\text{C11b}$  silicide to the  $\text{C40}$  alumino-silicide. Yet another advantage offered by such *in-situ* schemes is the ability to form protective diffusion barrier coatings on metal fibers embedded in the matrix. A similar procedure was employed by Gibala and coworkers [Gib 92], who incorporated erbium additions to arc-melted  $\text{MoSi}_2$ - $\text{Mo}_5\text{Si}_3$  composites with the aim of silica elimination and microstructural refinement.

#### 2.4 The Carbothermal Reduction of Silica

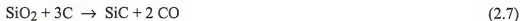
The carbothermal reduction of silica to  $\text{SiC}$  is a multistep reaction that is described by the following sequence [Ish 90, Wei 83]:



followed by the reaction of silicon monoxide to form silicon carbide, i.e.,



The overall reaction is



Reaction (2.7) has a standard free energy change  $\Delta G^0_T$  [Wei 83] which varies with temperature as

$$\Delta G^0_T = 609.023 - 0.351T \text{ kJ/mol}$$

The reaction is schematically represented in Fig. 2-7 and the regions of stability of the various phases are also indicated [Ish 90].

The energetics of reaction (2.4) suggest that it is feasible above 1700K under atmospheric pressures. By the definition of the free energies, any change in the total pressure of the system would shift the equilibrium either towards SiC formation or SiO<sub>2</sub> retention. Ishizaki [Ish 90] has shown that a lowering of the oxygen partial pressures and/or a reducing environment (conditions that typically exist during vacuum hot pressing using graphite dies) lower the reaction temperatures. Reaction (2.7) also shows that two out of every three reacting carbon atoms are gasified and are converted to CO. Therefore, the consolidation sequences during powder processing should be chosen so as to allow the product gases to escape in order to achieve full densification with no porosity.

## 2.5 Physical Properties

### 2.5.1 Elastic Modulus

The elastic modulus data of polycrystalline MoSi<sub>2</sub> are summarized in Table 2-2. The single crystal elastic constants have also been recently evaluated using the pulse-echo overlap technique [Nak 90]. The elastic properties are anisotropic, with the Young's modulus along the [001] orientation being higher (514.5 GPa) than those along the [100] orientation ( $E=417.0$ ) or [110] orientation ( $E= 458.0$  GPa). Based on these values, bounding estimates of the elastic modulus have been calculated using the rule of mixtures.



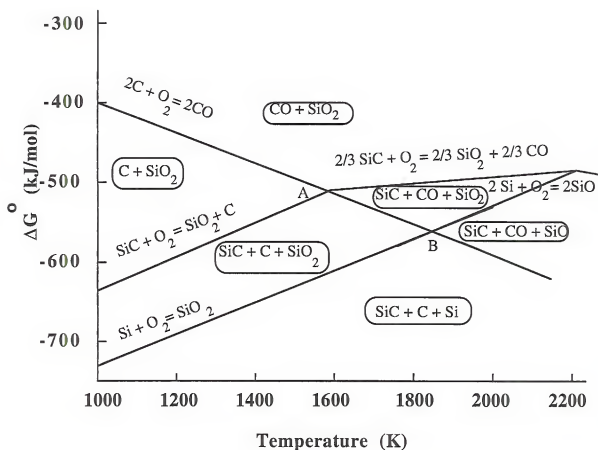


Figure 2-7 Schematic depicting the regimes of thermodynamic stability of the various phases for the carbothermal reduction of silica.

Such calculations yield an average value of the Young's modulus of 437.5 GPa . This value is slightly higher than the experimentally determined moduli of polycrystalline MoSi<sub>2</sub>, possibly due to second phase (Mo<sub>5</sub>Si<sub>3</sub>, SiO<sub>2</sub>) and porosity effects. The higher

Table 2-2 Elastic modulus of MoSi<sub>2</sub>

Temperature (°C)	E (GPa)	Reference and Comments
20°C	406.784	Max 52c, Dynamic Modulus
20°C	387.5	Sri 92 , 96 % Theoretical Density, Dynamic modulus
1260°C	275.786	Materials Advisory Board, National Academy of Sciences): Report # 4, Ad hoc committee on refractory inorganic non metals, structural materials, Jan 1961.
1370	172.366	
1510	82.736	

values of the elastic modulus along the c axis are significant from the viewpoint of thermal stresses, which, in turn, could have implications in microcracking behavior, fatigue properties, etc.

### 2.5.2 Diffusivity

Ivanov and coworkers conducted isothermal vacuum siliconizing studies on molybdenum at temperatures from 1200°C to 1350°C [Iva 67]. Silicon gradients in silicide layers were analyzed by XRD analysis of successive silicide layers. The

activation energies for the diffusion of silicon in  $\text{Mo}_5\text{Si}_3$  and  $\text{MoSi}_2$ ,  $Q_{\text{Mo}_5\text{Si}_3}^{\text{Si}}$  and  $Q_{\text{MoSi}_2}^{\text{Si}}$  were determined to be  $126 \pm 12$  kCal/mole and  $57.6 \pm 6$  kCal/mole respectively. These values of  $Q_{\text{Mo}_5\text{Si}_2}^{\text{Si}}$  are in good agreement with those reported by Bartlett and coworkers [Bar 64]. The temperature dependence of the diffusion coefficients of silicon in  $\text{Mo}_5\text{Si}_3$  and  $\text{MoSi}_2$  were likewise found to fit the form,

$$D_{\text{Mo}_5\text{Si}_3}^{\text{Si}} = 2.2 \times 10^8 \exp\left(\frac{-63,000}{T}\right)$$

and

$$D_{\text{MoSi}_2}^{\text{Si}} = 0.8 \exp\left(\frac{-28,800}{T}\right)$$

respectively.

Of significance is the high diffusivity of silicon when compared to that of the molybdenum in the silicide, as confirmed by this and other studies [Iva 67; Tho??]. The size effect seemingly associated with the faster diffusion of the smaller Si atoms in the refractory silicide lattices in comparison to the larger metal atoms is in opposition to the trend observed in metals, where diffusion takes place by vacancy motion. For example, the activation energy for silver and copper diffusion in copper are reported as 46.6 and 49.6 kCal respectively. The slower metal diffusion in the case of the silicides has been ascribed to their structure and the cohesive energy. Specifically, it has been argued that the repulsion between the metal atom cores makes the diffusion of large metal atoms difficult. No direct experimental evidence exists for the lattice diffusivity of Mo in  $\text{MoSi}_2$ . However, Bose [Bos 92] has attempted to derive estimates of the activation energy for self diffusion through the use of Zener's theory [She 63] through the empirical relationship,  $\Delta H/T_m = 150.7 \text{ JK}^{-1}$ . Assuming  $T_m = 2311 \text{ K}$ , the effective activation energy was computed to be  $347.5 \text{ kJ mol}^{-1}$ . In a similar fashion, Sadananda et al. [Sad 92] have invoked the semi-empirical relation derived by Kucera and Million [Kuc 70] derived originally for regular solid solutions to estimate the bounds of the activation energy for the intermetallic compound. Using the relationship

$$Q_{MoSi_2}^{Mo} = T_{mMoSi_2} \left( \frac{Q_{Mo}^{Mo} X_{Mo}}{T_{mMo}} + \frac{Q_{Si}^{Si} X_{Si}}{T_{mSi}} \right)$$

where  $T_{mi}$  is the melting temperature of component  $i$ ,  $Q_{Mo}^{Mo}$  and  $Q_{Si}^{Si}$  the activation energies for self diffusion for molybdenum in molybdenum (460 kJ mol<sup>-1</sup>) and silicon in silicon (~460 kJ mol<sup>-1</sup>) respectively, and using  $T_m$  values of 2020, 2610, and 1410 °C respectively for MoSi<sub>2</sub>, Mo and Si, they arrived at activation energy estimate of 540 kJ mol<sup>-1</sup>. In arriving at this approximation, one recognizes that MoSi<sub>2</sub> is not a solid solution, but rather an intermetallic compound. From the above two estimates, the activation energy for Mo diffusion in MoSi<sub>2</sub> is estimated at between 350 and 500 kJ mol<sup>-1</sup>.

Grain boundary diffusivity data are also lacking for MoSi<sub>2</sub> at this time.

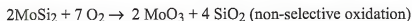
Therefore, the interpretation of the experimental diffusivity results in the literature requires considerable caution. For instance, Samsonov and coworkers [Sam 59], reported diffusivity values for Si in the silicide in the range of 13.387 kCal/mol, which is a quarter of the values reported through the vacuum siliconizing experiments of Ivanov [Iva 67]. The validity of Samsonov's values have been seriously questioned in view of the presence of chlorine in the siliconizing atmospheres of their study, as a result of their use of SiCl<sub>4</sub> as a silicon derivative for their siliconizing experiments. The presence of chlorine in the siliconizing atmosphere leads to the solutionizing of chlorine in the MoSi<sub>2</sub>, thereby resulting in a breakdown of the silicide lattice and a consequent reduction of the activation energy for silicidization.

An interesting, though somewhat unrelated observation concerns the mobility of Mo and W in the alloy silicide. Baglin et al. report that [Bag 79], although MoSi<sub>2</sub> and WSi<sub>2</sub> have similarly sized atoms, they do not intermix until about 1100°C, lending support for the earlier discussions on the low mobility of the refractory metal atoms in the silicide.

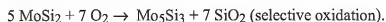
## 2.6 Oxidation Characteristics

MoSi<sub>2</sub> possesses excellent oxidation resistance at high temperature because of the formation of a self passivating, self healing, amorphous adherent silica layer that protects the underlying silicide [78 Sch] from further oxidation. These characteristics prompt MoSi<sub>2</sub> to be considered for protective coating applications on molybdenum, as well as its long-standing use in "Kanthal Super " heating elements. Pure and alloyed silicide coatings are thus considered as the most promising coating materials for high temperature oxidation protection.

MoSi<sub>2</sub> exhibits active oxidation below 800°C and passive oxidation behavior above that temperature. These differences between the high (T>800°C) and low (T<800°C) temperature oxidation regimes have been attributed by Wirkus and Wilder [Wir 66] to a change in the oxidation mechanism associated with the volatilization of MoO<sub>3</sub>. At T<800°C, crystalline MoO<sub>3</sub> and SiO<sub>2</sub> are the oxidation products, formed according to the following reaction:



At higher temperatures, MoO<sub>3</sub> ceases to be an oxidation product, thereby leading to the following high temperature reaction:



The glassy oxide scale formed at high temperatures offers the best protective properties, and thus pre oxidation of the MoSi<sub>2</sub> coatings at 1400-1500°C is preferable before using the coated material at lower temperatures. Of interest is the negligible solubility of molybdenum in the glassy silica layer.

At and above 1700°C, MoSi<sub>2</sub> does not have satisfactory oxidation resistance due to a combination of factors. SiO<sub>2</sub> (cristobalite) melts at 1725°C, and oxygen diffusion through the liquid layer is rapid; Oxide evaporation (SiO<sub>2</sub>, SiO, molybdenum oxides)

becomes important, and the volatile oxides are formed at the oxide/substrate interface, resulting in the rupture of the protective scale.

The effective lifetime of the silica coatings will also be influenced by repeated thermal cycling, which could lead to the cracking of the thermal scale due to CTE mismatches between the scale and the substrate. The presence of cracks in the coating does not necessarily lead to the failure of the coated part, since subsequent heating heals the cracks, partly by thermal expansion and sintering and partly by the formation of new  $\text{SiO}_2$ . Fitzer [Fit 85] has shown that Ge additions to  $\text{MoSi}_2$  result in better resistance of the oxide to thermal cycling because of the higher CTE of  $\text{GeO}_2$ .

Catastrophic oxidation of  $\text{MoSi}_2$  has been reported in the temperature range 450-600°C, resulting in the complete disintegration of the specimen. This phenomenon is termed "silicide pest", and, according to Fitzer [Fit 55], involves a form of intergranular oxidation of  $\text{MoSi}_2$  in which each grain eventually becomes surrounded by oxidation products. Westbrook and Wood [Wes 64] proposed that pesting was due to the intergranular diffusion of the reactant gas. Recent results [Mck 92, Cho 93] seem to confirm this hypothesis with the disintegration of  $\text{MoSi}_2$  being initiated by oxygen diffusion along pores and cracks, followed by  $\text{MoO}_3$  formation, which in turn produces stresses resulting from the volumetric expansion of  $\text{MoO}_3$ , thereby pushing the grains apart. Schlichtling [Sch 78] and Meschter [Mes 92] have demonstrated that the phenomenon is composition and porosity dependent, and that pesting can be avoided by the fabrication of  $\text{MoSi}_2$  bodies containing less than 4% porosity and less than 5 wt. %  $\text{Mo}_5\text{Si}_3$ . These results thus alleviate concerns that  $\text{MoSi}_2$  is a pest-limited material, and indicate that it is imperative to develop processes to fabricate near-full-density, near-stoichiometric  $\text{MoSi}_2$ .

## 2.7 Mechanical Properties

### 2.7.1 Single Crystals

The high temperature deformation mechanisms of  $\text{MoSi}_2$  have been studied by numerous groups [Uma 90, Kim 91, Uma 89, Uma 90]. Dislocation energy considerations would lead one to expect the activation of dislocations with the shortest burgers vectors, namely the  $\langle 100 \rangle$ ,  $1/2\langle 111 \rangle$  and  $\langle 110 \rangle$  (Please refer to Fig. 2-2 for the crystal structure). The densest slip plane, which would have the lowest Peierls stress, are the  $\{110\}$ , followed by  $\{001\}$  and  $\{011\}$ . It is therefore not surprising that the primary slip system is the  $\{011\}\langle 100 \rangle$ , with the secondary  $\{1\bar{1}0\}1/2\langle 111 \rangle$  system being activated at a higher temperature. Umakoshi et al. [Uma 90] report a  $\{1\bar{1}0\}1/2\langle 3\bar{3}1 \rangle$  slip in single crystal compression studies at temperatures less than  $1100^\circ\text{C}$ , but these are not seen in polycrystalline samples deformed at  $1200^\circ\text{C}$ .

From compression tests and subsequent slip trace analysis, Umakoshi et al. determined the orientation dependence of the observed slip plane at  $900^\circ\text{C}$ . Slip primarily occurs along the close-packed  $\{110\}$  planes.  $\{013\}$  slip is also observed, but only for the orientations near the  $[001]$  corner where the ratio of the Schmid factor for the  $(013)\langle 3\bar{3}1 \rangle$  to that of  $\{110\}\langle 3\bar{3}1 \rangle$  is more than 1.7. Above  $1300^\circ\text{C}$ ,  $\langle 100 \rangle$  and  $\langle 110 \rangle$  type ordinary dislocations were also observed. The plastic deformation is controlled by the movement of these dislocations.

The stress-strain curves of single crystal  $\text{MoSi}_2$  deformed in compression along  $[001]$  and close to  $\langle 100 \rangle$  orientations are shown in Fig. 2-8. Both ductility and the BDTT exhibit strong orientation dependencies, with higher ductilities and lower BDTTs ( $\sim 1100^\circ\text{C}$ ) reported along the  $\langle 100 \rangle$  orientation than the  $[001]$  orientation, which show negligible ductility up to  $\sim 1300^\circ\text{C}$ . The yield strengths (0.2% offset) of the  $[001]$

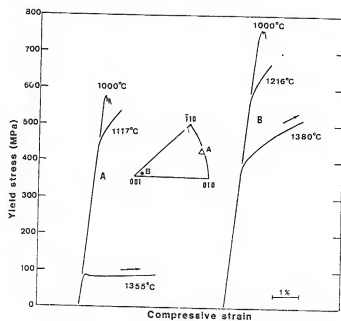


Figure 2-8 Stress-strain curves of single crystal MoSi<sub>2</sub> along various crystallographic orientations



orientation are higher than the those of the  $\langle 100 \rangle$  orientation. These differences have been attributed to differences in the active slip plane, with the  $[001]$  orientations deforming on  $\{013\}$  in contrast to the  $\langle 100 \rangle$  oriented crystals which undergo  $\langle 331 \rangle \{110\}$  slip [Uma 90, Kim 90]. However, the analysis leading to the conclusion of  $\langle 331 \rangle$  slip seems to be suspect. Curiously, dislocation analyses on  $1200^\circ\text{C}$  deformed polycrystalline samples do not support the  $\langle 331 \rangle$  slip [Unal 91], nor do the single crystal studies by Maloy [Mal 93]. Rather, slip was reported on the  $\{110\} \langle 100 \rangle$  (primary) and the  $\{110\} \langle 111 \rangle$  (secondary) systems. This seems reasonable from the energy standpoint, since  $1/2 \langle 331 \rangle$  is a relatively large Burgers vector.

The temperature dependence of the single crystal compressive yield strengths is plotted for various orientations in Fig. 2-9. The yield stress is highly dependent on the orientation at temperatures lower than  $1000^\circ\text{C}$ , with the  $[001]$  orientation exhibiting the highest strengths at all temperatures. The  $1100^\circ\text{C}$  strength for this orientation is about 750 MPa, with the other orientations showing lower values between 300 and 450 MPa. The yield stress remains constant from RT up to about  $1100^\circ\text{C}$ , beyond which it drops to about 100 MPa at  $1400^\circ\text{C}$ . However, the  $\langle 001 \rangle$  orientation maintains strength levels of upto 300 MPa at  $1500^\circ\text{C}$ .

## 2.7.2 Polycrystals

### 2.7.2.1 Strength

The strength data are summarized in Tables 2-3 and 2-4. This study found that, with the exception of the early work by Maxwell [Max 49, Max 50] and Long [Lon 52], little has been done to study the effect of processing variables on the properties of monolithic  $\text{MoSi}_2$ . Significantly, the earlier studies demonstrated a significant impact of such processing parameters as the initial powder size distribution, processing route (sintering versus hot pressing), and oxygen and carbon contents on the tensile strength, ductility and the BDTT (See Fig 2-10, elongation data next to data points). Fine powders

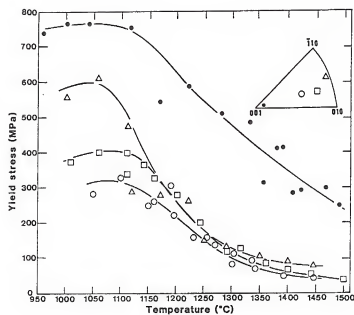


Figure 2-9 Temperature dependence of compressive strengths for different orientations of single crystal MoSi<sub>2</sub>.

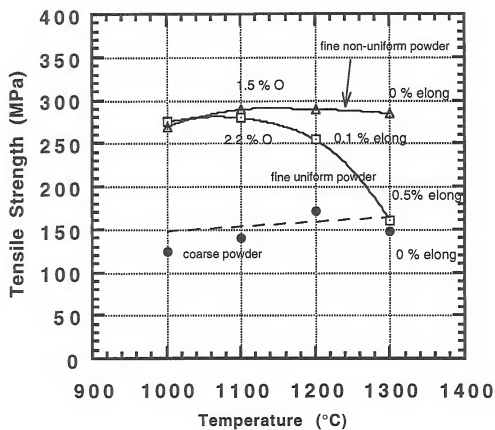


Figure 2-10 Short term tensile strengths of MoSi<sub>2</sub>.

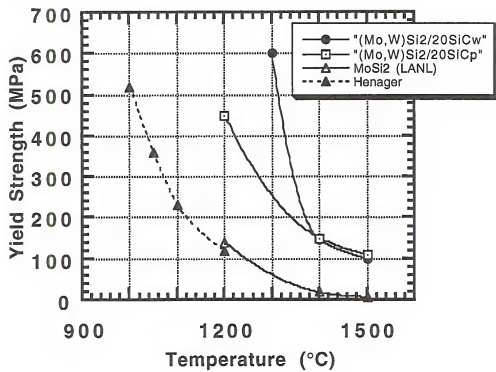


Figure 2-11 Yield strength of MoSi<sub>2</sub> - based materials (four-point bend tests).

Table 2-3 Short Time Tensile Strengths of MoSi<sub>2</sub>

Temperature (°C)	$\sigma_{ult}$ (MPa)	$\sigma_{ult}$ (MPa)	Reference
RT			
870	262		Lat 62
900	289		Mou 60
980	276		Lon 50
1095	289		Lon 50
1205	289		Lon 50
1315	282		Lon 50

Table 2-4 Bend Strength of MoSi<sub>2</sub> as a Function of Temperature

Strength (MPa)	Temperature (°C)	References & Comments
150 ( $\sigma_{ult}$ )	0-1200°C	Car 90
210 ( $\sigma_{ult}$ )	1400°C	Aik 92b, (high purity)
183 ( $\sigma_{ult}$ )	1400°C	Aik 92b, (Low purity)
14 ( $\sigma_{ult}$ )	1400°C	Car 90

of 3  $\mu\text{m}$  median size, but with either a "uniform" or "non-uniform" distribution yielded very different results in terms of ultimate strengths and elongations. The tensile ultimate strength showed an increase from RT upto 1200°C in all cases. Such strength increases with increasing temperature has been observed in Si<sub>3</sub>N<sub>4</sub> ceramics with grain boundary phases and have been attributed to high cavitation thresholds (in excess of the strength of the material) and the lack of connectivity of the glass phase [Zen 92]. The specimens derived from non-uniform powders (with 1.5% oxygen) showed no detectable elongation upto 1315°C, while the uniform powder derived specimens (similar oxygen contents)

displayed 0.1% elongation at 1200°C and 0.5% elongation at 1315°C. The total lack of plastic deformation in the oxygen (silica) containing specimens above the softening point of silica is not surprising, and has been previously reported in  $\text{Si}_3\text{N}_4$  materials over a range of strain rates from  $10^{-4}$  to  $10^{-6}$  per second [Zen 92]. This behavior has been attributed to localization of the glassy phase at triple points at 10 v/o  $\text{SiO}_2$  levels, with the  $\text{Si}_3\text{N}_4$  grains acting as obstacles to viscous flow (lack of connectivity between the glass pockets). The ultimate strengths in Long's study showed significant differences based on the powder characteristics, with the "non-uniform" powder material displaying significant strength retention at the expense of ductility especially at temperatures above 1200°C, while the uniform powder derived samples showed increased elongation and a sharp drop in strength above this temperature. Interestingly, these results were observed beyond the softening temperature of the silica phase, 1200°C. While it is tempting to argue that these differences could be due to differences in the silica content based on powder sizes, the size distribution of the powders suggests that this might not be the case. As if to support the argument against the oxygen content, samples fabricated from coarse powder ( $<16\mu\text{m}$ - 100%,  $< 6\mu\text{m}$  - 50%) (and therefore low oxygen content) showed decreased strengths throughout the entire temperature range (see Fig. 2-10).

These results indicate the need to understand and quantify the effects of both grain size and the morphology / volume fraction of the glass phase on the elevated temperature properties. In fact, most of the recent studies, which have focused on compositing approaches to derive optimal properties without such an understanding, have met with limited success. For instance, the addition of reinforcing SiC particles or whiskers, while improving the properties somewhat, do not have a sizable effect in curbing the drastic strength drops that are observed in the monolithic matrices between 1200°C and 1400°C [Fig. 2-11].

### 2.7.2.2 BDTT

Single crystal deformation studies [Uma 90] suggest that the BDTT is orientation dependent, with the [001] orientation exhibiting lower ductility and higher BDTT ( $>1200^{\circ}\text{C}$ ) than the orientations along the  $\langle 010 \rangle$  -  $\langle 110 \rangle$  boundary. These differences have been attributed to the difference in the active slip plane between these orientations and the CRSS. On the other hand, considerable amount of uncertainty exists regarding the actual value of the BDTT in polycrystalline  $\text{MoSi}_2$  [Lon 52, Max 50, Sch 78, Aik 92a,b] and this has been attributed to the presence of silica. While most of the earlier studies on polycrystalline  $\text{MoSi}_2$  report a BDTT of between  $1000^{\circ}\text{C}$  and  $1300^{\circ}\text{C}$ , a recent study [Aik 92] suggests that the BDTT could be much higher, in the range of  $1300^{\circ}\text{C}$  to  $1400^{\circ}\text{C}$ . Moreover, the study presents evidence that the presence of a scattered globular glassy phase in the amount of 6 v/o has no effect on the BDTT, and suggests that a difference in morphology of the silica phase (discrete globules in Aikin's work versus a continuous film in other studies) might be at the origin of the reported variations in the BDTT between the different research groups. Aside from the morphological differences of the intergranular phase, the grain size distribution and its interplay with the intergranular phase could also exert subtle microstructural effects on the BDTT and the deformation behavior. Indeed, the data presented in the next section seem to support this hypothesis.

### 2.7.3 High Temperature Deformation and Creep

Published reports of the creep data of  $\text{MoSi}_2$  and  $\text{MoSi}_2$  based composites are summarized in the Table 2-5. A few commonalities emerge from the data.

Table 2-5 Summary of Creep Data on MoSi<sub>2</sub> and MoSi<sub>2</sub> composites

Reference	Material, Grain size	Test Temp. (°C)	Applied stress (MPa)	Test Tech nique	Atmos phere	Stress Exponent, n	Grain size Expn t	Q <sub>act</sub> (KJ/mol)
Max 50	MoSi <sub>2</sub> , 1µm median	870-1093	49-245	tension	----	1.38	---	460
Bos 92	Single Crystal <210> HIP MoSi <sub>2</sub> , 2.5% pores 5% Mo <sub>5</sub> Si <sub>3</sub> 30 µm ditto HP MoSi <sub>2</sub>	1200 1200 1200	comp. tension comp. comp.	comp. tension comp. comp.	3			251 347.5 306 306
Sad 92	MoSi <sub>2</sub> HP 18-35 µm ditto 20v/o SiC <sub>w</sub> , 18 µm (Mo,W)Si <sub>2</sub>	1100-1400 >1200 <1300 >1300	>~30	comp. comp. comp.	1.9 1.2			433 (bet. 10-40 MPa) ditto 590 536 (bet. 8-30 MPa) ditto
Bas 91 Gib 92	HP MoSi <sub>2</sub> , 35 µm, 95% TD MoSi <sub>2</sub> (35 µm)- 15% SiO <sub>2</sub> (1-20 µm)	1000-1300 1100-1200	comp. 80-300	comp. comp.	air air	2.5 2.5- 20		191.9
	MoSi <sub>2</sub> -15% Mo <sub>5</sub> Si <sub>3</sub> MoSi <sub>2</sub> -45% Mo <sub>5</sub> Si <sub>3</sub>	1200-1300	40-500	comp.	air	2 - 3		253.6



Table 2-5-- (continued)

Reference	Material, Grain size	Test Tempr. (°C)	Applied stress (MPa)	Test Tech nique	Atmos phere	Stress Exponent, n	Grain size Expn t	Qact (KJ/mol)
Wei 92	(Mo, W)Si <sub>2</sub> -20v/o SiC <sub>w</sub> 20 µm, SiO <sub>2</sub> size 5 µm			tensile		3.2		557
				comp.		2.3 (data scatters)		312
Suz 93, Suz 92	XD MoSi <sub>2</sub>	1050-1300		comp		3.5		430
Jen 92, Jen 94	MoSi <sub>2</sub> /SiC -20 v/o plasma sprayed	T < 1300 T > 1300		comp.		2.4 - 2.6 1.4 - 1.6	2	300 190
	MoSi <sub>2</sub> /SiC -20 v/o plasma sprayed	1200-1550	40	comp.	air	n=3 to n=1 @20 MPa & @ 1350°C		

First,  $\text{MoSi}_2$  exhibits lower creep rate in compression than in tension, with the creep rates in tension being an order of magnitude higher than in compression for the same stress levels. These differences have been attributed to volumetric expansion effects associated with cavitation processes that occur easily in tension [Wei 92]. Second, the observed values of the stress exponents are close to 3 for most of the experiments. In the finer grain sized materials, however, the stress exponents in monolithic  $\text{MoSi}_2$  [Sad 92] and some  $\text{MoSi}_2/\text{SiC}$  composites [Jen 93] display an anomalous behavior, with stress exponents decreasing with increasing stresses (from  $n = 2.5$  to  $n = 1.2$ ) contrary to conventionally observed stress exponent behavior. Curiously, this behavior of the stress exponent is not seen in  $(\text{Mo,W})\text{Si}_2$  alloy matrices. The exact mechanism of this transition, as well as the reason for the associated threshold stress behavior are unknown, although  $n$  values close to 1 strongly indicate viscous flow processes such as grain boundary sliding. Compositing approaches have met with a good measure of success in enhancing elevated temperature strengthening, with  $\text{SiC}$  whisker reinforcements having been found to significantly improve the steady state creep properties [Sad 92]. Alloying with tungsten, does not contribute much to creep strengthening, while leading to higher densities [Sad 92].

Most of the creep studies have been performed on materials within a narrow grain size range of between 20 and 35  $\mu\text{m}$ , and very few in the grain size range of less than 10  $\mu\text{m}$ , where the silica effects are expected to be dominant. Furthermore, data is scant on the behavior of silica-free microstructures, presumably due to the difficulties involved in processing them from powders. Similarly, although attempts have been made to quantify the effect of intergranular silica phase, no attempt has been made to correlate these properties with silica-free materials. Neither has the interplay between the grain size and the silica content been studied in the deformation behavior of the material.

#### 2.7.4 Summary of Mechanical Properties

The previous sections serve to emphasize the poor low temperature damage tolerance and inadequate high temperature creep resistance of MoSi<sub>2</sub> and lead to the conclusion that monolithic MoSi<sub>2</sub> in both single crystal and polycrystalline forms (containing silica) is inadequate to warrant its consideration as a structural material. While several investigations have attempted to mitigate these problems through the use of particulates, whiskers and/or fibers to improve both fracture toughness and creep characteristics, these efforts have met with limited success. Thus, the problems of low toughness and degradation of strength in commercially derived composites above 1200°C still remain. Similarly, the BDTT in MoSi<sub>2</sub> is also likely to be controlled by the morphology and distribution of the intergranular phase and/or the grain size. These factors point to a need for a systematic understanding of the interrelationship between the structure (i.e. grain size distribution and silica content) and properties, in order to optimize the processing of the monolithic material.

### 2.8 Creep Deformation Mechanisms in Polycrystalline Materials

#### 2.8.1 Phenomenological Equation

The steady state creep rate,  $\dot{\epsilon}$ , for most mechanisms of high temperature creep is given by the generalized power law equations of the form

$$\dot{\epsilon} = (ADGb / kT) (b/d)^p (\sigma/G)^n \quad (2.10)$$

or

$$\dot{\epsilon} = A \sigma^n \exp (-Q/kT) \quad (2.11)$$

where D is the diffusion coefficient, G the shear modulus, b the Burgers vector, k the Boltzmann constant, T the absolute temperature, d the grain size, p the inverse grain size

exponent,  $n$  the stress exponent, and  $A$  the dimensionless constant. The diffusion coefficient is given by

$$D = D_0 \exp(-Q/RT), \quad (2.12)$$

where  $Q$  is the activation energy for the diffusion process and  $R$  the gas constant ( $8.31 \text{ J mol}^{-1}\text{K}^{-1}$ ). Each creep mechanism is uniquely specified by the values of the three constants,  $A$ ,  $p$ , and  $n$ , and by the activation energy  $Q$ . Thus, the interpretation of the rate controlling creep mechanism in a polycrystal is usually determined with reference to the  $n$ ,  $p$ , and  $Q$  values. If the dominant mechanisms are intragranular, there is no dependence of the grain boundaries and therefore  $p=0$ ; whereas if the deformation process involves the grain boundaries, the value of  $p$  is in the range from 1 to 3.

Analyzing the minimum creep rate versus stress data with a power law creep model is thus a generally useful method of gaining insight into the mechanisms governing creep provided the material behavior is consistent with the assumptions of the models. These assumptions include

- (a) Operation of a single creep mechanism, and,
- (b) Occurrence of uniform plastic deformation over the entire gage length (no localized plastic instability or necking) without other failure mechanisms occurring concurrently (transgranular or g.b. cracking, creep cavitation, etc.).

## 2.8.2 Creep Mechanisms

Creep mechanisms can broadly be classified into two types, lattice mechanisms and boundary mechanisms.

### 2.8.2.1 Lattice Mechanisms

These are based on the intragranular motion of the dislocations and, by definition, they require that  $p=0$ . Many theoretical mechanisms have been developed for intragranular deformation, and the most important of these are summarized in Table 2-6 in terms of the predicted values for  $n$  and  $Q$ , where  $Q_{\text{lat}}$ ,  $Q_{\text{ci}}$ , and  $Q_p$  are the activation

energies for lattice self diffusion, chemical interdiffusion of solute atoms, and pipe diffusion along the dislocation cores, respectively. A complete description of each of these mechanisms is given in the various references cited in Table 2-6. It is to be noted that many of the theoretical models lead to identical predictions of  $n$  and  $Q$ .

Table 2-6 Creep parameters for lattice mechanisms with  $p=0$

Mechanism	$n$	$Q$	Reference
Dislocation glide and climb, controlled by climb	4.5	$Q_{\text{lattice}}$	Weertman 57
Dislocation glide and climb, controlled by glide (Peierls stress controlled)	3	$Q_{\text{chemical interdiffusion}}$	Weertman 68
Non-conservative motion of jogged screw dislocations	3	$Q_{\text{lattice}}$	Barrett 65
Dislocation climb from Bardeen-Herring sources	3 5	$Q_{\text{lattice}}$ $Q_{\text{pipe}}$	Nabarro 67
Nabarro Herring creep at subgrain boundaries	3	$Q_{\text{lattice}}$	Friedel 64
Dislocation climb by pipe diffusion	5	$Q_{\text{pipe}}$	
Harper-Dorn Creep	1	$Q_{\text{lattice}}$	Langdon & Yavari, 82

### 2.8.2.2 Boundary Mechanisms

Boundary mechanisms are based on the deformation processes associated with the grain boundaries, so that, by definition,  $p>1$ . Table 2-7 lists several boundary

mechanisms in terms of the predicted values of  $n$ ,  $p$ , and  $Q$ , where  $Q_{ph}$  is the activation energy associated with the presence of a grain boundary liquid phase. A consequence of all boundary mechanisms is that the adjacent grains are displaced with respect to each other, with the displacement occurring at, or close to the grain boundary plane. If grain boundary sliding occurs in association with grain elongation in the direction of tensile stresses, the sliding is known as Lifshitz sliding. On the other hand, if the grain boundary displacement is not associated with grain elongation, it is classified as Rachinger sliding [Lan 83]. Rachinger sliding is important in siliceous materials when a thin glassy phase is present at the grain and interphase boundaries. In the absence of a liquid phase, sliding may be accommodated locally by the opening up of grain boundary cavities or fold formation at triple points.

### 2.9 Liquid Enhanced Creep

Many structural materials contain significant amounts of glassy intergranular phases (5-10 v/o) due to the incorporation of surface silica present in the starting powders. These glass phases are typically found in pockets interspersed amongst the grains or as thin films along the grain boundaries. These low melting intergranular phases limit the operating temperature of such materials for structural applications. As a result, the role of viscous intergranular silica on the elevated temperature mechanical properties of structural ceramic materials such as SiC, Si<sub>3</sub>N<sub>4</sub>, Al<sub>2</sub>O<sub>3</sub> has been a subject of continued interest and considerable study by numerous workers.

Over the last two decades, a wealth of experimental data has been generated, along with the development of mathematical models, for understanding the behavior of ceramic materials in the presence of boundary-wetting intergranular phases, especially with regard to properties such as creep and fracture toughness, and a variety of mechanisms and models have been proposed. From these studies, it has emerged that minor amounts (< 2%) of a wetting intergranular phase existing as a thin (~2 nm)

Table 2-7 Creep parameters for boundary mechanisms

Mechanism	n	p	Q	Reference
<b><u>LIFSHITZ SLIDING</u></b>				
<b>Sliding accomodated by diffusion</b>				
Nabarro-Herring creep	1	2	Q <sub>lattice</sub>	Nabarro 48, Herring 50
Coble creep	1	3	Q <sub>gb</sub>	Coble 63
<b>Sliding accomodated by intragranular flow across grains</b>	1	1	Q <sub>gb</sub>	Crossman & Ashby 75
<b><u>RACHINGER SLIDING</u></b>				
<b>With a continuous glassy phase at the boundary:</b>				
Liquid enhanced sliding	1	1	Q <sub>ph</sub>	Orowan 47
Solution -Precipitation	1	3	Q <sub>ph</sub>	
<b>Without a glassy phase:</b>				
Sliding accompanied by formation of grain boundary cavities	2	1	Q <sub>lattice</sub>	Langdon 70
Sliding accompanied by formation of triple point folds	3.5	2	Q <sub>lattice</sub>	Gifkin 73
<b><u>INTERFACE REACTION CONTROL</u></b>				
With glassy phase (solution precipitation)	1	1		Raj & Cheung 81
By solute drag	2	1	Q <sub>solute</sub>	Arzt, Ashby & Verrall 77
Without a glassy phase	1<n<2			Ashby 69, Greenwood 70, Burton 72
	2	2	Q <sub>gb</sub>	Schneibel & Hazzledine 83

film on the grain boundaries could severely degrade the elevated temperature properties in the vicinity of the softening temperature of the intergranular phase. A whole host of mechanisms such as lubricated grain boundary sliding, solution reprecipitation creep, cavitation etc. have been proposed to control the flow and fracture properties at these temperatures. While most of these studies have concentrated on wetting grain boundary phases, very little is known on the behavior of the materials with a non-wetting grain boundary phases.

MoSi<sub>2</sub> has a siliceous intergranular phase, similar to most other siliceous materials. However, unlike most ceramics, the glass phase in MoSi<sub>2</sub> exhibits a non-wetting behavior at the grain boundaries. The high dihedral angle of the glassy phase and the resultant non-wetting characteristics are in sharp contrast to the wetting characteristics of the glassy phase found in most ceramics such as Si<sub>3</sub>N<sub>4</sub>, Al<sub>2</sub>O<sub>3</sub> etc., where the glass phase subtends a near zero dihedral angle with the crystal boundaries. The effect of this difference in silica morphology on the deformation mechanisms is unclear.

Little evidence in literature is available on the behavior of materials containing non-wetting phases to predict the influence of this intergranular phase on the properties of MoSi<sub>2</sub>. In fact, the only known study on the elevated temperature behavior of a material containing a non-wetting phase was conducted by Pharr and Vandrager. Through a series of creep experiments straddling the melting temperature of lead in a microstructure consisting of 3 wt. % Pb, they showed that the creep exponents and the activation energies were unchanged through the melting range, thus proving that minor amounts of the non-wetting liquid phase had no effect on the creep behavior of the material. Furthermore, the study also showed that the creep mechanisms were significantly affected only when more than 70% of the grain boundary area was covered by the non-wetting intergranular phase. In contrast, it was found that for wetting systems such as Cu-Bi, less than 3 v/o of the liquid bismuth was sufficient to cause a shift to liquid enhanced creep mechanisms [Pha 89].



### 2.9.1 Mechanisms of Liquid Enhanced Creep

Two types of mechanisms have been proposed for liquid enhanced creep, and are described as follows.

#### 2.9.1.1 Lubricated Flow (Viscous Flow)

Pharr and Ashby [Pha 83] proposed the simplest model for liquid enhanced creep. They considered that the grain boundary glass acts as a lubricant, allowing the grains to slide over each other more easily. For an applied deviatoric stress  $\sigma$ , the creep rate is given as a function of grain size  $d$ , grain boundary thickness  $w$ , and viscosity  $\eta$  can be written as

$$\dot{\epsilon} = a \left[ \frac{w}{(w + d)} \right] \left( \frac{\sigma}{\eta} \right)$$

where  $a$  is a constant having a value of approximately  $1/3$ .

The drawback with this model is that it does not accurately capture the complexity of the microstructure in most materials. The geometry of this model allows the grains to slide over each other indefinitely without ever interlocking (unstable shear deformation), something that is never true in real microstructures. In reality, the grains lock up after a finite amount of deformation, thereby increasing the forces required to maintain the same rate of creep.

Investigating the deformation of sintered carbides, Drucker [Dru 64] quantified the effect of fluid flow on the creep by assuming a more realistic model - a 2-dimensional hexagonal array of grains surrounded by a viscous phase with a homogeneous flow of the liquid throughout the material. The viscosity  $\eta_{eff}$  of the material was found to be inversely proportional to the cube of the volume fraction of the boundary phase, i.e.

$$\eta_{eff} = \frac{\eta_i}{f^3}$$

where  $\eta_i$  is the intrinsic viscosity of the grain boundary phase, with the shear strain and the shear stress  $\tau$  being related by

$$\gamma = \frac{\tau}{\eta_{eff}}$$

It has however been argued that viscous flow controlled creep is not a viable mechanism. It has been reasoned that as the grains slide past each other, fluid is squeezed out of the compressive interfaces and the grains eventually become interlocked. Thus, viscous flow must be a transient process, limited by the impingement of adjacent grains. Also, as the grain boundary phase is incompressible, pressure gradients could develop that quickly oppose further sliding. Modeling a hexagonal grain array similar to the earlier Drucker model, Dryden et al [Dry 89] have demonstrated that the strains at which such interlocking occurs is of the same order as the volume fraction of the viscous phase (which is typically 5 to 10 %). Since the failure strains are much smaller in most glass ceramics, they have argued that viscous flow could still remain a viable creep mechanism, with the glass phase being redistributed from the regions of compressive stress to the regions under tension.

#### 2.9.1.2 Solution Reprecipitation Creep

This mechanism of liquid enhanced creep involves the dissolution of the solid phase from the grain boundaries in compression, followed by rapid transport through the liquid phase (Mar 83), and finally redeposition (reprecipitation) at the boundaries under tension (i.e. a Coble mechanism with transport through the liquid phase). Since this mechanism implicitly assumes the liquid phase to have some degree of solubility for one or more of the species of the crystalline phase, such a mechanism is also likely for  $\text{MoSi}_2$  with a liquid intergranular silica or silicon phases. Limited solubility of Mo in  $\text{SiO}_2$  has been reported by Clayton and coworkers [Cla 95]. Their XPS analysis of the silica yielded an approximate stoichiometry of  $\text{Mo}_{0.05}\text{SiO}_2$ . At these levels, the solubility of molybdenum is sufficient to effect mass transport through the liquid intergranular phase.

The rate controlling step for this mechanism could be

(1) the dissolution / reprecipitation process itself (solution / attachment kinetics limited), or,

(2) the transport process through the grain boundary phase (transport kinetics limited). Both of these are thermally activated processes.

Based on these different rate limiting kinetics, two models have been proposed by R. Raj and C.K. Chyung [Raj 81] and by Pharr and Ashby [Pha 83]. While differing in their approaches, these models however share the following premises:

1) The solid phase must have a limited degree of solubility in the liquid phase  
 2) The rate of deformation is limited by the physical processes limited to the liquid phase. (Specifically, the transport of matter through the liquid phase or the liquid solid dissolution / reprecipitation process)

3) The solid liquid dihedral angle is assumed to be small, approaching zero, so under conditions of equilibrium, the liquid wets the solid grain boundaries.

Under these three combined conditions, enhancements in the creep rates by three or more orders of magnitude are predicted, and have indeed been reported [Pha 83, Lang.80]. For dihedral angles between 0 and 60°, the melt forms a 3-D interconnected network along the triple junctions, yet does not wet the grain boundaries and, therefore, enhancements in the creep rate due to this mechanism are not significant.

Thus, for the case of diffusion-controlled creep enhanced by the grain boundary liquid or amorphous phase, the creep enhancements may be described by substituting the diffusion coefficient in the liquid,  $D_b$  into the Coble equation [Cob 63, Sto 73]

$$\dot{\epsilon} = \frac{A\sigma\Omega\delta_{gb}D_{gb}}{kTd^3}$$

where  $A_1$  is the constant,  $\Omega$  is the atomic volume,  $C$  is the solubility for the constituent atoms in the liquid,  $\delta_{gb}$  is the effective thickness of the grain boundary,  $D_{gb}$  is the grain boundary diffusivity,  $k$  is the Boltzmann constant,  $T$  is the temperature, and  $d$  is the grain size. Thus, for the case where mass transport through and across the grain boundary is

rate controlling, the above equation modifies by substituting  $C_1\delta_1D_1$  for  $\delta_{gb}D_{gb}$ , where  $C_1$  and  $D_1$  are the solubility and diffusivity, respectively, of the rate controlling species in the liquid film, and  $\delta_1$  is the liquid film thickness. Since  $\delta_1$  is proportional to the volume fraction of the liquid phase,  $V_1$  and the grain size, we obtain the following equation for diffusion-controlled liquid enhanced creep:

$$\dot{\epsilon} = \frac{A_2 \sigma \Omega V_1 C_1 D_1}{k T d^2}$$

where  $A_2$  is a new constant.

If the solute diffusion rate far exceeds the interface reaction rate required for atom attachment and detachment, the interfacial reaction is rate controlling, and the strain rate is proportional to the rate of the interfacial reaction. For this scenario, the creep rate is given by

$$\dot{\epsilon} = \frac{A_3 C_1 (\sigma \Omega)^n}{k T d}$$

We note that while the diffusion-controlled solution-precipitation creep model predicts a linear stress dependence of the strain rate, the interface reaction controlled model predicts  $n$  values ranging from 1 to 2.

## 2.10 Superplasticity

The ability of fine grained materials ( $d < 10 \mu\text{m}$ , where  $d$  is the grain size) to exhibit extensive plastic deformation, often without the formation of a neck prior to fracture, is generally known as micrograin (structural) superplasticity.

The strain rate sensitivity index is an important parameter characterizing the superplastic deformation. In keeping with the general equation for deformation, the strain rate sensitivity index is defined mathematically as

$$m = \frac{\partial(\ln \sigma)}{\partial(\ln \dot{\epsilon})}$$

Conventionally, superplasticity of an alloy is determined through measurements of strain rate sensitivity, either by a series of tensile tests at different strain rates at the temperature of interest, or by a single test undertaken at a series of strain rates.

Superplasticity requires high strain rate sensitivity ( $m > 0.4$  to 1). Through a rigorous analysis, Hart [Har 67] has shown that reasonable superplastic ductilities can be achieved for SRS values in the range of  $0.4 < m < 1.0$ .

In addition to high strain rate sensitivity, grain boundary cohesivity (absence of intergranular brittleness) is yet another requirement of structural superplasticity for most ceramic and intermetallic materials, so that large tensile deformations are facilitated without grain boundary fracture.

#### 2.10.1 Stress-Strain Rate Variations

The steady state flow of structurally superplastic materials shows an increase in the flow stress with increasing strain rate. The variation of  $\ln \sigma$  with  $\ln \dot{\epsilon}$  is characteristically sigmoidal and for convenience [Edi 76b], the curve is divided into three regions (see Fig. 2-12). The region of maximum strain rate sensitivity (region II) delineates the strain rate range over which superplasticity occurs at the selected temperature. At both low and high strain rates (region I and III) the strain rate sensitivity is smaller and these correspond to more conventional forms of plastic deformation.

#### 2.10.2 Materials Considerations for Superplastic Deformation

High deformation rates and high ductility are the primary objectives in developing superplastic materials. Practical considerations further dictate that these properties be achieved at the lowest processing temperature. The basis of materials considerations

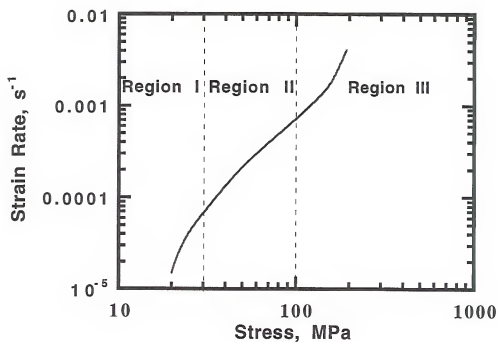


Figure 2-12 Schematic representation of the typical flow characteristics of a superplastic material showing the sigmoidal flow stress- strain rate relationship

governing the microstructure design for superplasticity is obvious from the governing equation for superplastic flow, which is expressed in the form,

$$\dot{\epsilon} = (AD_0Gb / kT) (b/d)^p (\sigma/G)^n \exp(-Q/kT) \quad (2.13)$$

where  $\dot{\epsilon}$  is the strain rate,  $\sigma$  is the stress, and  $n$  and  $p$  are the stress and grain size exponents respectively. The high deformation rates and low temperatures required for superplastic deformation can be achieved by decreasing the grain size, increasing lattice and grain boundary diffusivities, or introducing a grain boundary liquid phase to provide a fast diffusion path.

The processing route used in the fabrication of the bodies also has a significant bearing on the formability of the material. Structural superplastic flow requires uniform deformation which imposes stringent requirements on the material microstructure insofar as near uniform fine grain sizes and uniform chemical homogeneity; otherwise, shear bands might be nucleated at heterogeneities which, in turn, would lead to non-uniform deformation and subsequent loss of superplastic characteristics.

Microstructural stability during deformation is yet another requirement of superplasticity. As with duplex metallic structures, ceramic and intermetallic composites have the advantage of superior microstructural stability against static and dynamic coarsening, especially at volume fractions less than 20 v/o. For example, while fine grained pure alumina is subject to rapid grain growth and consequent loss of superplastic formability, its grain size remains largely stable during superplastic deformation with 10 v/o zirconia additions. Second phases also suppress the strain hardening behavior, thus contributing to the superplastic behavior as well. Likewise, duplex microstructures (i.e.) microstructures in which two phases of nearly equal volume fraction and both multiply connected, such as Pb-Sn and Zn-Al alloys,  $\alpha$ - $\beta$  Ti alloys, and  $\alpha$ - $\gamma$  stainless steel, are also amenable to superplastic deformation due to their ability to maintain their refined microstructures, essential for superplastic formability at forming temperatures (below the sintering or hot pressing temperatures).

From a microstructural control viewpoint, there is an important relationship between the matrix grain size and the size or amount of second phase particles. Since the early work of Zener, the particle pinning effect has been of continuing interest. According to the analysis of Hellman and Hillert [Hel 75], the matrix grain size,  $d$ , is 1.8 times that of the particle size,  $r$ , normalized by the cube root of the volume fraction,  $v$ , of the second phase. This is equivalent to having 6 pinning particles, on an average, for every grain. In this model, the grains are subject to three dimensional pinning by particles residing at grain corners. It has to be noted that the Hellman and Hillert model assumes equilibrium and the prediction is for the limiting grain size.

It is also to be noted that the beneficial effect of a second phase on resisting coarsening is lost when a significant amount of liquid phase is present in the sample, It is to be noted that in such instances, grain growth occurs by Ostwald ripening via solution, diffusion, and reprecipitation through the liquid phase, and static and dynamic grain growth cannot be suppressed merely by the introduction of second phase inclusions.

### 2.10.3 Characteristics of Superplastic Deformation

Although there is a general agreement that deformation mechanisms in superplasticity are similar to diffusional creep, definitive identification of specific mechanisms has not been successful. Reviewing the superplastic deformation data from several metals reveals that, in several important aspects, superplasticity differs from diffusional creep. First, the grain shape change after large deformations is remarkably small, contrary to those envisioned in diffusional creep models. Second, the contribution from grain boundary sliding is unusually large, compared to diffusional creep. Third, the stress and grain size exponents are often substantially different from the prediction of simple diffusional creep models. These discrepancies have motivated the development of several models which modify the conventional descriptions of diffusional creep for superplastic conditions. Particular attention is drawn to such concepts as grain switching,



grain rotation, and grain shape transformation, as well as to the enhanced roles of grain boundary sliding and grain boundary migration. Some models also envision an interplay of the diffusional processes and (grain boundary or lattice) deformation processes. It should be noted that these models are largely qualitative and fail to quantitatively account for the observed rates of superplastic deformation.

#### 2.10.4 Effect of a Second Phase on the Superplastic Deformation Characteristics

An essentially insoluble second phase can have two effects on the deformation resistance of a fine grained material: (a) a modification of the continuum deformation mechanics and (b) a change in the interface related deformation characteristics. The first effect can be treated and understood from continuum mechanics considerations in that the deformation resistance of a composite may be determined entirely by knowing the deformation resistance of the constituent phases, after computing the effective stress and strain distributions in the two phase composite. The second effect is microscopic, usually localized to grain boundaries and interfaces between phases, and arises from the alteration of the diffusion path, diffusion rates, and interface reactions due to chemical or structural modifications of the interface itself or interfacial phases. Although the continuum effect becomes significant only at higher volume fractions (e.g. 20 v/o) of the second phase, the microscopic effect can be pronounced with only trace amounts of additives.

For the case of rigid second phase inclusions embedded in a matrix, a continuum model, which pictures the composite flow as a non newtonian fluid containing rigid particulate has been appropriately developed by Chen. According to this rheological model, the strain rate of the composite is expressed as

$$\dot{\epsilon} = (1 - v)^{(2+n)/2}$$

where  $v$  is the volume fraction of the rigid inclusions,  $\dot{\epsilon}_0$  the strain rate of the reference matrix (taken as one with an identical grain size but without inclusions). Data on 2Y-TZP containing up to 80 v/o mullite are in very good agreement with this model.

### 2.10.5 The Threshold Stress and Its Origin in Superplastic Materials

By far, the most popular explanation for the origin of the threshold stress has been in terms of the action of the grain boundaries as imperfect sources and sinks for vacancies (interface reaction control). As at elevated temperatures there is an inverse relation between the strain rate and the grain size, the magnitude of the threshold stress could become significant when the grain size is small. Physically this means that more time is taken for the creation and annihilation of the vacancies than their motion. The activation energy will then be equal to that needed for the emission or the absorption of vacancies. Alternatively, a threshold stress could arise from the need for the multiplication of grain boundary dislocations when this process is an essential part of the mechanism that gives rise to the creation and annihilation of point defects. For example, the condensation or the emission of vacancies could occur by the glide/climb of dislocations in the grain boundary regions.

To date, the Ashby-Verall model [Ash 73] represents the only detailed analysis that provides a physical basis for the origin of the threshold stress in superplastic alloys. The development of their two dimensional model (applicable in the case of single phase materials containing equiaxed grains) differs from the Nabarro-Herring and Coble mechanisms in topological details. In this case, non-uniform flow leading to grain switching prevents significant grain elongation. Strain is produced by the relative translation of grains which also causes an increase in the number of grains along one of the two orthogonal directions. When these grains are not perfect hexagons, the translation of the grains will also produce a rotation. The switching of the (grain) neighbors, on the other hand, will lead to large specimen elongation without altering the shape and size of

the grains significantly. Figure 2-13 schematically illustrates this grain switching mechanism the diffusional accommodation that is necessary at the intermediate stage of the grain switching event, so that void formation of the boundaries is present.

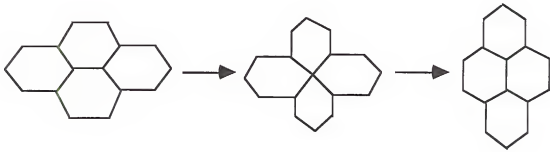


Figure 2-13 Schematic of the grain switching mechanism for superplastic materials

An idealized, two dimensional cluster of four grains constitutes a basic unit. As a result of the flow, the shape of a group of grains as a whole changes but the shape of the individual grains remains unaltered. The grains, however, suffer accommodation strain by grain boundary diffusion and this prevents them from remaining together. The external stress applied performs the work necessary to drive the following four irreversible processes:

(a) Diffusional Process: A temporary change in the shape of the grains due to the volume or grain boundary diffusion results due to the need for accommodation. The power dissipated by this process is proportional to the total flow rate of vacancies or atoms, as well as the average chemical potential difference between the sinks and source.

(b) Interfacial reaction: When the boundaries act as imperfect sources or sinks for point defects, an interface barrier has to be overcome before a vacancy can be removed or added to a boundary. The magnitude of the chemical potential barrier could be different

for the sources and sinks. Here again, the power dissipated would depend on the magnitude of the chemical potential difference and the flow rate of vacancies (atoms).

(c) Grain Boundary Sliding: Work has to be done against the grain boundary viscosity before sliding (shear displacements in the boundary plane which lead to the relative translation between grains) can take place. The power dissipated in this process is the product of the resolved shear stress on the boundary, the area of the boundary, and the velocity of sliding. Although the sliding contribution here in this case is greater than that obtained by Nabarro-Herring or Coble mechanisms, the power dissipated is negligible.

(d) Fluctuations in boundary area: Energy is stored when a group of four grains changes from the initial to the intermediate configuration, but gets released (as heat) once the original shape is restored. The power dissipated is proportional to the specific free energy of the boundary and the *rate of change* of boundary area. Thus, the creation of the additional surface area (grain boundary area *fluctuations*) is the major contributor to the power dissipation and is thought to give rise to a threshold stress below which flow is not possible.

Ashby and Verrall note that the diffusional accommodation requires a much shorter path length than envisaged in the Nabarro-Herring model since matter only has to be transported in the region of the triple points rather than across entire grains. Geometrically, they calculated that the amount of matter transported per unit strain is  $\sim 0.1 d^3$  in grain-switching creep, compared to  $d^3$  in Nabarro-Herring creep. Thus the creep rate is enhanced tenfold.

## CHAPTER 3 PROCESSING

This chapter focuses on the rationale and development of a method of synthesis of low-oxygen  $\text{MoSi}_2$  based composites starting from elemental powders. It will be shown that the glassy  $\text{SiO}_2$  phase characteristic of conventional powder processed  $\text{MoSi}_2$  can be effectively eliminated through this processing strategy which combines mechanical alloying, carbon additions, and an *in-situ* carbothermal reduction reaction. The interplay between the phase formation sequence in the powders and the microstructural evolution in the consolidated samples derived through this process (hereafter referred to as the University of Florida (UF) process) will be described. It will also be shown that a uniform distribution of micron-sized  $\text{SiC}$  reinforcements in an  $\text{MoSi}_2$  matrix are formed in the UF composites. The role of important processing variables such as the nominal alloy composition, milling media effects, consolidation temperatures, and consolidation atmospheres will also be discussed, as they relate to the final microstructure, based on our understanding of the Mo-Si-C system as well as from evidence obtained from DTA, TGA, TEM and XRD.

### 3.1 Introduction

The previous Chapters have established that while  $\text{MoSi}_2$  has long been considered a potential high temperature structural material, its commercial realization has been impeded by its low ambient temperature fracture toughness and poor elevated temperature strength. Furthermore, significant challenges need to be overcome with

regard to its processing, in view of its high melting point, its narrow solubility range (line compound), and its relatively high dissociation pressures at elevated temperatures [Cha 74, Sea 60]. While powder processing routes thus seem to be a preferable alternative due to the potentially lower processing temperatures that they afford, they also result in silica incorporation into the microstructure. The presence of grain boundary silica either as a continuous film or as discrete particles is expected to be detrimental since the particles may serve as crack nucleation sites at lower temperatures, while enhancing deformation via grain boundary sliding at temperatures above 1200°C where the silica softens appreciably. In fact, recent studies have shown that low-silica, polycrystalline MoSi<sub>2</sub> demonstrates negligible "plasticity" below 1400°C [Aik 92]. Silica formation also alters the matrix stoichiometry and results in the formation of Mo<sub>5</sub>Si<sub>3</sub>. Such stoichiometric deviations degrade the intermediate temperature oxidation resistance [Mes 92] of the silicide. Finally, silica has also been reported to cause the degradation of the diffusion barrier coatings at the fiber-matrix interface in ductile fiber reinforced MoSi<sub>2</sub> [Xia 92].

In attempting to control the oxygen content of MoSi<sub>2</sub> by varying the starting powder size and by intentional carbon additions (deoxidant), Maxwell [Max 52] found that a fine grained material with carbon additions had better creep properties and lower high temperature plasticity than a similar grain size material without carbon. More recently, Maloy et al. [Mal 91] also reported improved elevated temperature fracture toughness with varying levels of carbon additions. However, substantial (~40 %) weight losses were reported on consolidating these samples, resulting in uncontrolled formation of Mo-rich second phases. Hardwick and coworkers [Har 92] attempted to process oxygen-free MoSi<sub>2</sub> by conducting all the powder handling and consolidation steps under vacuum or inert gas atmospheres. However, these approaches [Har 92, Sch 92] are impracticable from the standpoint of processing bulk structural parts, due to the difficulties involved in the scale-up of the evacuation systems, as well as the excessive costs that would be associated with such processes.

It is therefore clear that further enhancements in the properties of  $\text{MoSi}_2$  and  $\text{MoSi}_2$  based composites are possible only with the elimination of silica (and oxygen) in the matrix along with close control of the overall stoichiometry, through the use of simple and economical processing schemes which do not necessitate elaborate care during powder handling. Thus, the major focus of the present study was to achieve the above mentioned objectives through a combination of mechanical alloying and carbothermal reductions for the silica-free synthesis of  $\text{MoSi}_2$ .

## 3.2. Background

### 3.2.1 Phase Equilibria

Optimizing the processing parameters and understanding the microstructural evolution requires an understanding of the phase equilibria and crystal chemistry of the binary Mo-Si and the ternary Mo-Si-C systems; these have been summarized in Table 2-1 in Chapter 2.

Ternary phase equilibria in the Mo-Si-C system have been discussed in Chapter 2. However, in view of the pertinence of the data to the processing rationale, we reiterate some of the salient features of the ternary phase equilibria of the system, as briefly described below.

Broadly speaking, two versions of the ternary Mo-Si-C isotherm are in existence, as shown in Fig. 2-5. The earlier versions were constructed by Nowotny and co-workers [Now 54] and by Brewer and Krikorian [Bre 56] at  $1600^\circ\text{C}$  and  $1727^\circ\text{C}$ . A  $1200^\circ\text{C}$  version of the isotherm was later constructed by Van Loo and co-workers [Van 82]. The only ternary phase in this system is the so called "Nowotny phase" which has the approximate formula  $\text{C}_{\leq 1}\text{Mo}_{\leq 5}\text{Si}_3$  and a relatively wide homogeneity range [Now 54, Par 65, Bre 56, Van 82]. While the isotherms of Nowotny et al. and Brewer et al. are in good agreement with each other in their prediction of the existence of a three-phase field

between  $\text{MoSi}_2$ ,  $\text{C}_{\leq 1}\text{Mo}_{\leq 5}\text{Si}_3$  and  $\text{SiC}$ , the Van Loo isotherm indicated the coexistence of  $\text{Mo}_5\text{Si}_3$ ,  $\text{SiC}$ , and  $\text{C}_{\leq 1}\text{Mo}_{\leq 5}\text{Si}_3$  at  $1200^\circ\text{C}$ . Subsequent analysis seems to support the Brewer and Nowotny diagrams.

Attention is also drawn at this point to the liquidus surface projections of the Mo-Si-C diagram (Fig. 2-6), with particular reference to the ternary eutectic between  $\text{C}_{\leq 1}\text{Mo}_{\leq 5}\text{Si}_3$ ,  $\text{MoSi}_2$  and  $\text{SiC}$  at  $1850^\circ\text{C}$ , and the quasi-binary eutectic between  $\text{MoSi}_2$  and  $\text{SiC}$  at  $1900^\circ\text{C}$ . These determine the upper limits of the processing temperature in powder consolidation approaches.

It is also instructive to consider the rather high dissociation tendencies of the silicide (refer back to Section 2.1.1), in view of its high vapor pressure at temperatures above  $1500^\circ\text{C}$ . The relevance of this aspect will be elaborated in the forthcoming sections.

### 3.2.2 Processing Rationale

The preceding chapters/sections have firmly established the need for the development of a process for the elimination of silica (and oxygen) from  $\text{MoSi}_2$  and  $\text{MoSi}_2$  based composites in order to enhance the properties of  $\text{MoSi}_2$ . Furthermore, the need for the close control of the overall stoichiometry of the process was also emphasized. A further requirement of such a processing scheme would be the simplicity, economy, and robustness of the process which would not necessitate elaborate care during powder handling.

The primary aim of the present investigation is to form low oxygen (low silica) content composites comprised of silicides and silicon carbide. To attain this objective, use is made of the carbothermal reduction reaction in order to reduce the silica to silicon carbide. Carbon, the essential element necessary to deoxidize the matrix, is incorporated through mechanical alloying.



The processing of oxygen-free  $\text{MoSi}_2$  by carbon additions requires the following two considerations:

- (1) Elimination of the  $\text{SiO}_2$  through its conversion to  $\text{SiC}$ .
- (2) Prevention of silicon volatilization.

Accordingly, a unique process was conceived for the silica-free synthesis of  $\text{MoSi}_2$ , which was based on a combination of mechanical alloying and carbothermal reductions. While the mechanical alloying (MA) results in the formation of microstructurally uniform and compositionally homogeneous alloys of the desired stoichiometry, due to its high energy intermixing of elements through interparticle collisions and repeated fracture, the carbothermal reduction process [Wei 83, Ish 90] would utilize the reducing effect of carbon to convert silica to silicon carbide. Furthermore, mechanical alloying would enable the homogeneous incorporation and dispersion of carbon in the matrix to facilitate these reactions. A further advantage of the mechanical alloying process was the potentially lower powder sizes it would produce; this, in turn, would lead to lower densification temperatures.

Based on the  $1600^\circ\text{C}$  isotherm of Nowotny and the  $1727^\circ\text{C}$  isotherm of Brewer, it is clear that ternary powder alloys within the composition limits established by the  $\text{MoSi}_2 + \text{C} \leq 1\text{Mo} \leq 5\text{Si}_3 + \text{SiC}$  three-phase field should form a *thermally stable*, three-phase microstructure when consolidated at these temperatures, provided that the powders are sufficiently homogeneous to minimize the diffusion length scales so as to establish equilibrium within the short time frames of the consolidation process. Here, it is assumed that the nature of the isotherms is unaltered by the presence of small amounts of oxygen present as surface  $\text{SiO}_2$  on the powders. The advantage of using carbon as the deoxidizing agent is obvious when one examines the phase relations; while part of the carbon will effect the deoxidization /carbothermal reduction reaction, the unreacted residual carbon will exist in equilibrium with  $\text{MoSi}_2$ , either in the Nowotny phase or as  $\text{SiC}$ , as the isotherms would dictate.

It is clear that for the formation of  $\text{MoSi}_2/\text{SiC}$  composites with minimal amount of the Nowotny phase, it is necessary to start with nominal compositions close to but slightly to the Mo-rich side of the  $\text{MoSi}_2\text{-SiC}$  tie line, so that compositional variations (carbon and silicon losses) as a result of both the carbothermal reduction reactions and  $\text{SiO}$  volatilization do not shift the overall composition to the adjacent  $\text{Si} + \text{SiC} + \text{MoSi}_2$  field, where incipient melting of silicon above  $\sim 1400^\circ\text{C}$  is expected. Adequate care should be taken to avoid the molybdenum-rich side of the tie-line, which would lead to formation of the  $\text{C}_{\leq 1}\text{Mo}_{\leq 5}\text{Si}_3$  phase. Bearing this in mind, it is possible to vary the amount of the reinforcing  $\text{SiC}$  phase in the  $\text{MoSi}_2$  matrix by simply choosing compositions at various points along the tie line, while accounting for the losses already mentioned.

It should be mentioned here that the use of *three* elemental powders allows for a greater degree of latitude with regard to the range of starting powder compositions accessible within the Mo-Si-C system. This is in direct contrast to other approaches which use mixtures of 2 components to form *in-situ* composites, such as a mixture of  $\text{Mo}_2\text{C}$  and Si, as employed by Henager and coworkers [Hen 92, Hen 93]. An obvious consequence of this methodology is that it restricts the range of compositions to those along the line joining the two components. For  $\text{MoSi}_2\text{-SiC}$  composites, this approach restricts the volume fraction of  $\text{SiC}$  formable through the process to a single composition determined by the intersection of the  $\text{MoSi}_2\text{-SiC}$  and  $\text{Mo}_2\text{C-Si}$  connects. While the problem can be circumvented somewhat by the incorporation of a third component such as carbon, the range of compositions achievable still does not cover the entire compositional range of the Mo-Si-C system. Taking the specific example of the  $\text{Mo}_2\text{C-SiC}$  combination, it is apparent that the composition range of the powders is delimited by the triangle covering these compositions. Consequently, the range of  $\text{MoSi}_2/\text{SiC}$  composites is restricted to those which lie along the  $\text{MoSi}_2/\text{SiC}$  tie line, but above the intersect of the  $\text{MoSi}_2\text{-SiC}$  and  $\text{Mo}_2\text{C-Si}$  interconnects. The second phase volume fractions formed using the above rationale are somewhat high (in the range of 30 v/o) for

the MoSi<sub>2</sub>-SiC system, and, due to the pinning effects of such reinforcements, result in the production of fine microstructures, which are desirable for formability, but not for creep strength considerations.

We note that the formation of the thermodynamically expected microstructures is also limited by the interface reaction kinetic constraints. Similarly, processing related effects such as porosity should also be appropriately controlled in view of the gaseous by-products formed as a result of the carbothermal reduction reaction.

It is worth noting that the deoxidization of commercial MoSi<sub>2</sub> by carbon additions without a commensurate increase in the silicon content [Max 52, Mal 92] would result in compositional shifts along an imaginary line between MoSi<sub>2</sub> and C and a corresponding increase in the amount of the Nowotny phase (Fig. 2-5a).

In line with the rationale expressed in the preceding paragraphs, the processing studies were carried out to explore the possibility of room temperature synthesis of silicide matrices, specifically with low oxygen contents through mechanical alloying of powders and subsequent hot pressing (hereinafter referred to as the University of Florida (UF) process). Within this broad framework, the study had the following objectives: (1) characterization of the UF process (as a function of variables such as carbon content) in terms of the phase evolution, thermogravimetry and microstructure evolution (2) Comparison of the efficacy of the UF process to conventional "blend and consolidate" powder metallurgy processes (hereinafter also referred to as the conventional process (CP)), specifically in terms of the homogeneity and phase content of the fully consolidated microstructures.

For purposes of carrying out task 1 outlined above, two powder compositions were chosen for mechanical alloying (MA). The first corresponded to stoichiometric binary MoSi<sub>2</sub> (Si-33.33 Mo, all compositions in atomic percent), primarily as a baseline for comparison while the other was a ternary alloy (Si-28 Mo-14 C) in the MoSi<sub>2</sub> + C<sub>≤1</sub>Mo<sub>≤5</sub>Si<sub>3</sub> + SiC three phase field. Task 2 entailed the comparisons of consolidated

microstructures derived from the same composition (Si-28 Mo-14 C), but processed using two different routes, namely mechanical alloying of elemental powders and conventional blend and consolidation of commercial  $\text{MoSi}_2$  and carbon. In addition,  $\text{MoSi}_2/\text{SiC}$  composites processed by the UF and CP routes were also compared. For the production of  $\text{MoSi}_2/\text{SiC}$  composites, alloys of nominal composition, Si-25 Mo-14 C and Si-19 Mo-23 C, corresponding to 20 and 40 v/o SiC were chosen.

### 3.3 Experimental Procedure

#### 3.3.1 Raw Materials

Table 3-1 lists the characteristics of pertinent raw materials used in this investigation.

Table 3-1 Specifications of the raw materials used

Raw Material	Purity (weight %)	Size	Vendor
Molybdenum	99.9%	2-4 $\mu\text{m}$	Cerac
Silicon	98%,	< 44 $\mu\text{m}$	Cerac
Carbon, amorphous	99.5 %	-300 mesh	Johnson Matthey
$\text{MoSi}_2$ (Powder)	99.9%	-325 mesh	Johnson Matthey
SiC (Powder)	99.9%	< 1 $\mu\text{m}$ avg. diameter	Cerac

### 3.3.2 In-situ Composites

#### 3.3.2.1 Mechanical Alloying

Mechanical alloying was performed in a Szegvari attrition mill (planetary type) using hardened steel balls as the milling media and a ball to charge ratio of 5:1. In view of the potential compositional deviations that would arise as a result of the powders coating the milling media, the mill and the media were specially treated prior to the commencement of a run. For this purpose, the attritor and the charge media were thoroughly cleaned with deionized water, followed by an acetone wash to facilitate quick drying of the mill as well as to avoid rusting of the mill and the milling media. Following the drying, the attritor was loaded with a sacrificial charge of MoSi<sub>2</sub> powder, allowed to run for an hour, and the powder discharged. The above procedure coated a thin layer of the silicide on the walls of the attritor and the surface of the milling media. Attrition was commenced following this procedure. Elemental powders of commercial purity molybdenum (purity 99.9%, 2-4  $\mu\text{m}$ ) and silicon (purity 98%, < 44  $\mu\text{m}$ ) obtained from Cerac and high purity carbon powder (99.5 % pure, -300 mesh, amorphous) obtained from Johnson Matthey were the starting materials. To ensure uniformity of the elemental powder mixture prior to loading in the attritor, the powders were tumble-blended in a rotary mill using teflon containers. Oxygen contamination during processing was minimized by maintaining an atmosphere of high purity titanium-gettered argon (oxygen content less than 4 ppm) under a slightly positive pressure in the attritor. The powders were loaded at an attritor speed of 200 rpm, and subsequently the attritor speed was ramped up to 500 rpm for the duration of the run. The progress of MA was monitored by withdrawing small amounts of powder samples from the same attrition batch after 0, 0.5, 7, 17, 29, 40 and 42 hours of milling. These powders were later characterized for structure and morphology by SEM and XRD.

Subsequent to the mechanical alloying process, the powders were stored in glass bottles. It is emphasized here that the powders were stored under ambient environment in closed bottles, and that they did not require any special care while handling or storage.

### 3.3.2.2 Thermogravimetry

The transformation characteristics of the MA powders were monitored by differential thermal analysis (DTA) and thermogravimetric analysis (TGA). DTA/TGA was performed under flowing gettered argon (1cc/min, oxygen content less than 4 ppm) on a Netzsch STA-409 system with heating/cooling rates of 10°C per minute. Errors due to the differing specific heats of the sample and the reference were eliminated by using commercial MoSi<sub>2</sub> powder which had been previously calcined under gettered argon at 500°C as the reference. For more detailed investigations, powders were heated at 10°C/min under gettered argon above each DTA exotherm, held at that temperature for less than a minute, and rapidly cooled for subsequent analysis.

Structural analysis of the mechanically alloyed powders and the consolidated samples was carried out using a Philips ADP 3720 diffractometer operated at 40 kV and 20 mA with Cu K $\alpha$  radiation and digital data acquisition over 2 $\theta$  ranges of 5°-100°. While the as-alloyed powders were mounted on glass slides using a colloidal solution, the analysis of bulk samples was conducted on thin flat sections (~1 mm thickness) ground to 600 mesh finish, and mounted on slides. Phase identification was accomplished in the Major Phase and Isotypical modes of the JCPDS% data base search routines.

### 3.3.2.3 Powder Consolidation

As noted in the previous sections, the processing of silica-free MoSi<sub>2</sub> by carbon additions requires the following important considerations:

(1) Elimination of the SiO<sub>2</sub>: This is achieved through its conversion to SiC, with the overall reaction generally represented as

---

% PC-PDF card retrieval and display system and PDF-2 Data Base by JCPDS-ICDD, Swarthmore, PA.



The thermodynamics of this reaction indicate that it is feasible above 1450°C. In order for the above deoxidization reaction to proceed in the forward direction (SiC formation), the gaseous byproducts (for example, CO) of the reaction must be removed. If this were not properly accomplished, considerable amounts of entrapped porosity would develop in the compact. Thus, vacuum levels of better than  $10^{-3}$  torr are necessary in order to evacuate the product gases from the compact. A subtle point to be noted herein is the need for providing sufficient open porosity in the compact prior to and during the deoxidization reaction so as to facilitate easy evacuation of the product gases from the bulk, including the core region of the compact. Upon completion of the deoxidization, however, all porosity (open and closed) needs to be minimized or eliminated.

## (2) Prevention of silicon volatilization:

As alluded to in Chapter 2, silicide bodies exhibit high vapor pressures at temperatures above 1550°C, which results in their dissociation to silicon vapor and the next higher silicide at pressures below half an atmosphere. Furthermore, the dissociation tendency exhibits a significant increase with an increase in temperature. Thus, conditions typically present during consolidation (low dynamic vacuum levels and temperatures above 1550°C) are conducive to silicide dissociation and result in the progressive evaporation/loss of the elemental silicon from the silicide body in the form of silicon vapor. The final body would then not possess the desired stoichiometry or microstructure (in our case, a mixture of silicon carbide and the disilicide), but would be sub-stoichiometric (with respect to silicon) and contain indeterminate amounts of silicon-lean phases. However, such silicon losses are avoidable by maintaining the ambient pressure of the hot pressing chamber at a level greater than the dissociation pressure at that temperature.

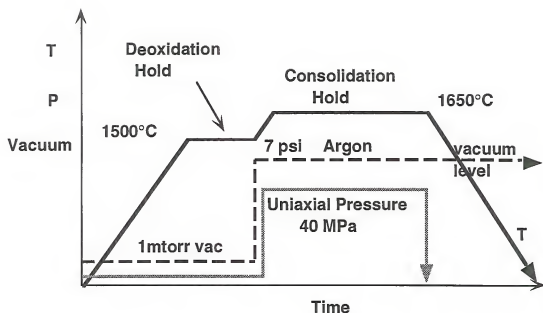
It is thus apparent that maintaining a constant vacuum atmosphere or a constant argon (overpressure) atmosphere during the entire duration of hot consolidation of the

alloyed Mo-Si-C powder will not yield the desired microstructures, due to the conflicting atmospheric pressure requirements of the deoxidization and silicon volatilization reactions. Maintaining vacuum levels of better than  $10^{-3}$  torr throughout the duration of the hot consolidation process, while efficiently removing the entrapped gases at lower temperatures, would also lead to silicon volatilization from the surface at temperatures above  $1550^{\circ}\text{C}$ . Conversely, maintaining a argon overpressure throughout the duration of the consolidation experiment, while effectively suppressing silicide dissociation and the resultant silicon volatilization, retards deoxidization and removal of gaseous by-products and therefore would potentially result in synthesis of porous samples.

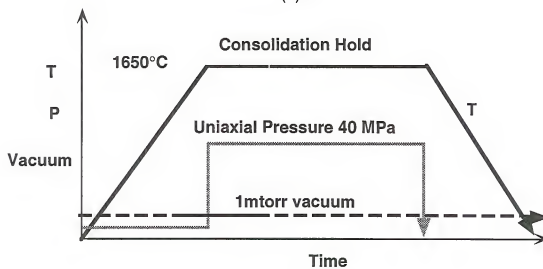
Thus, the derivation of the optimum microstructures in the UF materials requires the performance of the consolidation process in two stages, as shown in Fig. 3-1a. For comparison, the processing conditions of conventional hot pressing cycles are shown in Fig. 3-1b. The first stage of the modified hot pressing cycle (Fig. 3-1a) envisages the MA powder to be loaded in dies and a very low pressure (less than 10 MPa) applied to the cold compact, so that the sample has sufficient open porosity for the entrapped gases to escape during the degassing and silica reduction reactions. To achieve deoxidization, the sample is ramped up to  $1450\text{--}1500^{\circ}\text{C}$  and held at that temperature under a dynamic vacuum of 1 millitorr or less for at least 30 minutes to deoxidize the matrix. Subsequently, the densification and pore closure operations are effected by heating the sample to between  $1600\text{--}1650^{\circ}\text{C}$  under an argon environment (7 psi) and holding for an hour under sufficient uniaxial pressure (typically 35-40 MPa). The compaction pressure is subsequently released and the sample cooled to room temperature at  $10^{\circ}\text{C}/\text{min}$ .

It is emphasized that processing variables such as the temperature and the vacuum levels need to be carefully controlled while processing  $\text{MoSi}_2$  and  $\text{MoSi}_2/\text{SiC}$  composites. Fig. 3-2 is a backscattered electron image of the surface of a the MA40 material that had undergone silicon volatilization after being hot pressed under a vacuum of less than  $10^{-3}$





(a)



(b)

Figure 3-1 Schematic of the hot consolidation cycle for the processing of  $\text{MoSi}_2/\text{SiC}$  composites: (a) modified cycle which minimizes silicon losses during consolidation, and (b) conventional cycle which could lead to potential silicon loss during processing.

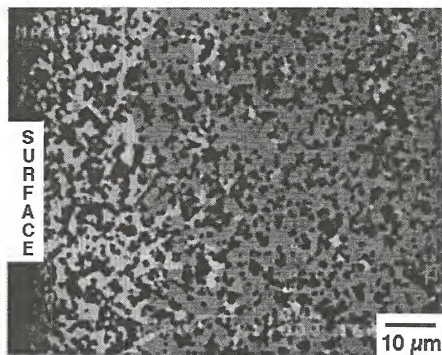


Figure 3-2 Backscattered electron image of area of hot pressed sample from UF MoSi<sub>2</sub>/40 SiC, showing a silicon depleted surface layer. [light phase is the Nowotny phase, grey is MoSi<sub>2</sub>, dark phase is SiC].

torr at 1700°C for one hour. Similar effects due to silicon volatilization have been reported during the processing of monolithic MoSi<sub>2</sub> [Che 64].

Thus, consolidation of the MA binary powders was carried out by hot pressing under a vacuum of 10<sup>-2</sup> torr or less in an inductively heated graphite die at 1450°C, while the ternary powders were subject to a processing cycle based on the rationale expressed in the preceding paragraphs, and as depicted in Fig. 3-1a. To ensure easy removal of the consolidated samples, the die walls and the plunger were coated prior to powder loading with a thin layer of boron nitride spray. A thin layer of grafoil was also used to line the die walls, as well as a spacer between the plunger and the powders, for the same purpose. The die temperature was measured with the help of a two color pyrometer (Capintec) with accuracies of +25 -20°C over the range of temperatures measured. To prevent cracking of the sample, the pressure was released prior to cooling.

### 3.3.3 Conventionally Processed (CP) Composites

For purposes of comparison, composites with 20 and 40 v/o SiC reinforcement were fabricated using the conventional approach of dry blending MoSi<sub>2</sub> (99.9% pure, -325 mesh, Johnson Matthey) and SiC powders (< 1 µm average diameter, 99.9% pure, Cerac) in the appropriate proportions in teflon containers followed by hot consolidation (hereafter designated as CP20 and CP40). Monolithic MoSi<sub>2</sub> was also processed from commercial MoSi<sub>2</sub> powder (99.9% pure, -325 mesh, Johnson Matthey). In order to facilitate the meaningful comparison of properties between the CP and compositionally tailored *in-situ* UF composites produced by mechanical alloying, the size distribution of the SiC powders for the CP composites was chosen such that they matched the reinforcement sizes in the *in-situ* processed UF material. Hot pressing of the CP composites was performed in graphite dies under a vacuum of 10<sup>-3</sup> torr or better, with a pressure of 35 MPa at 1600°C for a hold time of 1 hour. Subsequently, samples were cooled at the rate of 10°C/min to room temperature.

### 3.3.4 Microstructural Characterization

Samples for microstructural characterization were electro-discharge machined on a numerical controlled Brother HS-100 wire EDM<sup>#</sup>, ground on 60 to 180 grit SiC paper to remove the EDM recast layer, and then final grinding (240 through 600 grit SiC paper), and polished successively on 6  $\mu\text{m}$  and 3  $\mu\text{m}$  diamond and finally to a 1  $\mu\text{m}$  diamond finish. Following this, samples were ultrasonically cleaned in deionized water and detergent solutions prior to microstructural examination, as well as between all polishing operations.

Grain boundary contrast in large grained  $\text{MoSi}_2$  samples is easily revealed by polarized light microscopy, because of its anisotropic optical response. However, this technique is unsuitable at grain sizes less than 10  $\mu\text{m}$  because of limitations in the resolution and light source intensity. Attempts to enhance grain contrast in  $\text{MoSi}_2$  samples by etching were unsuccessful.  $\text{MoSi}_2$  grain boundaries were generally found to respond very poorly to most common etchants. Various techniques such as wet etching in  $\text{HF} + \text{HNO}_3$  mixtures, as well as by boiling for 30 s in mixtures of 10%  $\text{NaOH}$  and  $\text{K}_3\text{Fe}(\text{CN})_6$  [Potassium Ferricyanide], failed to reveal the grain boundaries. Rather, these etchants usually attacked the silica, thereby providing spurious contrast.

Microstructural analysis of the consolidated samples as well as the MA powders was performed using a JEOL JSM 6400 SEM equipped with a Tracor Northern EDS unit with light element detection capabilities and JEOL 200CX and JEOL 4000FX TEMs, the latter equipped with a Princeton Gamma Tech (PGT) EDS unit with a light element detector. Electron microprobe analysis (EMPA) was conducted using a JEOL 644 using  $\text{Al}_2\text{O}_3$ , SiC and Mo as the standards and using a quantitative correction program (PROZA). Analysis was performed using a broad beam ( $\sim 50 \mu\text{m}$ ) as well as focused probe ( $\sim 1 \mu\text{m}$ ).

---

<sup>#</sup> Japanese manufacturer, serviced in the US by Charmilles Technologies, OH.

### 3.3.4.1 TEM Sample Preparation

Powders obtained after 17 and 40 hours of milling were analyzed by TEM. For the TEM analysis, powders were ultrasonically dispersed in acetone and a small droplet was spread on a holey carbon film. The fine size ( $<1\text{ }\mu\text{m}$ ) of the powders ensured their electron transparency.

Thin foil TEM specimens were prepared from the bulk samples as well. For this purpose, 1 mm thick slices were diamond saw cut and ground down to  $500\text{ }\mu\text{m}$  using SiC paper. Following this, 3 mm diameter discs were cut using an ultrasonic drilling tool. The 3 mm slices were then ground down to close to  $100\text{ }\mu\text{m}$  using 600 grit SiC paper. Final thinning to between  $50\text{--}70\text{ }\mu\text{m}$  was performed with  $6\text{ }\mu\text{m}$  diamond paste in a Gatan Dimpler using a flat profiled dimpling tool. In view of the brittle behavior of the samples, dimpling with the arc-profiled dimpler was not very successful. To avoid sample breakage during handling, the samples were then mounted on annular 3 mm copper rings using a thermally setting M-Bond adhesive. Samples were then ion-milled to perforation using a Gatan argon ion-mill operating at 4.5 kV, and an incidence angle of between  $25$  and  $30^\circ$ . Final thinning after the initial perforation was done at incidence angles of  $12\text{--}15^\circ$  to derive the maximum thin area for subsequent TEM analysis.

## 3.4. Results and Discussion

### 3.4.1 In-situ Composites

#### 3.4.1.1 Powder Microstructure

The development of the powder morphology with increasing milling times is shown in Fig. 3-3. After 0.5 h of milling (Fig. 3-3c), large particles with a diameter of  $5\text{--}6\text{ }\mu\text{m}$  are predominant. Refinement of the powder continues through 7 h of milling (Fig. 3-3d), beyond which the reduction in powder size gradually slows down. The powder size stabilizes around  $1\text{ }\mu\text{m}$  after 29 hours (Fig. 3-3e) and remains constant.

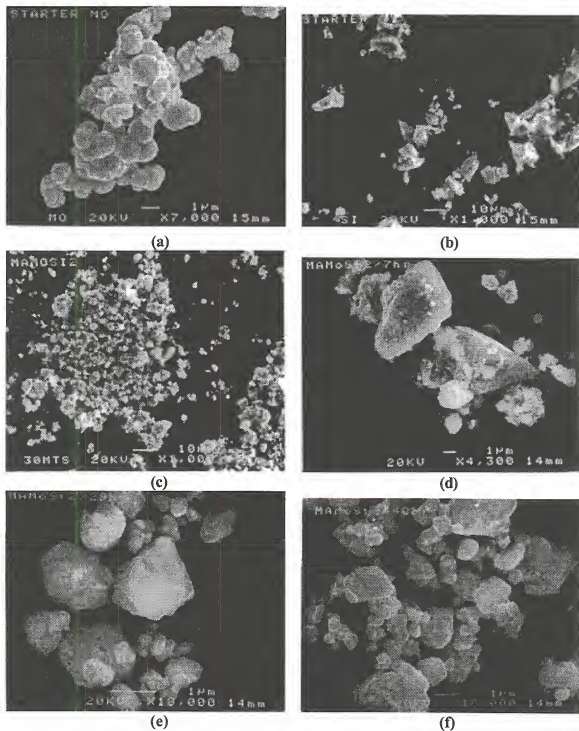


Figure 3-3 Morphological evolution of the MA MoSi<sub>2</sub> powders as a function of milling time showing the progressive reduction in powder size and subsequent stabilization of powder size after 29 h: (a) and (b) Elemental Mo and Si powders prior to milling (0 h) (c) after 0.5 h of milling (d) after 7 h of milling (e) after 29 h of milling and (f) after 40 h of milling.

thereafter (Fig. 3-3f).

Structural evolution studies of the powders as a function of milling time (Fig. 3-4) indicated the formation of traces of  $\beta$ -MoSi<sub>2</sub> (hexagonal form) after short milling times (0.5 h, see Fig. 3-4a). Further milling (7 h, Fig. 3-4b) results in a slight increase in the amount of  $\beta$ -MoSi<sub>2</sub> along with the gradual appearance of  $\alpha$ -MoSi<sub>2</sub> (tetragonal form). Further increases in the amount of  $\alpha$ -MoSi<sub>2</sub> continue through 17 h of milling (Fig. 3-4c), at which time elemental molybdenum and silicon are still present. Milling beyond 17 h through 29 h (Fig. 3-4d) results in the almost complete disappearance of the silicon peaks along with a considerable broadening of the  $\alpha$ -MoSi<sub>2</sub> peaks; this is presumably due to the decrease in the crystallite size of  $\alpha$ -MoSi<sub>2</sub> rather than the effect of lattice strain since MoSi<sub>2</sub> is brittle at the milling temperatures. This was confirmed by TEM observations. Beyond 29 hours, milling has little effect on the structure of the powders, a fact which was also corroborated by the SEM observations, which showed particle size stabilization after 29 hours.

Powders were characterized for their microstructure by TEM. A dark field TEM micrograph of a MA MoSi<sub>2</sub> powder particle milled for 40 hours is shown in Fig. 3-5a. Close examination reveals a fine distribution of crystallites, the sizes of which are between 4 and 7 nm. In addition, the surfaces of the powder particles appear to be covered with a layer of amorphous oxide, the projected thickness of which varies from 5 to 15 nm. The selected area diffraction pattern (SADP) (Fig. 3-5b) from this powder indexes to the interplanar spacings of Mo and  $\alpha$ -MoSi<sub>2</sub>. X-ray diffractograms (Figs. 3-6a and 3-6b) from these powders not only confirm the presence of the predominant phases (Mo and  $\alpha$ -MoSi<sub>2</sub>) determined in the TEM SADPs, but also reveal traces of the metastable  $\beta$ -MoSi<sub>2</sub>, which reportedly occurs only above 1900°C under equilibrium conditions. The formation of the  $\beta$ -MoSi<sub>2</sub> at lower temperatures is not surprising and has been reported during the annealing of amorphous Mo-Si multilayers prepared by sputtering [Loo 88, Dol 90] as well as in ion-implanted MoSi<sub>2</sub> films [dHe 80]. The

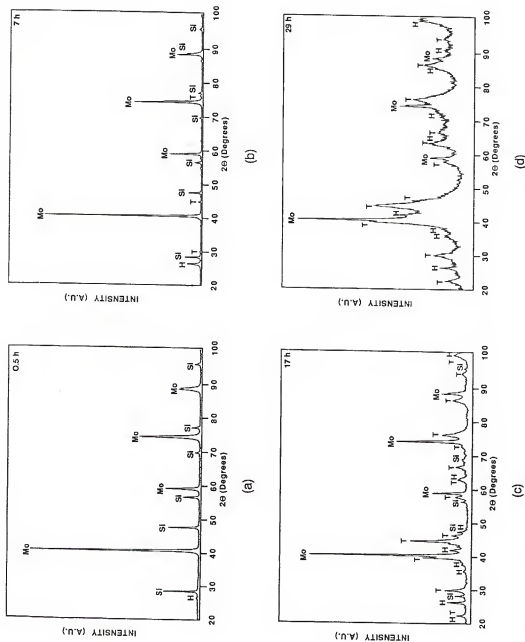


Figure 3-4 Structural evolution of the ternary MA MoSi<sub>2</sub> powder as a function of milling time: XRD patterns of the powders milled for the indicated times: (a) 0.5 h (b) 7 h (c) 17 h and (d) 29 h (Mo is molybdenum, Si is silicon, T is tetragonal α-MoSi<sub>2</sub>, H is hexagonal β-MoSi<sub>2</sub>).



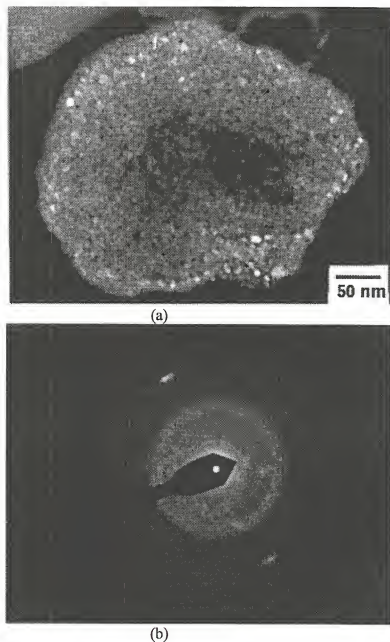
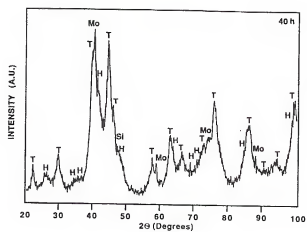
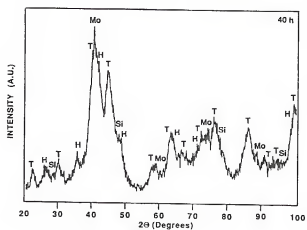


Figure 3-5 (a) Dark field TEM of the unannealed, as mechanically alloyed powder after 40 h milling, showing the distribution of fine crystallites of Mo,  $\alpha$ - and  $\beta$ - MoSi<sub>2</sub> in the micron-sized MA powder. Also note the presence of an amorphous layer surrounding the powder particle. (b) Selected area diffraction pattern from the above powder particle.



(a)



(b)

Figure 3-6 XRD of the (a) MA binary stoichiometric  $\text{MoSi}_2$  and (b) MA ternary  $\text{MoSi}_2$  (Si-28Mo-14C) after 40 h of milling. Note the relative intensities of the molybdenum and  $\alpha$ - $\text{MoSi}_2$  peaks (Mo is molybdenum, Si is silicon, T is tetragonal  $\alpha$ - $\text{MoSi}_2$ , H is hexagonal  $\beta$ - $\text{MoSi}_2$ ).

presence of Mo and MoSi<sub>2</sub> in the as-milled powders suggests that silicon is dissolved in the MoSi<sub>2</sub> and Mo crystallites; this is also a metastable effect caused by mechanical alloying, since the terminal solubilities of Si in Mo and MoSi<sub>2</sub> are negligible at room temperature, although both Mo and MoSi<sub>2</sub> are known to exist over a certain homogeneity range above ~1500°C [Bre 80, Gok 91]. The possibility of amorphization of part of the silicon was considered, but was eliminated in view of the experimental evidence against it [Koc 92]. The fine scale of the powder microstructures and the intermetallic compound formation during mechanical alloying suggest a homogeneous distribution of alloying elements. EDS analysis of the powders also revealed the presence of trace amounts of iron impurities that were probably picked up from the hardened steel balls used for milling.

In order to ascertain the possible effects of carbon additions on the final structure of the MA powders, XRD patterns from the binary (Fig. 3-6a) and ternary samples (Fig. 3-6b) after 40 hours of milling were compared. It can be seen on the basis of the relative intensities of the molybdenum and  $\alpha$ -MoSi<sub>2</sub> peaks, that the formation of  $\alpha$ -MoSi<sub>2</sub> is suppressed by the carbon additions.

#### 3.4.1.2 Phase Evolution

The phase evolution of the binary and ternary MA MoSi<sub>2</sub> powders as a function of temperature was studied by DTA. A typical heating trace of the binary MA MoSi<sub>2</sub> powder is shown in Fig. 3-7, where weak exotherms corresponding to 580°C, 780°C and 1020°C are apparent. The transformations corresponding to these exotherms were studied by XRD analysis of powders heated to temperatures above the end of each exotherm under identical heating conditions (10°C/min under flowing argon), and the results are shown in Fig. 3-8. Comparison of the room temperature and the 690°C XRD patterns (Fig. 3-6a and Fig. 3-8a respectively) showed that the mild 580°C exotherm is associated with the formation of more  $\alpha$ -MoSi<sub>2</sub> from Mo, as is evidenced by the change in the relative intensities of the  $\alpha$ -MoSi<sub>2</sub> and Mo peaks. Likewise, comparison of the

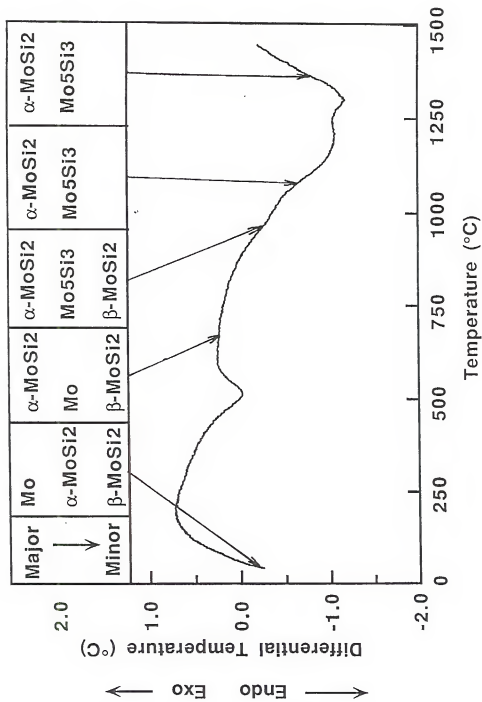


Figure 3-7 DTA of binary stoichiometric  $\text{MoSi}_2$  under flowing Ar at a heating rate of  $10^\circ\text{C}/\text{min}$ . The phase formation sequence is also schematically depicted.

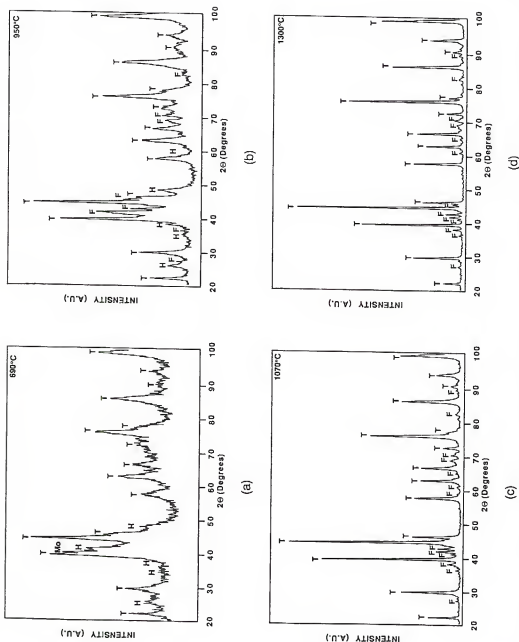


Figure 3-8 XRD of the MA binary stoichiometric  $\text{MoSi}_2$  powders heated at  $10^\circ\text{C}/\text{min}$  under flowing argon to the temperatures indicated: (a)  $690^\circ\text{C}$  (b)  $950^\circ\text{C}$  (c)  $1070^\circ\text{C}$  and (d)  $1400^\circ\text{C}$  ( $\text{Mo}$  is molybdenum,  $\text{Si}$  is silicon,  $\text{T}$  is  $\alpha\text{-MoSi}_2$ ,  $\text{H}$  is  $\beta\text{-MoSi}_2$  and  $\text{F}$  is the tetragonal  $\text{Mo}_5\text{Si}_3$  phase).

690°C and 950°C XRD patterns (Fig. 3-8a and 3-8b) shows that the 780°C exotherm corresponds to the simultaneous growth of  $\alpha$ -MoSi<sub>2</sub> and Mo<sub>5</sub>Si<sub>3</sub> (tetragonal). The 1020°C exotherm appears to be associated with the growth of  $\alpha$ -MoSi<sub>2</sub> at the expense of  $\beta$ -MoSi<sub>2</sub> and tetragonal Mo<sub>5</sub>Si<sub>3</sub>. Further heating to higher temperatures (1300°C, Fig. 3-8d) resulted in a decrease in the amount of Mo<sub>5</sub>Si<sub>3</sub> due to its transformation to  $\alpha$ -MoSi<sub>2</sub>, although minor amounts of the Mo<sub>5</sub>Si<sub>3</sub> were still apparent.

Fig. 3-9 shows the DTA trace of the ternary MoSi<sub>2</sub>. Exothermic reactions with peaks at 540°C, 875°C, 1030°C were observed. The transformation sequences of these powders were monitored in the same manner as the binary MA MoSi<sub>2</sub> powders and the results of the XRD analysis are shown in Fig. 3-10. Comparison of the room temperature (Fig. 3-6b) and 750°C patterns (Fig. 3-10a) indicates that the mild 540°C peak corresponds to the partial transformation of molybdenum to  $\beta$ -MoSi<sub>2</sub> while the analysis of the 750°C and 935°C patterns (Figs. 3-10a and 3-10b respectively) suggests that the 875°C exotherm corresponds to the formation of the carbon-stabilized C<sub>≤1</sub>Mo<sub>5</sub>Si<sub>3</sub> (Nowotny) phase at the expense of molybdenum. The possibility of this higher molybdenum silicide forming as an oxidation product rather than as a phase transformation product was also considered, but was discounted on the basis of the TGA data (discussed in detail in section 3.4.1.5), which did not show any inflections (due to weight loss or gains that are normally associated with oxidation reactions) at the corresponding exothermic temperature (875°C, Fig. 3-17). Furthermore, the 1030°C exotherm corresponds to the transformation of the Nowotny phase and  $\beta$ -MoSi<sub>2</sub> to the more stable  $\alpha$ -MoSi<sub>2</sub>, as evidenced by a comparison of the 935°C and 1070°C XRD patterns (Figs. 3-10b and 3-10c respectively). Heating to higher temperatures (1400°C, Fig. 3-10d) results in a decrease in the amount of the Nowotny phase and an increase in  $\alpha$ -MoSi<sub>2</sub>. The DTA cooling curves of the binary and the ternary powders were flat in nature, thereby indicating stable structures.

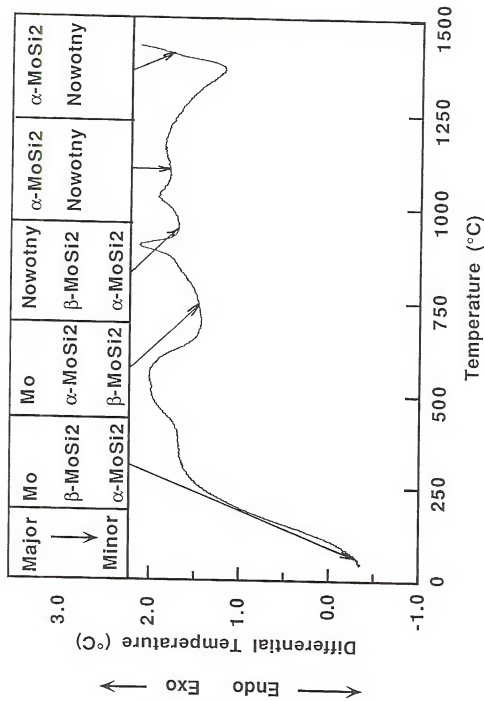


Figure 3-9 DTA of ternary MoSi<sub>2</sub> under flowing argon at a heating rate of 10°C/min. The phase formation sequence is also schematically depicted. ('Nowotny' refers to the Nowotny phase,  $C < [Mo] < 5Si_3$ ).

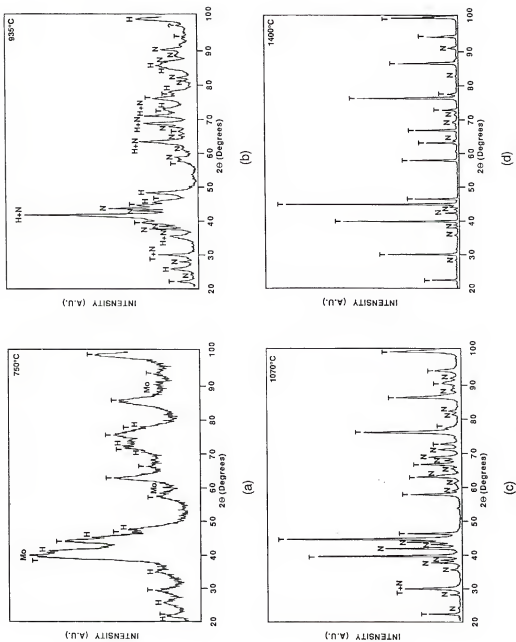


Figure 3-10 XRD of the MA ternary  $\text{MoSi}_2$  powders (Si-28Mo-14C) heated at 10°C/min under flowing argon to the temperatures indicated: (a) 750°C (b) 935°C (c) 1070°C and (d) 1400°C (Mo is molybdenum, Si is silicon, T is  $\alpha\text{-MoSi}_2$ , H is  $\beta\text{-MoSi}_2$  and N is the hexagonal Nowotny phase).



The low temperature formation of the carbon-stabilized Nowotny phase instead of the thermodynamically preferred  $\alpha$ -MoSi<sub>2</sub> phase is probably related to its greater ease of nucleation and growth. The stability of the  $\beta$ -MoSi<sub>2</sub> up to 1030°C is also not surprising. Hexagonal  $\beta$ -MoSi<sub>2</sub> formed as a result of isothermal annealing of sputtered Mo-Si multilayers has been reported to be stable up to 800°C. However, the higher limit of temperature stability of the beta- phase in this study is probably related to the presence of iron and oxygen impurities rather than the relatively high heating rates of the powders in the light of experimental evidence obtained from the isothermal annealing of the MA binary and ternary powders (820°C for a period of 1 h), which demonstrated the stability of  $\beta$ -MoSi<sub>2</sub> under these conditions.

#### 3.4.1.3 Consolidated Microstructures

##### Densities

Bulk density measurements of the various composites prepared during this study show that near full densities (99% or greater) were achieved for the *in-situ* composites and the conventionally processed (CP) composites for compositions up to 40 v/o SiC. Theoretical densities of the *in-situ* composites were estimated based on the volume fraction of SiC experimentally determined through standard point count techniques, while those of the CP composites were based on initial blend stoichiometries. The nearly complete densification of the *in-situ* composites and the absence of gas porosity are significant and indicate the effective removal of product gases of silica deoxidization such as CO and CO<sub>2</sub>.

##### Microstructures

Fig. 3-11 shows the microstructures of a hot pressed specimen derived from the MA binary nominally stoichiometric MoSi<sub>2</sub> powders. Considerable amounts of second phase particles with volume fractions of about 0.15 are present in the MoSi<sub>2</sub> matrix. TEM/EDS analysis of these samples (Fig. 3-12) revealed the presence of submicron-sized grains of MoSi<sub>2</sub> and second phase particles which were amorphous and silicon-rich,

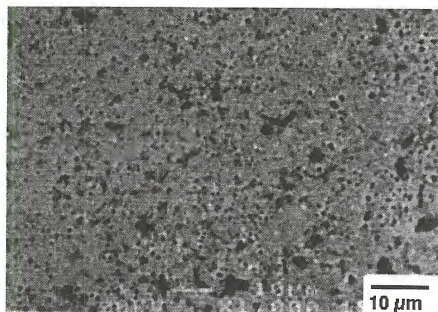


Figure 3-11 Scanning Electron Micrograph (SEM) of the microstructure of the hot-pressed binary MA MoSi<sub>2</sub>.

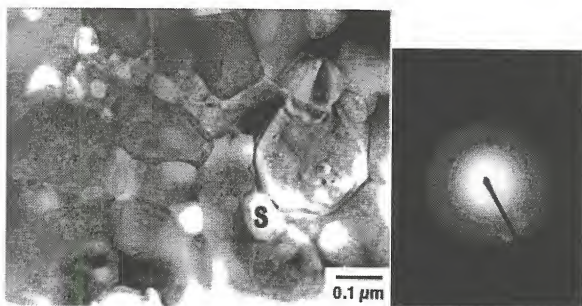


Figure 3-12 Bright Field Transmission Electron Micrograph (BFTEM) and SADP of silica particles in hot-pressed binary MA MoSi<sub>2</sub>. S denotes a typical silica particle.

identifying them as the glassy silica phase. The silica was present primarily at the grain boundaries and triple points. In addition, very fine (10 nm) dispersoids were found within the MoSi<sub>2</sub> grains, along with occasional grains of Mo<sub>5</sub>Si<sub>3</sub>.

Figure 3-13 shows a backscattered electron image of a hot pressed specimen derived from the carbon-modified MA MoSi<sub>2</sub> powder. Considerable improvement in the overall homogeneity and cleanliness of the microstructure is apparent in comparison with the samples derived from the binary MA MoSi<sub>2</sub> powder. Based on the atomic number (Z) contrast, it is apparent that the material has three phases.

Table 3-2 Microstructural characteristics of the consolidated samples derived from the ternary MA MoSi<sub>2</sub> powder

Phase	Compn. (at.%)				Volume Fraction (%)
	Si	Mo	C	Fe	
MoSi <sub>2</sub>	64.55	35.45	0.0	0.0	79.15
SiC	0.0	48.29	50.20	0.0	11.83
Nowotny	54.91	35.26	5.22	4.59	9.028
Overall	58.16	31.7	9.765	0.37	
Initial	58.00	28.00	14.00		

Following qualitative analysis by EDS, the compositions of each of these phases as well as the overall matrix composition were determined by electron microprobe analysis. In addition, quantitative estimation of the volume fraction of these phases was obtained using standard point count techniques. These results are summarized in Table 3-2. The data indicates the presence of SiC (low Z phase), MoSi<sub>2</sub> (intermediate Z phase)

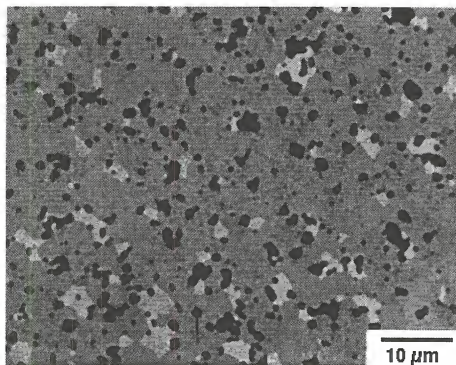
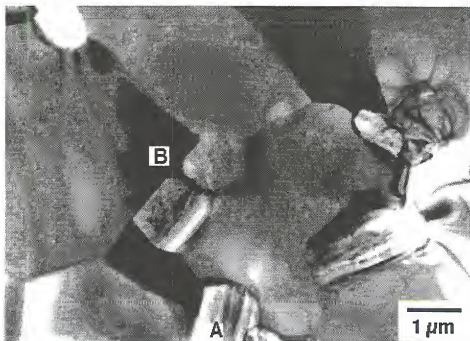


Figure 3-13 Backscattered electron image of the hot-pressed ternary MA MoSi<sub>2</sub> (Si-28Mo-14C) (UF process).

and an iron-containing Nowotny phase  $C_{\leq 1}(Mo,Fe)_{\leq 5}Si_3$  (high Z phase) in the microstructure, and thus seems to support the isotherms proposed by Nowotny and Brewer [Now 54, Bre 56] (see Fig. 2-5a) rather than that of Van Loo [Van 82] (see Fig. 2-5b). Furthermore, the volume fractions of these phases are in reasonable agreement with the location of the nominal compositions in the  $MoSi_2 + SiC + C_{\leq 1}Mo_{\leq 5}Si_3$  three-phase field in the Nowotny diagram.

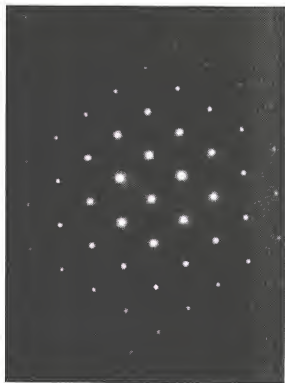
TEM analysis of the carbon-modified material revealed a homogeneous microstructure with uniformly distributed second phases such as those marked A and B in Fig 3-14a. The average grain size of the  $MoSi_2$  was between 3 and 5  $\mu m$ , which is much larger than that of the material without carbon. The larger grain size is a temperature related effect as ternary powder samples consolidated at 1450°C exhibited submicron grain sizes. EDS microanalysis, with ultrathin polymeric window, of region A showed the presence of silicon and carbon alone, indicating that these regions correspond to the dark (low Z) regions such as those shown in Fig. 3-13. Selected area diffraction patterns (SADPs) were obtained along the major zone axes from these and other silicon rich regions (Fig. 3-14b) and were consistently indexed to a cubic  $\beta$ -SiC structure (with  $a = 0.4359$  nm). The  $\beta$ -SiC was present in the form of 1  $\mu m$ -sized particles located predominantly along grain boundaries and at triple point regions. Furthermore, the SiC particles were easily distinguishable based on the internal twinning observed (Fig. 3-15). Although the microstructural origin of these SiC particles is presently not well understood, it is probable that their formation would involve the following reactions: (A) the carbothermal reduction of silica to SiC; and (B) the cooperative displacement of Si and C from  $MoSi_2$  and  $C_{\leq 1}Mo_{\leq 5}Si_3$  to form SiC. While the reaction mechanisms for (A) have been discussed previously, the results of the phase evolution studies on the ternary powders do not indicate the formation of SiC within the limits of detection of the XRD. However, the fact that these studies were conducted on loosely packed powders, at



(a)



(b)



(c)

Figure 3-14 (a) BFTEM of the ternary MA MoSi<sub>2</sub>. (b) SADP of β-SiC along B=[011] (region A). (c) SADP of the Nowotny phase along B=[101̄0] (region B).

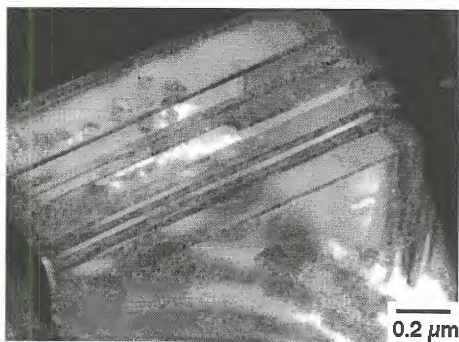


Figure 3-15 BFTEM of a  $\beta$ -SiC particle formed *in-situ* in the ternary MA MoSi<sub>2</sub>.

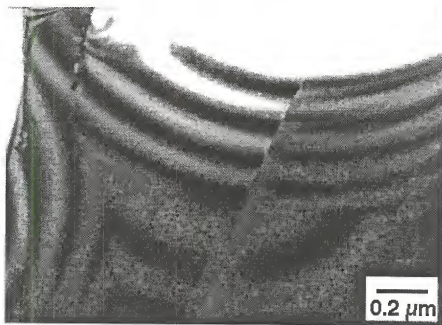


Figure 3-16 BFTEM of the ternary MA MoSi<sub>2</sub> showing the absence of grain boundary SiO<sub>2</sub>.

atmospheric pressures under flowing argon (as opposed to the consolidation conditions which involve densely packed powders under highly reducing atmospheres) might have precluded effective conversion of silica to SiC. On the other hand, direct reaction between cooperatively displaced Si and C is also feasible above 1435°C, based on the DTA data of Singh [Sin 92]. In addition to  $\beta$ -SiC, grains of the iron-containing Nowotny phase (region B) were also easily distinguishable, based on their lower ion milling rates. Most importantly, the grain boundaries also appeared to be free of silica (Fig. 3-16) although a small amount was occasionally observed within the grains. Contrary to Maxwell's hypothesis that molybdenum carbides would be present in the matrix as a reduction product of MoO<sub>3</sub> [Max 52] and in accordance with the 1600°C isotherms of Nowotny, none of the molybdenum carbides such as MoC and Mo<sub>2</sub>C were detected.

#### 3.4.1.4 Contamination Effects due to Milling Media

As mentioned in Section 3.1.4.3, iron was detected in the consolidated microstructures and its origin is believed to be the hardened steel milling media used for the powder attrition process. It was therefore of interest to pinpoint the localization of iron in the microstructure. Accordingly, elemental x-ray mapping of Fe, Mo and C in the microstructure was undertaken and supplemented with backscattered electron imaging of the corresponding location. Evaluation of these maps (Fig. 3-17) reveal that the iron tends to locate preferentially in the high-Z Nowotny phase. These observations, together with the EPMA data, demonstrate the preference of iron to locate in the Nowotny phase. Interestingly, essentially no iron was detected in the MoSi<sub>2</sub> regions despite previous reports that it has a limited amount of solubility for iron [Ray 85]. The preferential location of iron in the Nowotny phase is probably related to the greater affinity of iron towards the carbon centered octahedra of this phase. The relatively small size differences between the atomic radii of Mo and Fe, together with the low levels of the iron impurity make iron substitution on the molybdenum sites easy, since the resulting lattice strains would be small. It is also apparent that the Nowotny phase tends to adjoin the SiC grains



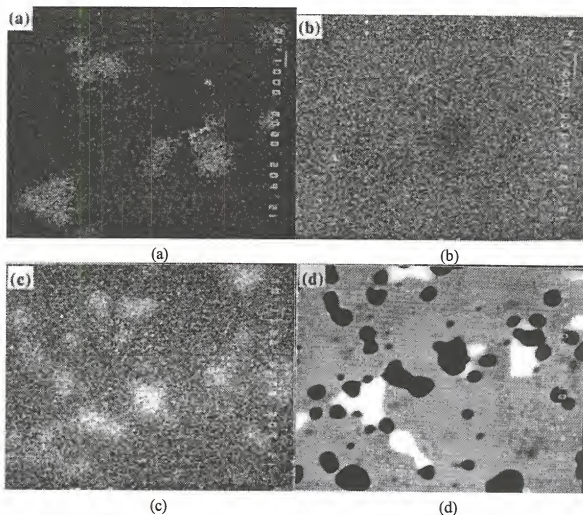


Figure 3-17 X-Ray elemental maps showing location of (a) Fe (b) Si (c) Mo, along with (d) a backscattered electron image of the UF MoSi<sub>2</sub>/SiC. The light phase is the Nowotny phase (note the iron enrichment), the grey phase is MoSi<sub>2</sub>, the dark phase is SiC.

thereby suggesting that its origin is probably due to local deviations from stoichiometry resulting from either  $\text{SiO}_2$  or  $\text{SiC}$  formation.

#### 3.4.1.5 Thermogravimetric Analysis

The results of the thermogravimetric analysis (heating and cooling rates of 10K/min) of the MA binary (solid line) and ternary powders (dotted lines) are shown in Fig. 3-18. The top and the bottom curves in each set represent the weight changes of the powders during heating and cooling respectively. While both the samples experienced weight losses above 1200°C, the C-modified ternary MA  $\text{MoSi}_2$  powders exhibited weight losses that were much higher than those of the binary MA  $\text{MoSi}_2$  at all temperatures. Examination of the XRD patterns of the binary MA  $\text{MoSi}_2$  at temperatures above 1200°C (Fig. 3-8d) revealed minor amounts of tetragonal  $\text{Mo}_5\text{Si}_3$ , indicating a silicon depleted powder. Since the oxygen content of micron-sized  $\text{MoSi}_2$  powders is about 1.5 at. % [Max 52], it is quite possible that the weight losses above 1200°C are caused by the dissociation of  $\text{SiO}_2$  (under very low partial pressures of oxygen) to the volatile  $\text{SiO}$ . On the other hand, the higher weight losses in the C-modified MA  $\text{MoSi}_2$  powders are ascribed to the presence of carbon. However, the mechanism in this case is the reduction of  $\text{SiO}_2$  by carbon to form volatile oxides such as  $\text{CO}$ ,  $\text{CO}_2$ , and  $\text{SiO}$ .

The above data are consistent with the weight losses experienced during the actual hot consolidation of the ternary MA  $\text{MoSi}_2$  samples. Vacuum hot pressing of the C-modified samples at temperatures of 1550°C or less resulted in maximum weight losses of 4.35 %, while higher consolidation temperatures (1700°C) result in a near doubling of the weight losses (8.09 %) However, it should be recognized that the weight losses at temperatures above 1700°C are caused by the volatilization of silicon from  $\text{MoSi}_2$  due to the relatively high vapor pressures of silicon over  $\text{MoSi}_2$  [Cha 74, Sea 60], rather than by the carbothermal reduction of the  $\text{SiO}_2$ . This implies that while relatively minor weight losses (up to 5 %) due to carbothermal reduction of silica are unavoidable, careful control

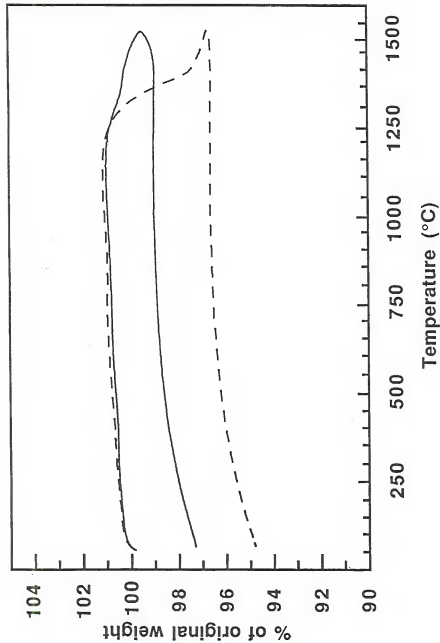


Figure 3-18 TGA of the binary stoichiometric MA MoSi<sub>2</sub> (—) and ternary MA MoSi<sub>2</sub> (Si-28Mo-14C) (---) under flowing argon at a heating and cooling rate of 10°C/min. The top curve in each set represents heating while the bottom curve represents cooling.

of the consolidation temperature and vacuum levels can prevent substantial weight losses (~40%) such as those reported in previous studies [8].

### 3.4.2 Microstructural Comparisons: *In-situ* vs. Conventionally Processed MoSi<sub>2</sub>/SiC

#### 3.4.2.1 *In-situ* Processed (UF) Composites

Figure 3-19a shows a backscattered electron image of the hot pressed specimen MA20. The microstructure consists of a uniform distribution of 1-2  $\mu\text{m}$  sized low Z particles dispersed in an intermediate-Z matrix. XRD and EDS analysis together indicated the low Z phase to be SiC, while the intermediate Z phase was MoSi<sub>2</sub>. In addition, minor amounts (< 1v/o) of the high Z Nowotny phase were observed. In expected agreement with the processing rationale adopted, the relative volume fractions of these phases were found to agree very well with the location of the nominal powder compositions in the 1600°C Mo-Si-C isotherm of Nowotny. The grain size of the MoSi<sub>2</sub> was relatively uniform and between 6-8  $\mu\text{m}$ . Polarized light microscopy indicated that the SiC particles were located primarily at the grain boundaries. Occasionally, large SiC grains were also observed. Previous TEM analysis of similarly processed material, as shown in the previous sections, revealed the grain boundaries to be free of siliceous intergranular phases.

The microstructure of the hot-pressed UF40 alloy (Fig. 3-19b) (interchangeably designated MA40) shows a dispersion of SiC in the MoSi<sub>2</sub> matrix. However, the SiC size is considerably larger and the distribution considerably more inhomogeneous than the MA20 (UF20) material. This is attributed to diffusion-controlled coarsening of SiC brought about by the smaller interparticle spacing associated with the high volume fractions of SiC. Indeed, the presence of necks between adjacent SiC particles (e.g. Fig 3-19b) is indicative of coarsening by coalescence. This coarsening leads to a wider size distribution and a higher mean particle size, and consequently to a wide variation in the MoSi<sub>2</sub> grain size distribution due to varying Zener drag on the grain boundaries. The

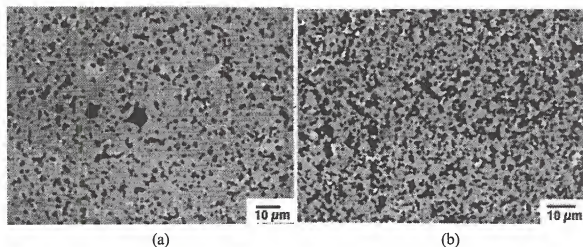


Figure 3-19 Backscattered electron images of consolidated microstructures of UF MoSi<sub>2</sub>/SiC containing (a) 20 v/o and (b) 40 v/o SiC. The dark and grey phases are SiC and MoSi<sub>2</sub> respectively.

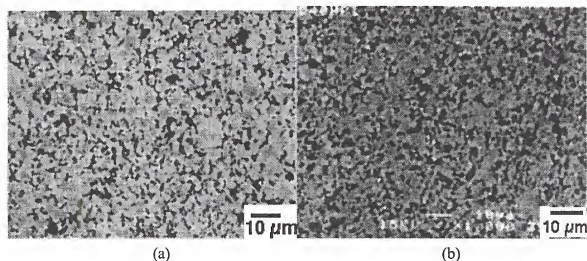


Figure 3-20 Backscattered electron images of consolidated microstructures of CP MoSi<sub>2</sub>/SiC containing (a) 20 v/o and (b) 40 v/o SiC. The dark and grey phases are SiC and MoSi<sub>2</sub> respectively.

MoSi<sub>2</sub> grain size varies between 2 and 7  $\mu\text{m}$ , with the mean grain size close to 5  $\mu\text{m}$ . The SiC is irregularly shaped, with a size range from 1 - 10  $\mu\text{m}$ .

#### 3.4.2.2 Conventionally Processed (CP) Composites

The microstructures of the conventionally-processed (CP) composites CP20 and CP40 are shown in Figs. 3-20a and 3-20b respectively and are typified by an inhomogeneous distribution of the SiC particles. These microstructures are characterized by particle-free islands of MoSi<sub>2</sub> surrounded by a network of irregularly shaped SiC particles. The rather inhomogeneous distribution is attributed to variations in starting powder sizes of the MoSi<sub>2</sub> and SiC. The size of the SiC is much greater than the initial starting size of less than 1  $\mu\text{m}$ , indicative of its coarsening during consolidation. Both of these microstructures are exemplified by a wide distribution of matrix and reinforcement grain sizes. The CP20 composite has a MoSi<sub>2</sub> grain size range ranging from 2 - 10  $\mu\text{m}$ , with a mean of 7  $\mu\text{m}$ , while for the CP40 composite, these values range from 2 - 8  $\mu\text{m}$ , with a mean of around 5  $\mu\text{m}$ . These wide distributions in the matrix and reinforcement grain sizes are significant, since they may enhance the magnitude of the thermal mismatch stresses between the two phases.

#### 3.4.3 Oxygen and Carbon Analysis

Since the elimination and control of the oxygen was one of the main premises of this investigation, it is instructive to look at the oxygen levels at various stages of the process. It should be noted that a minimum amount of carbon is necessary for the complete deoxidization of the matrix.

The oxygen contents of the powders are reported in Table 3-3. In general, the data reveal the powder size dependence of the oxygen contents. For example, commercially available -325 mesh MoSi<sub>2</sub> powder possesses about 2.02 w/o oxygen, while mechanically alloyed MoSi<sub>2</sub> powders, with their submicron size distribution, typically have double

Table 3-3 Carbon and Oxygen Analysis of the Starting Powders

Powder Source	Size	C (w/o)	O (w/o)
Cerac	-200, +325 mesh	0.0449 <sup>a</sup>	0.300
Johnson Matthey	-325 mesh	0.175±0.001 <sup>a</sup>	2.02±0.04
Maxwell's powder <sup>b</sup>	100% < 6 μm	0.08 <sup>a</sup>	1.5
(sintering studies)	98% < 1 μm		
Maxwell's powder <sup>c</sup>	< 6 μm	0.13 <sup>a</sup>	0.35
(hot pressing study)			
UF (Mechanically	< 1 μm	variable <sup>d</sup>	4.07± 0.016
Alloyed) MA20B		3.8	

<sup>a</sup> Originally present in powder; no addition

<sup>b</sup> Lot 15, per his designation

<sup>c</sup> Commercially acquired and ground (Maxwell)

<sup>d</sup> Intentional additions, dependent on target compositions.

Table 3-4 Oxygen Analysis of the Consolidated Microstructures

Material	Carbon (w/o)	Oxygen (w/o)	Processing Technique
UF MoSi <sub>2</sub> -20v/o SiC (UF20A-HP4)	2.38 ± 0.01	0.39 ± 0.03	Ambient handling <i>in-situ</i> deoxidization
UF MoSi <sub>2</sub> -20v/o SiC (UF20A-HP5)	2.26	0.26 ± 0.02	Ambient handling <i>in-situ</i> deoxidization
UF MoSi <sub>2</sub> -20v/o SiC (UF20B-HP1)	2.22 ± 0.03	0.542 ± 0.14	Ambient powder handling <i>in-situ</i> deoxidization
UF MoSi <sub>2</sub> -5v/o SiC	0.821	0.167	Ambient powder handling <i>in-situ</i> deoxidization
CP MoSi <sub>2</sub> -20v/o SiC (C20-HP4)	3.573 ± 0.06	1.61 ± 0.05	conventional blend and hot consolidate
CP MoSi <sub>2</sub> -20v/o SiC (C20-HP5)	3.77	1.71 ± 0.05	conventional blend and hot consolidate
Sintered Bar, no C (Maxwell)		1.4	sintering
Sintered Bar, with 1.7 w/o C addition (Maxwell)		0.15	sintering
Hot Pressed Bar (Maxwell)		0.42	
Rockwell MoSi <sub>2</sub> (controlled atm)		0.16-0.22	Reactive HIP + Glovebox Processing
LANL MoSi <sub>2</sub>		0.1	Glovebox Processing MA + vacuum Hot press



this amount. As a result, significant reductions in starting powder oxygen contents are achieved in the larger sized powders, as evidenced by the 0.3 w/o oxygen for the -200, +325 mesh Cerac powders.

Thus, the data indirectly illustrate the surface origins of the oxygen content. Furthermore, finer powders would be expected to possess more surface oxygen, and consequently would require more carbon for carbon deoxidization. Sintering studies of Maxwell on fine powders of size distribution less than 1  $\mu\text{m}$  suggested a carbon requirement for complete deoxidization of between 1 and 4 w/o [Max 52b]. Along with lowered oxygen levels due to deoxidization, sintering also leads to carbon losses from the body.

The oxygen and carbon contents of the consolidated microstructures are shown in Table 3-4. Considering the CP20 composites and comparing the oxygen contents of the starting Johnson Matthey powder and the consolidated microstructure, we note a reduction in the oxygen levels from 2.02 to 1.61 w/o, presumably due to the reducing atmospheres surrounding the graphite die, plus the deoxidizing effect of tramp carbon present in the starting powder (0.175 w/o). Additional increases in carbon content of the samples due to pickup and diffusion of carbon from the die walls into the compact also cannot be ruled out. With respect to the UF material, and referring again to Tables 3-3 and 3-4, in spite of the high oxygen levels ( $\sim 4$  w/o) of the starting powders, significant reductions in the oxygen content are achieved and the final microstructures possess oxygen levels comparable to those achieved using sophisticated powder handling techniques. The data thus demonstrate the efficacy of the *in-situ* deoxidization reactions, and corroborate the microstructural evidence obtained through TEM. Some degree of scatter is evident on the lowest oxygen levels obtainable through the UF process, with levels of between 0.167 and 0.39 w/o. The lowest oxygen levels of 0.167 w/o for the UF  $\text{MoSi}_2$ -5 v/o SiC are in the same range as those of the Rockwell and LANL-processed material, which were obtained by conducting the entire powder handling under controlled

atmospheres. The latter result is significant, since the UF process does not require special care for powder handling or consolidation, to obtain similar levels of oxygen. Within the same batch of mechanically alloyed powders, some degree of scatter is also evident on comparing the oxygen contents of composites obtained from different hot pressing runs. Significant reduction in the carbon levels is also apparent as a result of the deoxidization reactions.

Theoretical calculations based on the assumption that all the oxygen is present as silica reveal that every w/o of oxygen results in the incorporation of 4.7 v/o silica in the matrix. Furthermore, calculations based on the reaction stoichiometry of the carbothermal reduction reaction indicate that for every cubic centimeter of  $\text{SiO}_2$  reduced results in the incorporation of 0.48 cubic centimeter of SiC, assuming the density of silica and SiC to be 2.32 and 3.22 respectively. Based on these, it is estimated that a minimum of between 2 to 4 v/o SiC will be formed in the  $\text{MoSi}_2$  matrices as a result of matrix deoxidation.

### 3.5. Significance of the *In-situ* Reactions

The preceeding sections have illustrated the rationale and the modus operandi of the use of *in-situ* reactions in the processing of  $\text{MoSi}_2$  matrix composites. As a specific example, it has been shown that a judicious combination of *in-situ* techniques with carbothermal reduction reactions and mechanical alloying result in the production of thermodynamically stable, chemically and microstructurally homogeneous microstructures free of potentially deleterious phases, through the use of single step reactions. For the Mo-Si-C system, the ability to tailor such aspects of the microstructure as the grain size and the second phase volume fraction through control of the starting compositions has been demonstrated. A powerful argument for the utility of this process stems from the fact that such microstructural variations are achieved, without affecting the skeletal elements of the basic process. The interlink between the starting compositions and the final grain size has been elucidated, through the analysis of the

second phase volume fractions. It appears attractive to extend this type of analysis to two phase systems involving line compounds, regardless of the processing routes used. This is significant, considering that the list contains technologically important borides, silicides, nitrides, oxides, carbides, etc., which have a plethora of applications far-removed from the mechanical property requirements envisaged in this investigation.

Close stoichiometric control is yet another advantageous aspect of the process which has been demonstrated herein. Again, this represents a significant advancement in the processing of line compounds.

The ability to form silica-free MoSi<sub>2</sub> based composites containing micron-sized SiC reinforcements opens up some exciting possibilities from a mechanical properties perspective also. Strengthening theories would suggest that uniformly dispersed SiC in a modified MoSi<sub>2</sub> matrix should lead to considerable elevated temperature strengthening, in addition to improved fracture properties, due to the enhanced resistance to grain boundary sliding brought about by the SiC dispersoids in the absence of a viscous silica film. It is also conceivable that synthesis of MoSi<sub>2</sub>/WSi<sub>2</sub> alloys with carbon additions by means of mechanical alloying may result in improved strengthening due to the synergistic effects of solid solution and dispersion strengthening with *in-situ* formed SiC or WC.

Utilization of this strategy holds promise in ductile phase toughening also. For instance, while compositing with refractory metals such as niobium, tantalum, and tungsten seems to be one of the favored means for increasing the room temperature toughness of this brittle intermetallic, the major problems encountered are the degradation of the diffusion barrier coatings due to their reaction with silica, and the severe residual stresses caused by the mismatch in the coefficients of thermal expansion (CTE) between the matrix and the reinforcement leading to cracking of the matrix. Through the use of the ternary MA MoSi<sub>2</sub> powders, it should be possible to form the desired volume fraction of SiC reinforcements *in-situ* so as to tailor the effective CTE of the matrix to match that of the reinforcement. For example, the CTE of a refractory metal such as molybdenum or

tungsten is intermediate between that of  $\text{MoSi}_2$  and  $\text{SiC}$ . As has been shown by Maloney et al. [Mal 92], controlled additions of micron-sized  $\text{SiC}$  lower the effective CTE of the  $\text{MoSi}_2$ - $\text{SiC}$  composite in accordance with the rule of mixtures and enable the use of refractory metals that have better strength retention at elevated temperatures (i.e. W), but are otherwise limited in their use due to their low CTEs. Such an *in-situ* modified matrix would also have the added advantage of being free of silica and silicon, compared to composites processed using commercial powders; this should prevent the coating degradation and enhance the useful life of these composites.

### 3.6 Summary and Conclusion

$\text{MoSi}_2/\text{SiC}$  composites containing up to 40 v/o  $\text{SiC}$  have been fabricated using a novel processing technique involving mechanical alloying, carbothermal reduction of silica and *in-situ* displacement reactions, starting from elemental molybdenum, silicon and carbon powders. Grain boundary silica, otherwise present in conventional powder processed  $\text{MoSi}_2$  matrix composites has been eliminated through this technique. Homogeneous distribution of the reinforcing phase is observed for  $\text{SiC}$  contents up to 20 v/o, while higher loadings lead to inhomogeneities brought about by the diffusion-controlled coarsening of the  $\text{SiC}$  due to reduced interparticle distances.

The structural and morphological evolution of the powders with and without carbon additions has been studied as a function of milling time. Complete attrition is achieved after 29 hours of alloying. The resultant powders are micron-sized and contain 4 to 7 nm crystallites of molybdenum,  $\alpha$ - $\text{MoSi}_2$  and traces of  $\beta$ - $\text{MoSi}_2$ . Carbon additions to the starting elemental powder mixture suppress the formation of  $\alpha$ - $\text{MoSi}_2$  in the fully milled powders. Minor amounts of iron impurities were also found in the powders due to the contamination from the milling media.

The phase evolution studies of the binary and ternary  $\text{MoSi}_2$  powders indicated that  $\beta$ - $\text{MoSi}_2$  is stable to  $1020^\circ\text{C}$  at heating rates of  $10^\circ\text{C}/\text{min}$ , in contrast to previous

studies on the isothermal annealing of Mo-Si multilayers which demonstrated stabilities to only 800°C. While minor amounts of tetragonal  $\text{Mo}_5\text{Si}_3$  were evolved as an intermediate transformation product in the binary MA  $\text{MoSi}_2$  powders, the evolution of the ternary  $\text{MoSi}_2$  powders showed the formation kinetics of the Nowotny phase  $\text{C}_{\leq 1}\text{Mo}_{\leq 5}\text{Si}_3$  to dominate that of tetragonal  $\alpha\text{-MoSi}_2$  at lower temperatures. However, temperatures above 1000°C resulted in the progressive decrease in the amount of these higher molybdenum phases.

Complete consolidation of the MA powders was achieved at temperatures from 1450°C onward. Amorphous silica found in all conventional powder processed matrices was eliminated through *in-situ* carbothermal reactions facilitated by the carbon additions through mechanical alloying. It is shown that composites consisting of uniformly distributed micron-sized SiC particles with varying volume fractions can be formed using this approach. Significant grain size differences exist between the microstructures processed from the binary powders and those of the ternary powders, probably due to the higher consolidation temperatures used in the case of the latter. The formation of the iron and molybdenum containing Nowotny phase of the approximate composition  $\text{C}_{<0.5}\text{Mo}_{<4.4}\text{Fe}_{0.4}\text{Si}_3$  is also reported. The co-existence of the Nowotny phase with  $\text{MoSi}_2$  and SiC is in agreement with the isotherm proposed by Nowotny et al. rather than that proposed by Van Loo and coworkers.

The possibilities of utilizing MA powders to overcome the CTE mismatch and coating degradation problems in ductile phase composites are discussed. Use of these compositionally tailored powders would alter the matrix CTE so as to match that of the ductile reinforcements, thus minimizing the problems of matrix cracking. The absence of silica should also improve the diffusion barrier coatings of these composites.

## CHAPTER 4 MECHANICAL PROPERTIES

### 4.1 Introduction

The key issues of particular relevance to the potential commercial realization of MoSi<sub>2</sub> are its ambient toughness, high temperature creep strength and fabricability. Like most intermetallics and ceramics which have complex low-symmetric crystal structures with large unit cells and directional bonding, MoSi<sub>2</sub> is brittle at room temperature up through ~ 1200°C. Likewise, it suffers drastic strength reductions at temperatures past 1200°C, the very temperature range for which it is under consideration. Net-shape forming of MoSi<sub>2</sub> and MoSi<sub>2</sub>-based composites also poses significant challenges due to its hard and brittle nature, which results in poor machinability. Thus, room temperature shape-forming of the silicide has been confined to grinding and polishing operations, which are not cost-effective.

In this chapter, we have endeavored to address at least two of the three key issues, namely, improving the high temperature strength and developing a methodology for the near-net shape manufacture of MoSi<sub>2</sub> based materials. To achieve this, systematic flow characterization studies have been carried out from 1180°C to 1450°C, as a function of key microstructural parameters such as the grain size and the intergranular silica content. The effects of silica are elucidated by comparing the deformation behavior of two classes of MoSi<sub>2</sub>/20 v/o SiC composites processed using the CP and UF routes: both have similar grain size distributions, but, as shown in Table 4-1, differ chiefly in their oxygen levels (and hence the amount of intergranular silica). Of particular interest is the

extent to which the non-wetting silica phase affects the high temperature flow properties. Similarly, the effects of grain size are elucidated by comparing the properties of silica-free MoSi<sub>2</sub>/SiC materials containing 20 and 5 v/o SiC which have different grain sizes.

Table 4-1 Oxygen analysis of the consolidated microstructures

Material	Oxygen (w/o)	Processing Technique
UF MoSi <sub>2</sub> /20 v/o SiC	0.241	Mech. Alloyed
CP MoSi <sub>2</sub> /20 v/o SiC	1.72	Blend + Consolidate

Fracture toughness measurements are also presented to elucidate the effects of intergranular silica. Finally, the implications of these results are discussed, with special emphasis on resolving the formability and high temperature strength issues in MoSi<sub>2</sub>.

## 4.2 Experimental

### 4.2.1 Hardness and Fracture Toughness Measurements

Hardness and fracture toughness measurements were carried out on UF and CP MoSi<sub>2</sub>/SiC with 20 and 40 v/o SiC. Vickers microhardness indentations, each at least 3 mm apart (to minimize interactions between neighboring cracks) were made on the surfaces of the samples polished to a 1  $\mu$ m diamond finish. The indentation loads spanned a range from 49 N to 245 N for a contact time of 15 seconds, with a minimum of 4 indentations per indent load per sample. The minimum indentation loads were selected so as to achieve a minimum value of 2 for the ratio of the half penny crack radius ( $c$ ) and half the diagonal of the Vickers impression, a requirement recommended in conventional practice for toughness measurements by indentation. In the case of the monolithic

MoSi<sub>2</sub>, extensive microcracking around the indenter prevented the formation of well defined cracks for loads up to 196 N, in part due to the large grain size. The lengths of the indent diagonals (2a) and the radial cracks (2c) were measured and the hardness (H) and fracture toughness (K<sub>IC</sub>) were calculated using the following equations [Ans 81]:

$$H = P / \alpha a^2 \quad (4.1)$$

and

$$K_{IC} = \delta (E/H)^{1/2} (P/c)^{3/2} \quad (4.2)$$

where P is the peak indentation load,  $\alpha = 2$  for a Vickers indenter,  $\delta$  is a material independent constant ( $\delta = 0.016$ ) and E is the Young's modulus. The Young's moduli of the composites were calculated using values derived from literature for MoSi<sub>2</sub> [Nak 90] and SiC [Eng 79] and assuming the rule of mixtures behavior (Voight bound).

#### 4.2.2 Flow Characterization

As detailed in the Introduction, two classes of MoSi<sub>2</sub>/SiC composites containing 20 v/o SiC reinforcements were investigated. The first class of materials (hereafter designated UF MoSi<sub>2</sub>/ 20 SiC) was prepared using a combination of mechanical alloying and *in-situ* carbothermal reduction reactions starting from elemental molybdenum (3-7  $\mu$ m, Johnson Matthey), silicon (98% pure -325 mesh, Cerac), and carbon (99.5% pure, -300 mesh, Johnson Matthey) powders. Details of the processing scheme are outlined in the preceding chapter. For purposes of comparison, composites with 20 vol. % reinforcement were fabricated using the conventional approach of dry blending MoSi<sub>2</sub> (99.9% pure, -325 mesh, Johnson Matthey) and SiC powders (<1  $\mu$ m average diameter, 99.9% pure, Cerac) in the appropriate proportions, followed by hot consolidation. The matrix grain size, reinforcement size and volume fraction were kept reasonably constant between the UF and CP materials in order to facilitate meaningful comparisons.



In order to study the effects of grain size on flow properties, silica-free MoSi<sub>2</sub>/SiC composites containing 5 v/o SiC reinforcement, and a median grain size of 40 µm were also scrutinized for systematic mechanical property measurements.

#### 4.2.2.1 Specimen Preparation and Testing

##### Compression Testing

Following hot consolidation, rectangular parallelepiped compression specimens of nominal dimensions 4 mm x 4 mm x 7.5 mm ( aspect ratio ~ 1.75) were electro-discharge machined from the billets. The orientation of the samples was such that the testing direction was perpendicular to the hot consolidation direction. The specimen ends (in subsequent contact with the compression platens during testing) were polished flat and parallel to each other, as well as being perpendicular to the compression axis.

High temperature compression tests were performed on an MTS closed-loop servo hydraulic test (Model 810) machine equipped with a Centorr furnace. Specimens were tested under constant displacement using graphite loading rams, SiC platens and grafoil / boron nitride lubricants between the sample and the platens. Testing was conducted in a titanium-gettered argon atmosphere at temperatures from 1180°C to 1360°C. To ensure minimal oxygen levels in the furnace while testing, the furnace assembly was subjected to a chamber evacuate - backfill cycle for a minimum of four times. Heating of the specimen to temperature was accomplished with the aid of an OXY-GON model FR200 furnace attached to the load frame of the MTS system, with tungsten mesh elements surrounding the samples. The furnace was instrumented with two thermocouples placed 10 mm from the sample surface. The testing temperatures chosen were below the initial consolidation temperature; this ensured stable microstructures during testing. The furnace temperature was held to within  $\pm 3^\circ\text{C}$  during the entire duration of the tests. The control console allowed for both manual and automatic operation of the furnace, whereby heating from room temperature to 200°C was performed manually in 20 minutes, followed by a pre-programmed ramp up to the

test temperature in 45 minutes. Shorter ramp times were avoided, based on prior experience of furnace instabilities (temperature fluctuations) when quicker ramp-up cycles were adopted. While initial specimen setup and testing were usually performed under stroke control (subsequent to the backfill operation), heating was inevitably done under load control in order to compensate for the load train expansion during heatup. For this purpose, loads of between 10 - 15 lbs were found to be adequate. This load, while ensuring the stability of the specimen against sliding, however was insignificant to contribute to the overall specimen deformation. Subsequent to reaching the test temperature, this load was released and the instrumentation zeroed. A sufficient amount of time (at least 30 minutes) was allowed for equilibration of the specimen and the load train before the commencement of the tests.

The compliance of the system, including the graphite rams and the SiC platens was measured over the range of test temperatures for incorporation into the load-displacement data. Displacement measurements were indirectly monitored through measurements of the position of the cross head during testing; the small size of the test specimens and the furnace geometry precluded conventional methods of specimen extensometry, necessitating such specimen displacement calculations from the crosshead motion. The load displacement records were acquired digitally with appropriate data acquisition tools (LabTech Notebook), as well as through an analog recorder (Hewlett Packard Model), with buffering capabilities. From these, true stress and true strain values were calculated, invoking the assumptions of specimen volume conservation and uniform deformation.

Deformation behavior was characterized using a combination of constant strain rate and strain rate change (SRC) testing, with the latter being used to determine the value of the strain rate sensitivity exponent. Some constant load creep tests were also performed. In most cases, steady-state deformation (i.e. flow under constant stress) was attained with strains of the order of a few percent; this facilitated the performance of

strain rate change testing. For each strain rate, the flow stress was determined after steady state deformation was maintained for at least 3% strain. Tests were typically performed for sample strains of up to 30%, with strain rates ranging from  $2 \times 10^{-6} \text{ s}^{-1}$  to  $2 \times 10^{-3} \text{ s}^{-1}$ . The lower strain rate limits for each material were determined by the limit of load resolution of the testing set-up, which corresponded to 6 MPa stress level for the specimen geometries investigated herein. The strain rate sensitivity index ( $m$ ) was derived from the slopes of the  $\log \sigma - \log \dot{\epsilon}$  plots; cubic curve fits to the data followed by calculation of the first derivative sufficed for these purposes [Pad 80, Edi 76]. Microstructural characterization of the as hot-pressed and compression tested materials was conducted on selected specimens using optical and scanning electron microscopy.

#### Bend Strength Measurements

Flexure strength measurements were conducted on four-point bend bar specimens having nominal dimensions of 4 x 3 x 25 mm which were electro-discharge machined from the billets. Prior to testing, the edges of the test bars were chamfered and polished to 1  $\mu\text{m}$  diamond finish. Testing was performed using SiC fixtures, with an inner span of 10 mm and an outer span of 20 mm. These tests spanned the temperature range from 1200°C to 1450°C. All tests were conducted at a constant crosshead speed of 50.8  $\mu\text{m} / \text{minute}$  under flowing argon.

#### 4.2.2.2 Data Analysis

Since the experiments were conducted at a constant displacement rate rather than a constant strain rate, and since relatively large deformations were involved, special corrections were used to analyze the data, as noted below:

Denoting the typical load by  $P$ , and displacement (compensated for machine compliance) by  $\Delta l$ , we invoke the logarithmic definition of strain to calculate the true strain,  $\epsilon$  as,

$$\epsilon = \int_{l_0}^l \frac{dl}{l} = \ln \frac{l}{l_0}$$

Thus,

$$\epsilon(t) = \epsilon(t) = \ln \frac{l(t)}{l_0}$$

The initial true strain rate is defined as

$$\dot{\epsilon}_0 = \frac{\dot{l}}{l_0}$$

where the crosshead displacement rate is given by  $\dot{l}$ . From this, the instantaneous strain rate is computed from the cross head speed using the relation,

$$\dot{\epsilon}(t) = \frac{\dot{l}}{l_0} \cdot \frac{1}{1+e}$$

The engineering strain is given by

$$e = \frac{l - l_0}{l_0} = \frac{l}{l_0} - 1$$

It is noted here that  $e$  is positive in tension and negative in compression. The true strain rate, is then given by

$$\begin{aligned} \frac{d\epsilon(l)}{dt} &= \frac{1}{1+e} \frac{de}{dt} \\ &= \frac{1}{1+e} \frac{de}{dl} \frac{dl}{dt} \\ &= \frac{1}{1+e} \cdot \frac{1}{l_0} \cdot \dot{l} \end{aligned}$$

We thus obtain

$$\dot{\epsilon}(t) = \dot{\epsilon}_0 \cdot \frac{1}{1+e}$$

Likewise, the true stress is calculated from

$$\sigma = S(1+e)$$

where the engineering stress,  $S$ , is given by

$$S = P/A$$

is the engineering stress.

A note of caution is required in the interpretation of the flow stress data generated here. In calculating the flow stress, friction-free sliding between the specimen and the silicon carbide platens was assumed. Friction was neglected since the specimens showed very little barreling after deformation. Finite friction would imply that the actual flow stress would be lower than the values reported in this document.

The stress exponent  $n$  (and hence the strain rate sensitivity,  $m$ ) was determined as the slope of the experimentally determined  $\ln \sigma - \ln \dot{\epsilon}$  plots. The latter were obtained using the values measured in the steady state region. The data are subjected to a polynomial curve fit, and the resultant equation differentiated and numerically evaluated at specific values of  $\dot{\epsilon}$  to yield the  $n$  and SRS ( $m$ ) values. This method of evaluation has been successfully used for a variety of materials in the past [Dun 72; Ald 67; Pad 80; Ari 76].

The activation energies for flow were determined in region II of the stress-strain rate diagram, corresponding to the maximum in SRS. For the fine-grain sized UF and CP MoSi<sub>2</sub>/20 SiC material, identical stress levels corresponding to 60 MPa were chosen, and the strain rates were determined at each temperature from the stress- strain rate plots. The plot of the strain rates versus the inverse temperature thus obtained gave a measure of the activation energy. Considerable care was exercised in choosing the stress levels so as to ensure that the strain rate variations were in the same deformation regime (similar  $n$  or  $m$  values) over the range of temperatures in which the activation energies were determined.

### 4.3 Results and Discussion

#### 4.3.1 Microstructure

Figures 4-1a and 4-1b are optical micrographs obtained from the as hot pressed composites of the *in-situ* UF and CP 20 v/ SiC composites. The matrix grain size is relatively uniform and between 6-8  $\mu\text{m}$ . The SiC particles are uniformly distributed, with a size of 1-2  $\mu\text{m}$ . The SiC particles (typically 2 to 3  $\mu\text{m}$ ) were located predominantly along the grain boundaries. Occasionally, large SiC grains were also observed. Prior TEM analysis of the UF MoSi<sub>2</sub>/ 20 SiC material (Chapter 3) showed grain boundaries which were free of the siliceous intergranular phase. In the case of the CP material (Fig. 4-1b), the microstructure was less homogeneous and consisted of particle-free islands of MoSi<sub>2</sub> surrounded by SiC particles. In this case, however, the microstructures were somewhat in homogeneous due to the relative size distributions of the starting MoSi<sub>2</sub> and SiC powders. The matrix grain size in this material was nearly the same ( $\sim 7 \mu\text{m}$ ) as the *in-situ* processed material; so was the reinforcement size and volume fraction. Again, prior TEM analysis reveals the presence of  $\sim 6$  v/o silica particles which existed as discrete pockets along triple junctions. Oxygen analysis of the as-consolidated materials (Table 4-1) confirmed the difference in oxygen (and hence silica) levels between the CP and UF materials with oxygen contents of 1.72 and 0.24 w/o respectively.

#### 4.3.2 Hardness and Fracture Toughness

Figure 4-2 shows the variation of the Vickers hardness as a function of reinforcement content of the composites. For the purpose of comparison, the hardness of the composites as predicted by a simple rule of mixtures is also plotted in the figure. It should be noted that while the hardness values of single phase MoSi<sub>2</sub> ( $\sim 20 \mu\text{m}$  grain size)

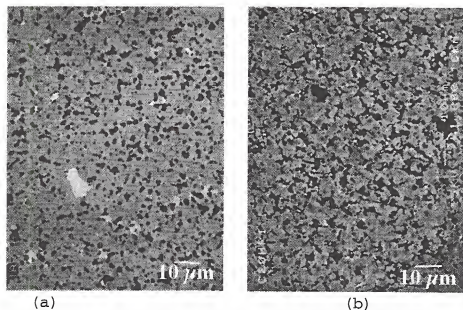


Figure 4-1 SEM of the undeformed (a) UF MoSi<sub>2</sub>/20SiC (b) CP MoSi<sub>2</sub>/20SiC

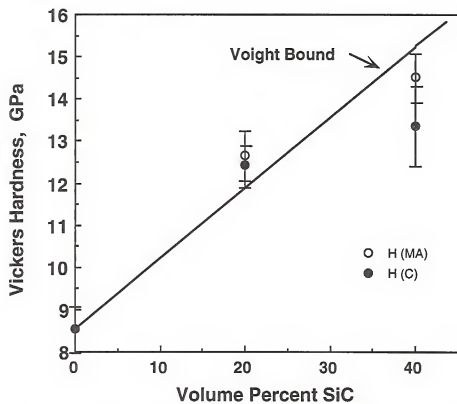


Figure 4-2

Vickers hardness of the CP and UF MoSi<sub>2</sub>/ SiC composites. H(MA) refers to the hardness of the mechanically alloyed UF material, while C refers to that of the conventionally processed material.



studied in this investigation is  $8.56 \pm 0.5$  GPa, a slightly higher value was used in the rule of mixtures calculation in order to account for the smaller grain size of the matrix in the composites ( $\sim 10$   $\mu\text{m}$  or less). Previous studies on monolithic  $\text{MoSi}_2$  have shown the hardness to increase slightly with decreasing grain size [Wad 92]. The hardness value of SiC used in the rule of mixtures estimation was 25 GPa [Ohy 92].

The results show that the room temperature hardnesses of the  $\text{MoSi}_2/\text{SiC}$  composites increase with increasing SiC content. For all reinforcement contents, the hardnesses of the *in-situ* composites were slightly higher than the CP composites, with the difference increasing with increasing reinforcement content. Microstructural comparison between the CP and *in-situ* processed composites at 40 v/o SiC loading show no marked differences in the matrix or reinforcement grain sizes or in their spatial distribution to account for the observed differences. However, it may be of significance that the content of the intergranular silica phase in these composites are substantially different, with the MA material containing little or no silica. Specifically, the presence of the viscous glass phase at elevated temperatures might play a significant role in the relaxation of the thermal contraction stresses generated during cooldown by the CTE mismatch between the reinforcement and matrix phases.

Figures. 4-3a and 4-3b shows the variation of the fracture toughness with SiC content for the *in-situ* processed and CP composites respectively for various indentation loads, with each data point representing the average of at least 4 indentations. It is seen that the fracture toughness of the *in-situ* composites increases monotonically with reinforcement content upto 40 v/o. In contrast, the CP composites exhibit a much slower increase in toughnesses with SiC loading for SiC content above 20 v/o. This increase in toughness with increasing reinforcement content for the conventionally processed material is consistent with earlier data [Bha 91]. Furthermore, the peak toughness values obtained in the composites processed using the CP as well as the MA approaches are almost

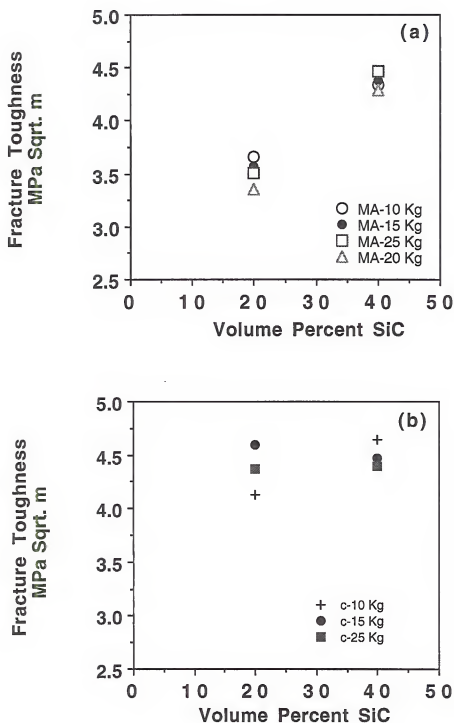


Figure 4-3 Indentation fracture toughnesses of (a) UF and (b) CP MoSi<sub>2</sub>/SiC. The MA and C designations refer to the mechanically alloyed UF material and conventionally processed material respectively, while the indent loads are indicated by means of the numbers that follow the alphabets.

identical at around 4.5 MPa.  $m^{1/2}$ . This is perhaps the limit of toughening for SiC particulate reinforced MoSi<sub>2</sub>.

The fracture toughness data also indicates that the toughnesses are constant and do not show any variations with the crack length, at least for the range of indentation loads used in this investigation. The only possible exception to this trend is the indentation response of the C20 material, which seemingly shows a marginal increase in  $K_{Ic}$  with indentation load. Toughness increases with indent load are usually observed in materials exhibiting R-curve behavior.

Microstructural observations of the crack path seem to support the trends in the toughness values. Examination of the crack path of the MA20 material under polarized light as well as in the SEM (Fig. 4-4a) revealed that the crack propagation was relatively straight, with a substantial portion of the crack length being transgranular and through the silicide matrix. A limited amount of crack deflection was also evident. While modulus differences could also contribute to crack deflection, MoSi<sub>2</sub> and SiC have elastic moduli that are nearly identical. For the most part, the cracks appeared to propagate through the matrix, and in some instances, the crack cut through the SiC particles. The absence of any interfacial debonding along the MoSi<sub>2</sub>/SiC interface suggests that the strength of this interface is high and hence, does not contribute to toughening.

Investigation of the crack path in the microstructures of the C20, C40 and MA40 materials showed that all three materials exemplified very similar crack-microstructure interactions. Considering the C40 material as a representative example (Fig. 4-4b), a small amount of crack deflection due to the SiC particles is observed. Evidence of some crack branching is seen, although it does not appear to be extensive. A larger portion of the crack segments were observed to run along the MoSi<sub>2</sub>/SiC interface as well as through the SiC particles, when compared to the MA20 material. Presumably, these differences could have contributed to the increased toughness in the case of the C20, C40 and MA20 materials. Alternatively, it is also conceivable that the large differences in the CTEs

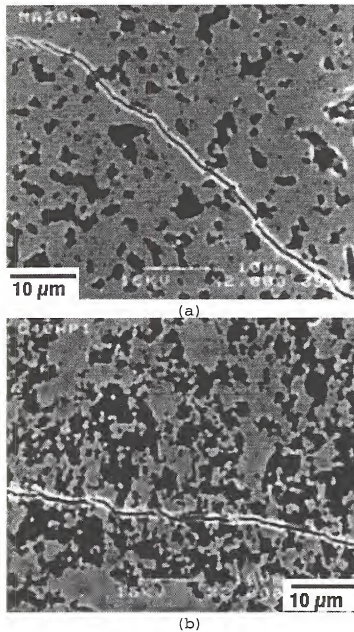


Figure 4-4 Crack path arising from a Vickers indent in (a) UF MoSi<sub>2</sub>/20SiC and (b) CP MoSi<sub>2</sub>/ 40SiC

between the  $\text{MoSi}_2$  and  $\text{SiC}$  at the processing temperatures ( $\Delta\alpha = \sim 4 \times 10^{-6}$  at  $1000^\circ\text{C}$ ) could lead to thermally-induced microcracking, thereby contributing to increased toughnesses, with the magnitude of the thermal mismatch stresses being higher for a wide grain size distribution, such as the C40 and MA40 materials than for a uniform, fine grained microstructure such as the MA20. The propagation of the cracks through the  $\text{SiC}$  particles rather than being deflected around them is also not surprising, since the lower CTE of the  $\text{SiC}$  particles compared to the matrix would cause radial compressive stresses within the  $\text{SiC}$  particles and tensile hoop stresses around the  $\text{SiC}$  particle in the  $\text{MoSi}_2$  matrix thereby causing the crack to be attracted towards the particles [Ric 87].

The results of the room temperature indentation fracture toughness measurements thus seem to indicate that the intergranular glass phase does not influence the toughness as much as the uniformity of the microstructure. However, it should be noted that  $K_{IC}$  determinations based on direct crack length measurements are rather inaccurate and have a high degree of error. Additional testing using at least one other large crack technique will be necessary to verify the trends in toughnesses.

#### 4.3.3 Microstructural Effects on Flow Parameters

##### 4.3.3.1 Stress-Strain Curves

The deformation behavior of both the silica-containing and silica-free material strained under compression were characterized by quasi-steady state flow, as exemplified by deformation under constant stress for extended strains over most of the range of strain rates tested (see Appendix 1 for typical true-stress strain curves). No strain dependence or prior deformation dependence of the flow stress was found, as evidenced from the results of the single strain rate tests and the (multiple) strain rate change tests. Likewise, no evidence of cracking was observed on the external surfaces of the deformed specimens even after extended amounts of strain.

The underlying assumptions behind the assessment of the deformation mechanisms based on SRC experiments are (a) the deformation of a prior stage of the SRC test has no effect on the deformation (hence the flow stress) of the subsequent stages (assumption of no prehistory effect on the deformation) and (b) the flow stress after 0.03-0.04 strain at each strain rate is indicative of the steady state corresponding to that strain rate. Excellent agreement was obtained between the flow stress values obtained at the highest strain rates of the SRC test with those obtained with the corresponding strain rate in the single strain rate (SSR) test, thus validating the assumption of no prehistory effects on subsequent deformation. Strain rate decrement tests were conducted subsequent to the incremental strain rate tests, and, in this case, the flow stresses corresponding to each strain rate (upchange and downchange) showed reasonable agreement, indicating that these flow stress values could be used with reasonable certainty to establish the stress exponents and flow mechanisms.

#### 4.3.3.2 CP MoSi<sub>2</sub>/20 SiC Composites

##### Flow Stress variations with Strain Rate

Figure 4-5a shows a log-log plot of the variation of the steady state flow stress of CP MoSi<sub>2</sub> / 20v/o SiC as a function of strain rate. The data reveals an increase in the flow stress with strain rate, for the range of temperatures tested. Furthermore, the flow stress exhibits a decrease with increasing temperature. The plot of  $\log \sigma$  vs.  $\log \dot{\epsilon}$  shows a smooth sigmoidal variation. Such sigmoidal variations are characteristically exhibited by superplastic materials.

We also note that the flow stresses of the material are relatively low (less than 100 MPa) for most of the temperature range, at relatively high strain rates ( $\sim 10^{-4}$  to  $10^{-3} \text{ s}^{-1}$ ). While desirable for forming operations, such low stresses denote the poor creep resistance of the material. Structural applications require much higher strength levels from the material.

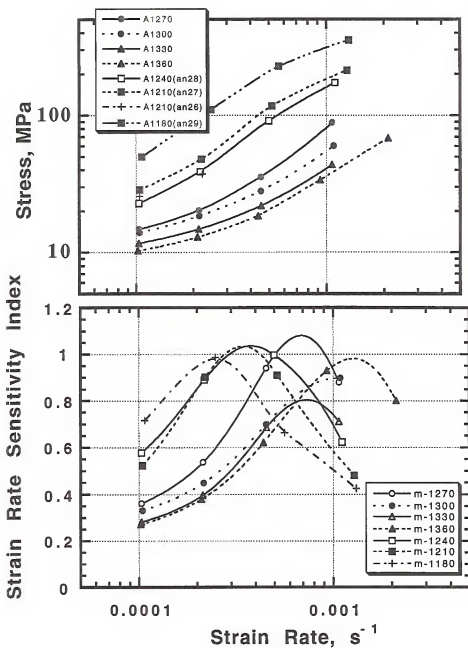


Figure 4-5

(a) Flow stress variations with strain rate, CP MoSi<sub>2</sub>/20 SiC  
 (b) Strain rate sensitivity variations as a function of strain rate.  
 The numerical designation in the legend denotes the test temperature in °C. AN refers to the test specimen designation.

### Strain Rate Sensitivity Variations

Figure 4-5b shows a plot of the variation of the strain rate sensitivity (SRS) as a function of strain rate. For the range of temperatures investigated, the plot of SRS exhibits a maximum with respect to the strain rate. Furthermore, the maximum value of the SRS index is clustered around  $m \sim 1$ , a value that is high. High strain rate sensitivities provide resistance to strain localization and, therefore, are a fundamental criterion for superplastic deformation. While the highest theoretically possible value of  $m$  is one, instances of  $m$  higher than 1, in the range of 1 to 1.1 have been reported for ceramics containing intergranular phases [Lan 81].  $m$  values of 1 describe newtonian viscous flow, where the material is potentially infinitely ductile. Analysis [Har 67] shows that reasonable superplastic ductility is possible for  $0.4 < m < 1.0$ .

With the exception of one temperature, the SRS maximum seemingly displays a trend that is independent of the temperature. Furthermore, the convexity of the plots seemingly decreases with increasing temperature, thereby suggesting an increase in the superplastic deformation (strain rate) window with increasing temperature. Variations in the strain rates corresponding to the peak in the SRS ( $\dot{\epsilon}_{\max}$ ) for each temperature are shown in Table 4-2. It is seen that the SRS maxima,  $(\dot{\epsilon}_{\max})$ , shift toward increasing strain rate values with increase in temperature.

Table 4-2 Strain rates corresponding to SRS peak ( $\dot{\epsilon}_{\max}$ ) for the UF and CP MoSi<sub>2</sub>/ 20 v/o SiC as a function of temperature

Temperature (°C)	UF	CP
1240	$1.0 \times 10^{-4} \text{ s}^{-1}$	$4.0 \times 10^{-4} \text{ s}^{-1}$
1270	$1.5 \times 10^{-4} \text{ s}^{-1}$	$7.0 \times 10^{-4} \text{ s}^{-1}$
1300	$4.0 \times 10^{-4} \text{ s}^{-1}$	$12.0 \times 10^{-4} \text{ s}^{-1}$
1330	$15.0 \times 10^{-4} \text{ s}^{-1}$	$14.0 \times 10^{-4} \text{ s}^{-1}$



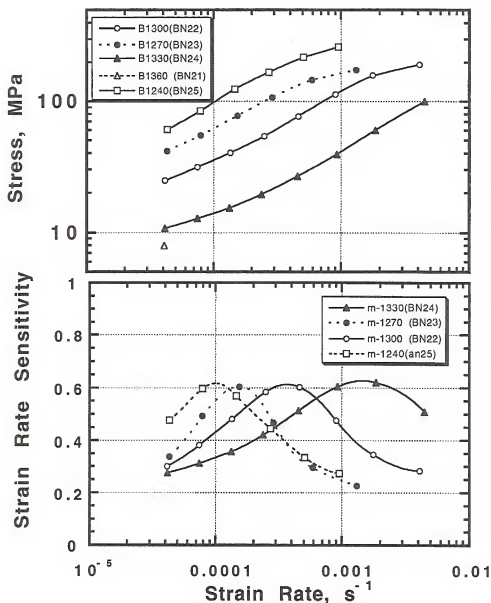


Figure 4-6 (a) Flow stress variations with strain rate, UF MoSi<sub>2</sub>/20SiC  
 (b) Strain rate sensitivity variations as a function of strain rate.  
 The numerical designation in the legend denotes the test temperature in °C. BN refers to the test specimen designation.

#### 4.3.3.3 UF MoSi<sub>2</sub>/ 20 SiC Composites

##### Flow Stress Variations with Strain Rate

Variations in the steady-state flow stress of the UF material as a function of strain rate are shown in Fig. 4-6a. The data reveals trends similar to that of the CP material in that the flow stress shows an increase with an increase in the strain rate, for the range of temperatures investigated. Similarly, the flow stress decreases with increasing temperature and the plots suggest a smooth sigmoidal variation of  $\log \sigma$  with  $\log \dot{\epsilon}$ , again implying the likelihood of superplastic flow.

Again, it is noted that the material exhibits relatively low flow stresses of less than 100 MPa for most of the temperature range, for relatively high strain rates of between  $10^{-4} \text{ s}^{-1}$  and  $10^{-3} \text{ s}^{-1}$ . While the flow stresses are somewhat higher than the CP MoSi<sub>2</sub>/20 SiC material, their levels are insufficient to warrant their use in structural applications.

##### Strain Rate Sensitivity Variations

Variations in SRS as a function of strain rate for the UF MoSi<sub>2</sub>/ 20 SiC are plotted in Fig. 4-6b. For the range of temperatures investigated, the plot of the SRS exhibits a maximum with respect to the strain rate, again showing striking similarities to the CP material. However, the maximum value of the SRS consistently clusters around  $m \sim 0.64$ , for all four temperatures, with no observable dependencies of the SRS values on temperature. As in the case of the CP material, the convexity of the strain rate sensitivity plot decreases (becomes more flat) with increasing temperature, thereby suggesting an increase in the superplastic deformation (strain rate) window with increasing temperature. Also, from the variations in the strain rates corresponding to the peak in the SRS for each temperature (Table 4-2), it is seen that the peak in the SRS ( $\dot{\epsilon}^*$ ) shifts toward increasing strain rates with increasing the temperature, consistent with the trends exhibited by the CP material.

#### 4.3.3.4 UF MoSi<sub>2</sub>/ 5 SiC Composites

##### Flow Stress Variations with Strain Rate

Variations in the steady-state flow stress of the UF material as a function of strain rate are shown in Fig. 4-7a. The data reveals trends similar to that of the CP material in that the flow stress shows an increase with an increase in the strain rate, for the range of temperatures investigated. Similarly, the flow stress decreases with increasing temperature. However, in contrast to the fine grain-sized CP and UF MoSi<sub>2</sub>/20 SiC material, the plots do not exhibit the characteristic sigmoidal variation of  $\log \sigma$  with  $\log \dot{\epsilon}$ , so characteristic of superplastic flow. Rather, the flow behavior corresponds to normal plastic deformation, with transition to higher stress exponents (lower SRS) with increasing strain rate / stress levels.

Of particular note are the relatively high flow stresses ( $\sim 200$  MPa) exhibited by the material at the lower strain rates of  $2 \times 10^{-6} \text{s}^{-1}$ . This is in contrast to the UF and CP MoSi<sub>2</sub>/20 SiC materials, which exhibit relatively low flow stresses of between 20 to 50 MPa at the higher strain rate regimes of between  $10^{-4}$  and  $10^{-3} \text{s}^{-1}$ .

##### Strain Rate Sensitivity Variations

Variations in SRS as a function of strain rate for the UF MoSi<sub>2</sub>/ 20 SiC are plotted in Fig. 4-7b. For the range of temperatures investigated, the strain rate sensitivities decrease with increasing strain rates, and are thus reminiscent of the transition to power-law creep with increasing strain rates (stresses) observed in conventional materials. At the lower spectrum of the strain rates, however (around  $\dot{\epsilon} = 2 \times 10^{-6} \text{s}^{-1}$ ), it is observed that the material displays strain rate sensitivities of between 0.3 and 0.5, indicative of grain boundary sliding contributions.

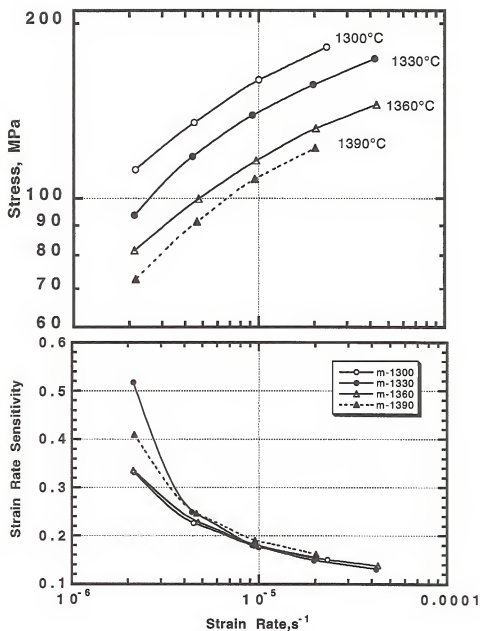


Figure 4-7 (a) Flow stress variation with strain rate, UF MoSi<sub>2</sub>/5 SiC  
 (b) Strain rate sensitivity variations as a function of strain rate.  
 The numerical designation in the legend denotes the test temperature in °C.

#### 4.3.3.5 Silica Effects on Flow Characteristics

Evaluation of the flow stress data for the CP and UF MoSi<sub>2</sub>/20 SiC materials (Fig. 4-8) reveals that at comparable temperatures and at the lower strain rate ranges (for e.g. 1300°C and 0.0001 s<sup>-1</sup>), the low oxygen material exhibits flow stresses which are triple that of the oxygen-containing material. The magnitude of this difference in the flow stress, however, generally decreases at the higher strain rate ranges (~ 0.001 s<sup>-1</sup>) and is about 2 to 2.5 times that of the silica-containing material. Likewise, a comparison of the strain rates under conditions of equal flow stress reveals that the CP material deforms at strain rates which are roughly one order of magnitude higher than that of the low-silica UF material at the lower range of stresses and about 3 times higher strain rates at the higher

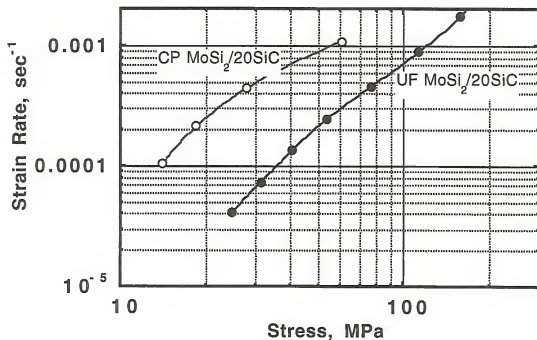


Figure 4-8 Comparison of the flow characteristics of the UF and CP MoSi<sub>2</sub>/20 SiC at 1300°C.

stress levels. Thus, significant reductions in the flow stresses are obtained in the presence of the siliceous phase. It may be interpreted that the incorporation of the siliceous phase could facilitate deformation at lower stresses and higher forming rates.

Comparison of the SRS data of the UF and CP materials reveal some common trends. In general, the data are characterized SRS that initially increase with increasing strain rate and then decrease, for each temperature, thus giving rise to the maxima. For all the temperatures tested, the data exhibits a range of strain rates where the SRS is greater than 0.5. Superplasticity requires deformation regimes with strain rate sensitivities of greater than 0.3 - 0.5. Such behavior is commonly observed in superplastic materials, and corroborates well with the sigmoidal trends in the  $\log \sigma$  -  $\log \dot{\epsilon}$  plots, which are again characteristic of superplastic materials [Pad 80; Edi 76; She 89]. For both materials, the extent of the strain rate window applicable for neck-free deformation, as roughly characterized by the measure convexity if the  $m$  vs.  $\log \dot{\epsilon}$  plot increases with increasing temperature. However, the SRS values are different for the two classes of material, with the oxygen containing material exhibiting higher peak SRS ( $m$  values of 0.64 for the UF material versus peak  $m \sim 1.0$  for the CP material). These peak  $m$  values are indicative of the operative deformation mechanism in region II of the superplastic regime in the  $\log \sigma$  vs.  $\log \dot{\epsilon}$  plot. SRS values close to 1 correspond to stress exponents close to 1 and, in the case of the silica-containing material, are possibly indicative of grain boundary sliding induced by the viscous glass phase [Lan 80]. Likewise,  $m$  values in the vicinity of 0.5 correspond to stress exponents of close to 2 and are normally indicative of conventional mechanisms of superplasticity such as dislocational or diffusional assisted grain boundary sliding.

Furthermore, the strain rates corresponding to the SRS maxima ( $\dot{\epsilon}^*$ ) are 3x to 4x higher for the silica-containing material, as opposed to the low-oxygen material (Table 4-2). Taken in perspective, the higher peak strain rate sensitivity values and the lower flow

stresses required for deformation of the oxygen containing material imply that the silica phase contributes to enhanced formability of the MoSi<sub>2</sub>/SiC composite.

In both of the above cases, the relatively fine microstructures promote deformation under low flow stresses, with or without the presence of silica. The low flow stresses, relatively fine grain size, homogeneous coarsening-resistant two-phase microstructures, relatively large crack-free deformation to large strains (albeit under compression), and presence of a well defined regime of strain rates where  $m > 0.5$ , all point to the likely operation of superplastic deformation in this material.

It is to be noted that the above assessments on the superplastic deformation of the material are based on the data obtained from compression tests. Further evidence based on tensile testing would be necessary not only to corroborate the data trends obtained in compression, but also to determine the extent of tensile elongations feasible in this system.

#### 4.3.4 Microstructural Effects on Deformation Mechanisms

The operating mechanisms for high temperature deformation are typically identified through an analysis of the stress and grain size exponents, activation energies, and a comparison of the undeformed and post-deformed microstructures. In the following section, we present the analyses and the relevant discussion on the effects of silica and grain size on the deformation mechanisms.

##### 4.3.4.1 UF MoSi<sub>2</sub>/ 20 SiC

Figure 4-9 shows a plot of the stress exponent of the silica-free UF MoSi<sub>2</sub>/ 20 SiC material as a function of temperature. The stress exponent values start in the range of ~ 2.1 at around 1240°C and gradually drop to around 1.6 at 1330°C.

The activation energies for the deformation of the silica-free material were also obtained between 1240°C and 1330°C, as shown in Fig. 4-10. The activation energy

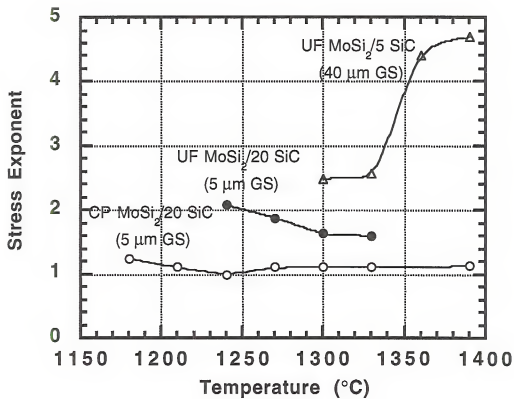


Figure 4-9 Variation of the stress exponent with temperature for MoSi<sub>2</sub>/SiC composites.



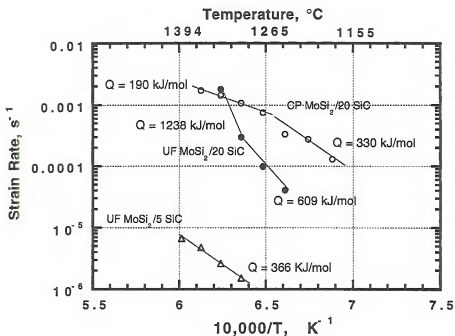


Figure 4-10 Temperature dependence of strain rate for MoSi<sub>2</sub>/SiC composites. The activation energy evaluations correspond to stress levels of 60 MPa for the CP and UF MoSi<sub>2</sub>/20 SiC material, and 100 MPa for the UF MoSi<sub>2</sub>/5 SiC material.

plot seemingly divides into two regimes, with values of 609 kJ/mol between 1240°C and 1300°C and ~ 1200 kJ/mol in the range from 1300°C to 1330°C.

Microstructural evaluation of a typical post-deformed microstructure deformed to stage II to a strain of 0.23 is presented in Fig. 4-11. Comparison of the undeformed and post-deformed microstructures (Figs. 4-11a and 4-11b) reveals that the grain sizes remain unchanged throughout the deformation. Furthermore, the grains remain essentially equiaxed through the deformation, with no detectable elongations for large strains. A similar trend was detected in specimens tested through the range of temperatures.

The values of stress exponent obtained for the silica-free fine-grained material are in the same range as those observed for other intermetallic systems (such as two-phase Titanium Aluminides) which have been shown to exhibit superplasticity [Che 92, Ima 92]. Generally, the region II superplastic behavior of these materials is characterized by SRS variations between 0.5 and 0.6 ( $n$  values of between ~ 1.5 and 2). The deformation mechanism corresponding to stress exponent values of 2 is generally attributed to grain boundary sliding controlled by interfacial reaction [Ash 69, Gre 70, Bur 72, Can 80], as indicated by the models developed by Mukherjee [Muk 71] and Langdon [Lan 70]. In this case, the rate controlling mechanism is either the climb motion of dislocations or their annihilation at the grain boundaries, based on the microstructural evidence and stress exponents. The slight drop in the value of the stress exponent from ~2.1 to ~ 1.6 with an increase in the temperature indicates slight enhancements to the sliding mobility of the grain boundaries.

The activation energy values of 609 kJ/mol and 1238 kJ/mol corresponding to these temperatures are higher than the values normally associated with the diffusion of the individual atomic species in the intermetallic lattice and thus cannot be simply ascribed to lattice diffusion. Higher than normal activation energy values of deformation are usually attributed to interfacial reaction limited processes [Lap 93]. In these cases, the kinetics of mass transport depend not only on the rate controlling diffusivities, but

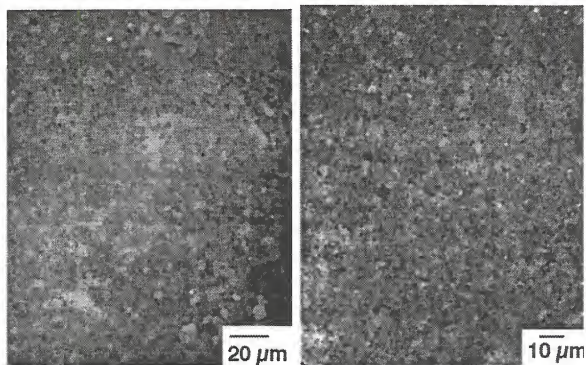


Figure 4-11 Polarized light micrographs of UF MoSi<sub>2</sub>/ 20 v/o SiC (a) undeformed microstructure (b) deformed at 1300°C to  $\epsilon = 0.23$  at  $\dot{\epsilon} = 3.2 \times 10^{-4} \text{ s}^{-1}$ . The longitudinal direction is the direction of application of stress.

also on the atom attachment / detachment at the grain boundaries. As mentioned earlier, such processes have stress dependencies of strain rates of between 1 and 2. It should be mentioned that activation energy values of between 300 - 450 kJ/mol have been reported for the dislocation creep of polycrystalline MoSi<sub>2</sub> and MoSi<sub>2</sub>/ 20 SiC composites [Bos 92, Sad 92, Wei 92].

It should also be pointed out here that the absence of reliable diffusivity data is a common shortcoming encountered in the analysis of deformation behavior of most intermetallic systems. A further complication arises from the effects of second phases such as SiC as in the present work, since it is well known that the incorporation of second phases changes the apparent activation energy of flow.

#### 4.3.4.2 CP MoSi<sub>2</sub>/20 SiC

Figure 4-9 again shows a plot of the stress exponents as a function of temperature for the silica-containing CP MoSi<sub>2</sub>/ 20 SiC. The stress exponents for the silica containing material hover around 1.1 and remains constant through the range of temperatures from 1180°C to 1390°C. We recall that in contrast, the stress exponents of the silica-free material of the same grain size range from around 2.1 at 1240°C and gradually decrease to 1.6 at 1340°C. Consequently, and as already noted in an earlier section, we note that the strain rate sensitivity is enhanced due to the presence of the intergranular silica.

As detailed before, the activation energy for the deformation was obtained from the slope of the semi-logarithmic plot of the strain rate versus the inverse absolute temperature at a constant applied stress (Fig. 4-10). We note that the activation energy data of the silica-containing material divides into two regimes with different slopes, for the temperature range under consideration, thus indicative of a change in deformation mechanism at around 1270°C. In the regime from 1180°C to 1270°C, the activation energy for flow is about 330 kJ/mole, and in between 1270°C to 1390°C, it is around 190 kJ/mol.

Microstructural evaluation of a typical post-deformed microstructure deformed to stage II to a strain of 0.28 is presented in Fig. 4-12. Comparison of the undeformed and post-deformed microstructures (Figs. 4-12a and 4-12b) reveals that the grain sizes remain unchanged throughout the deformation. Furthermore, the grains remain essentially equiaxed through the deformation, with no detectable elongations for large strains, thereby suggesting the likely operation of grain boundary sliding mechanism. It should be noted that the specimens exhibit equiaxed microstructures after deformation throughout the range of temperatures.

The stress exponents measured in the CP material in the superplastic range are in the range of 1.0, lower than the value of 2.5 measured by Sadananda et al. for polycrystalline  $\text{MoSi}_2$  with a grain size of  $\sim 30 \mu\text{m}$  but well in the range typically observed for ceramics. In such materials with intergranular phases, stress exponents between 1 and 2 are generally observed [Hig 95, Cho 91, Nau 90, Hwa 90, Yos 90, Kaj 93, Kaj 95, Gus 93]..

We now turn to analyzing the effect of the silica phase. Grain boundary sliding is the deformation mechanism (with  $n \sim 1.6$  to 2.1) for  $\text{MoSi}_2/\text{SiC}$  with grain sizes in the range of 5-7  $\mu\text{m}$ , as evident from the results of the silica-free material. However, the addition of the glass phase, the stress exponents drop to close to 1, indicative of viscous flow. A rather surprising finding is the existence of stress exponent close to 1 for all temperatures, especially for temperatures below 1250°C, whereas, for the same temperature range, the silica-free material exhibits stress exponents of 2. Considering the near identical microstructural scales of the two materials, it is therefore clear that the presence of the intergranular phase affects the deformation behavior at the lower temperatures as well. This finding is somewhat unexpected, since it was anticipated that the glass phase would exert an influence on its deformation behavior only at temperatures above its softening point.

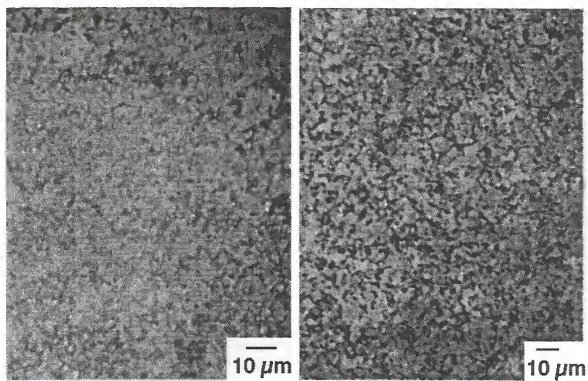


Figure 4-12 Polarized light micrographs of CP MoSi<sub>2</sub>/ 20 v/o SiC (a) undeformed microstructure (b) deformed at 1300°C to  $\epsilon = 0.28$  at  $\dot{\epsilon} = 1.2 \times 10^{-4} \text{ s}^{-1}$ . The longitudinal direction is the direction of application of stress.

In considering the possible effect of a liquid / amorphous intergranular phase on the elevated temperature deformation, we note that the siliceous phase could effect deformation in two ways:

(a) It could act to reduce friction between the grains, thus promoting grain boundary sliding and thus lead to a resultant enhancement of strain rates.

(b) Alternatively, the liquid phase could provide a high diffusivity path (compared to grain boundary or lattice diffusion) for the diffusional creep process. This would leads to enhancement in the strain rate.

Regardless of the deformation mechanism involved, we also note that for the intergranular phase to enhance creep requires for the liquid/ amorphous phase to be spread over the grain boundaries and support a normal stress during the deformation.

In considering the possible deformation mechanisms associated with stress exponents of close to unity, we note that Nabarro-Herring and Coble diffusional processes are typically associated with stress exponents close to unity. In the case of the Nabarro-Herring mechanism, atom transport occurs through lattice diffusion from the grain boundaries under compression to those under tension, with the activation energy of the mechanism corresponding to that of lattice diffusion of the slowest diffusing species. The Coble mechanism, while essentially obeying near newtonian behavior with near-unity stress exponents, rather relies on the short circuit atom transport along the grain boundaries, with the process activation energies corresponding to that of grain boundary diffusion. It is generally well established [Fro 82] that for most metals and alloys,  $Q_{GB} = (0.6-0.7) Q_{lattice}$ . Assuming the lattice diffusion to be controlled by the molybdenum movement through the silicide lattice, and estimating the diffusivities semi-empirically as outlined in Chapter 2, we find that  $Q_{lattice}$  equals 250-350 kJ/mol. This in turn yields  $Q_{GB}$  values in the vicinity of 200 kJ/mol, values close to those observed in the high temperature ( $T > 1270^{\circ}\text{C}$ ) regime. While it is thus tempting to ascribe the observed stress exponent values of unity of the silica-free material to these diffusional creep

processes, the absence of any grain shape or aspect ratio change through the deformation of the silica-containing material precludes their operation. Diffusional creep processes such as Nabarro-Herring and Coble creep rather involve grain elongation along the direction of stress due to stress directed atom/ vacancy transport, which is in contradiction with the observations of equiaxed microstructures observed after extended amounts of deformation evidenced in this investigation. Therefore, Coble creep is ruled out as a possible deformation mechanism; rather, grain boundary sliding influenced by the viscous phase is the most probable deformation mechanism.

Thus, at temperatures above 1270°C, the silica-containing material exhibits liquid enhanced grain boundary sliding (lubricated flow), with stress exponents of close to unity and activation energies of 190 kJ/mol. Similar values of activation energy and stress exponent have been reported by Wolfenstine et. al on plasma sprayed MoSi<sub>2</sub>/SiC [Wolf 94] and by Hynes et al. [Hyn 91] on powder processed MoSi<sub>2</sub>. As alluded to earlier, the absence of any noticeable shape change in this regime, along with the change in activation energy, possibly indicates a change in the deformation mechanism

It should also be noted that the activation energy for the viscous flow of pure silica is higher (711 kJ/mol) than the observed activation energy for flow of ~190 kJ/mol in region II. While it is known that minor amounts of network modifiers such as alkali oxides or hydroxyl groups lower the energy slightly, the observed values are significantly low so as to be explained on the basis of such network modifiers. It is also worth mentioning that similarly low values of activation energy have been previously reported in the high temperature flow regime of silica-containing MoSi<sub>2</sub> by Hynes (232 kJ/mol) and by Wolfenstein (190 kJ/mol). The activation energies reported here are far lower than those reported by Sadananda (430 kJ/mol) for monolithic MoSi<sub>2</sub> with a significantly larger grain size.

In the temperature range between 1180°C and 1270°C, the material again exhibits newtonian viscous behavior, with stress exponents close to unity and activation energies



in the range of 330 kJ/mol. In view of the lack of diffusivity data, the deformation mechanism operating in this temperature regime is unclear, although it is possible that solution-precipitation creep is a possible mechanism, in view of the solubility of molybdenum in silica [Cla 95].

The trends in the activation energy of the silica-containing material are worthy of mention. Generally, for pure metals and intermetallics, a variety of deformation mechanisms operate in parallel and independent of one another, with the fastest process being the rate-controlling. The activation energy of such parallel creep processes increases with increase in the temperature, with the lower activation energy boundary diffusion mechanisms dominating at the lower temperatures, and a preponderance of the higher activation energy lattice mechanisms at higher temperatures. The silica-free material, as discussed in the earlier section, obeys this general trend, with activation energies of  $\sim 600$  kJ/mol in the lower temperature ranges (1240-1300°C) and  $\sim 1200$  kJ/mol in the higher ranges ( $T > 1300^\circ\text{C}$ ). On the other hand, the silica-containing material displays an opposing trend, with a transition from a higher to a lower activation energy from  $\sim 330$  kJ/mol to  $\sim 190$  kJ/mol at around 1270°C. Such trends are interpreted in conventional creep literature as indicative of the operation of a sequential deformation process, with the slowest process rate determining. More recently, however, such trends have also been reported in deformation studies on a wide variety of metallic and ceramic systems with low melting intergranular phases [Hig 95, Cho 91, Nau 90, Hwa 90, Yos 90, Kaj 93, Kaj 95, Gus 93]. In these systems, the temperature associated with the transition in the activation energies has been successfully correlated with phase changes in the intergranular phase (specifically melting of eutectic intergranular phases) [Hig 95].

#### Silica phase Redistribution

An implicit assumption throughout the preceding discussion is that the siliceous phase was present in adequate amounts at the grain boundary surfaces so as to affect the deformation mechanisms described. We recall that the intergranular phase is initially

present in the undeformed microstructures as discrete globular particles at grain junctions and triple points. It is believed that the grain switching events associated with the grain boundary sliding mechanism generate local shear stresses at the boundaries, under the influence of which the silica phase is forced to spread along the grain boundary. Since the grain switching processes entail a considerable degree of grain boundary deformation/accommodation [Ash 73], it would also lead to large scale redistribution of the intergranular phase as a "forced" continuous film along the grain boundaries. Subsequently, steady state conditions dominated by lubricated diffusional creep would set in, leading to an exponent of  $n \sim 1$ .

A clear distinction is made here in emphasizing the non-wetting characteristics and the non-equilibrium morphological configuration of the siliceous phase throughout this shear-driven redistribution process. Accordingly, the liquid / amorphous silica film may be considered to be held in place only under the action of the shear stresses at the boundary. Under this assumptions then, the siliceous film would revert to its globular configuration upon the removal of the loads. This argument is based on the microstructural observations that the as hot-pressed  $\text{MoSi}_2$  has spheroidal silica particles, and hot pressing may also be alternatively viewed as high temperature deformation under compression.

Following the postulates laid forth in the preceding paragraph, it can also be surmised that the redistribution should occur at a threshold stress, the magnitude of which is sufficient to initiate the grain switching events. The argument is based on the fact that prior to the actual switching event, the microstructural conditions for switching are identical in the silica-free and silica-containing materials. (The physical origins of the threshold stress have been enumerated in Chapter 2). Indeed, threshold stress analysis of the strain-rate-stress data reveal that the threshold stress is less than 10 MPa for the silica-containing material. Furthermore, the threshold stress is identical in both the silica-containing and silica-free materials throughout the range of temperatures investigated.

Subsequently to the grain boundary sliding / switching processes, silica-aided grain boundary sliding occurs, provided that a sufficient volume fraction of the silica phase is sufficient to cover a substantial portion of the grain boundary area.

From the above discussion, the occurrence of a grain boundary lubricated viscous sliding mechanism would require the following constraints:

(1) A volume fraction of the glass phase that is greater than the percolation threshold. The percolation threshold could depend on the average grain size

(2) Temperatures high enough for the facilitation of viscous flow of the intergranular phase.

(3) Stresses high enough to enable the siliceous phase to be redistributed under the influence of the grain switching events.

Thus, condition (1) mandates the presence of a critical volume fraction of silica,  $V_{\text{thresh}}$  for sliding to occur. Condition (2) requires a threshold stress for silica phase redistribution, at a level that is similar to the silica-free material with similar grain size and second phase microstructural parameters. Condition (3) mandates a minimum temperature above which the viscosity of the amorphous silica phase is sufficient for it to facilitate redistribution. We also note that it is not necessary for the siliceous phase to melt for the redistribution to occur.

#### 4.3.4.3 Coarse Grain-Sized Material

Figure 4-9 shows a plot of the variations of the stress exponent of the UF MoSi<sub>2</sub>/5 SiC material (40  $\mu\text{m}$  grain size) as a function of temperature. Considering the trends in the stress exponent, we note that the data seemingly group under two regimes:

(a) At temperatures below 1330°C, the stress exponent values range around 2.5 and

(b) at temperatures above 1330°C, the stress exponent experiences a jump and range between 4.5 and 4.7.

A plot of the activation energy for this material is shown in Fig. 4-10 . We take note of an interesting observation, namely, the slope of the plot is single valued, thereby indicating that the two temperature regimes of the stress exponent are governed by the same rate limiting thermally activated process.

Microstructural evaluation of a typical post-deformed microstructure deformed to a strain of 0.26 is presented in Fig. 4-13. Comparison of the undeformed and post-deformed microstructures (Figs. 4-13a and b) reveals a classic plastic deformation process, as evidenced by significant changes in the grain size and aspect ratios during the deformation process. Furthermore, the strain continuity is maintained across the grain boundaries, with no evidence of microcracking.

Considering the deformation above 1330°C, we note that the UF MoSi<sub>2</sub>/ 5 SiC material exhibits stress exponents of  $\sim 4.7$ , an activation energy of deformation of 366 kJ/mol, and significant changes in the shape and aspect ratios of the grains before and after deformation, indicating significant dislocation activity. Furthermore, the deformation is crack free, with the maintenance of strain continuity across the grain boundaries. These observations suggest the strong likelihood of operation of dislocational deformation mechanisms.

In ordered systems having 5 interpenetrating slip systems, power law creep processes generally occur at  $n \sim 5$  and are ascribed to the glide and climb of dislocations controlled by the climb process [Cho 91]. Single crystal deformation studies indicate the onset of climb at temperatures above 1300°C, as evidenced by the presence of copious amounts of low angle grain boundaries [Mal 95]. The onset of climb activates additional slip systems and aids in the meeting the Von Mises criterion of 5 independent slip systems.

The activation energies of 366 kJ/mol reported for the deformation of the large grained MoSi<sub>2</sub>/5 SiC in this investigation are in the same range of activation energies reported by other investigators for polycrystalline MoSi<sub>2</sub>. The activation energy

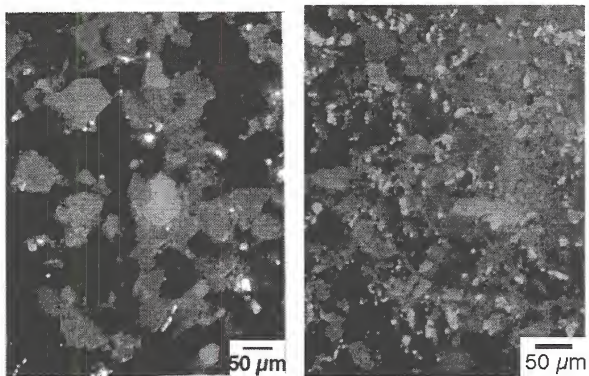


Figure 4-13 Polarized light micrographs of UF MoSi<sub>2</sub>/ 5v/o SiC (a) undeformed microstructure (b) deformed at 1300°C to  $\mathcal{E} = 0.26$  at  $\dot{\mathcal{E}} = 4 \times 10^{-6} \text{ s}^{-1}$ . The longitudinal direction is the direction of application of stress.

of the deformation process would be expected to correspond to the diffusion of the slowest moving species controlling the deformation at the temperature. In view of the fact that silicon is the faster diffuser in the metal silicide systems, one could therefore possibly interpret, albeit with some caution, that the activation energies obtained through the high temperature deformation experiments would correspond to that of the diffusion of molybdenum in  $\text{MoSi}_2$ .

The deformation of the UF  $\text{MoSi}_2/5 \text{ SiC}$  material below  $1330^\circ\text{C}$  is characterized by a stress exponent of  $\sim 2.5$  and an activation energy of  $366 \text{ kJ/mol}$ . These are indicative of a predominantly grain boundary sliding deformation mechanism, with the rate controlling step being the climb of the grain boundary dislocations. It should also be noted that only 4 independent slip systems operate in this temperature range. Therefore, contiguous deformation across the grain boundaries is difficult to achieve. Stress exponent values in the vicinity of 3 have often been reported in systems with less than 5 interpenetrating slip systems.

#### 4.3.5 Superplastic Behavior

Cavitation and grain boundary cohesivity may limit the range of uniform deformation under tension, and thus uniaxial tensile or biaxial stretch tests are needed to confirm the formability under tensile stresses. The room temperature fracture data demonstrate that the presence of the glass phase does not significantly affect the room temperature toughness.

The trends in the stress exponents (values tending close to 1.5-2.0 for the UF material and  $n \sim 1$  for the CP  $\text{MoSi}_2/20 \text{ SiC}$  material respectively) are indicative of a high strain rate sensitivity. This stems from the deformation mechanism which is normally associated with such values, namely, grain boundary sliding accommodated by either grain boundary or bulk diffusional mechanisms, or glass phase enhanced lubricated flow or solution-precipitation creep. A common prerequisite for superplastic flow (structural as

opposed to transformation superplasticity) in most materials is a high strain rate sensitivity ( $m \sim 0.5$  to  $1$ , i.e.,  $n = 1/m \sim 1$  to  $2$ ), a relatively high homologous temperature of deformation ( $T_h > 0.5$ ) and a relatively fine grain size of less than  $10 \mu\text{m}$ . The first requirement is mandated by the need for uniform neck-free deformation, which necessitates a large dependence of the flow stress on the strain rate (and hence high strain rate sensitivities), while the latter requirements are based on the need to accommodate the deformation due to grain boundary sliding (typical of superplastic flow), by concurrent bulk (Nabarro-Herring) or grain boundary (Coble) diffusional processes, with the appropriate grain size dependencies of the creep rate ( $p=3$  for Coble creep, and  $p=2$  for Nabarro Herring Creep). From a physics of flow, continuity of adjacent grains during deformation by grain boundary sliding has to be accommodated for by the diffusion of atomic species within the length scale of the boundaries and within the time scale as dictated by the imposed strain rate on the process. These requirements would be met by a combination of factors such as fine grain sizes (hence small diffusional distances) and / or high diffusivities (brought about by high homologous temperatures and the glass phase). It is to be noted that for the case of lattice diffusion in ordered compounds such as ceramics and intermetallics, the diffusivity requirement of the *slowest* moving species *must* be met in order to achieve accommodated grain boundary sliding.

Grain boundary cohesivity and the operation of sufficient slip systems are the requirements for tensile superplasticity. In the case of most ceramic systems such as  $\text{Al}_2\text{O}_3$ ,  $\text{ZrO}_2$ , and  $\text{SiC}$  which have been shown to exhibit superplasticity, the low diffusivities and the high melting points dictate that the diffusional distances be short for accommodated grain boundary sliding. This is perhaps why these materials exhibit superplastic flow in the regime of ultra fine ( $<1 \mu\text{m}$ ) grain sizes. Our results on  $\text{MoSi}_2$  indicate the possibility of accommodated grain boundary sliding processes in grain size regimes between  $5 - 10 \mu\text{m}$  at  $1573^\circ\text{C}$  ( $T_h \sim 0.7$ ), perhaps indicative of the relatively higher diffusivities of the slower moving species in this system, viz. Mo at these temperatures.

The high strain rate sensitivity is exhibited by the CP and UF MoSi<sub>2</sub>/ 20 SiC at moderate strain rates in both the materials at a temperature of 1300°C. The silica-free material with an average grain size of 5 μm shows promise of superplastic workability within the processing window at temperatures of 1350°C, as shown in Fig. 4-14. The limiting parameters of the forming window were chosen, keeping in view the need for economically viable forming rates ( $> 0.0001 \text{ s.}^{-1}$ ), and the design limitations ( $\sim 40 \text{ MPa}$ ) of the graphite tooling material which would be used for forming, at these elevated temperatures of greater than 1200°C. While the focus of our present experiments was in obtaining silica-free microstructures without any consideration whatsoever being given to minimize the grain size while processing, it is quite conceivable that the workable temperature range of the silica-free material would be lowered, if adequate reductions in the grain size were achieved from their present levels. The optimum working temperature range that would be desired for hot working would be in the range of 1200°C, since the tooling capabilities that exist for the working of molybdenum and nickel based alloys could then be used. Even with the current grain size levels of 5 μm, an increase in temperature by about 50 to 100°C from the current 1300°C levels would make superplastic deformation feasible at reasonably economical strain rates and low flow stresses for the silica-free material, as defined by a processing window. Improvements in the creep strength and lowering of the creep rates subsequent to superplastic working could be achieved by appropriate grain growth treatments that would shift the deformation mechanism from the grain boundary sliding regime to one involving dislocation creep. The limiting grain size that could be derived through grain growth would, of course, be controlled by the volume fraction and particle size of the SiC, approximately following the Zener relation,  $R_{\text{MoSi}_2} = (4r_{\text{SiC}}) / (3f_{\text{SiC}})$ . The volume



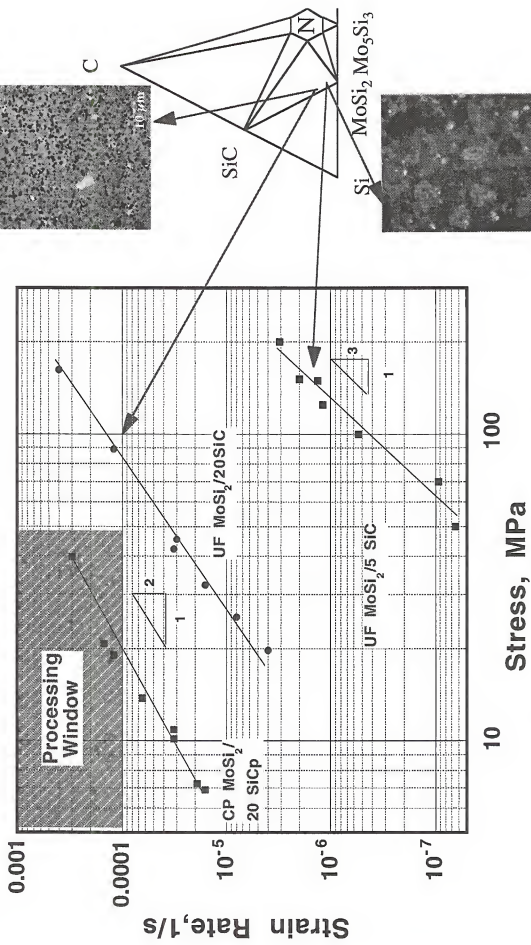


Figure 4-14 Composition-structure-flow relationships of some  $\text{MoSi}_2/\text{SiC}$  materials.

fraction of SiC desired for optimum creep strength could then be controlled by simply controlling the composition of the mechanically alloyed powder as detailed elsewhere.

Flow softening has been reported in MoSi<sub>2</sub> for temperatures as low as 900°C [Gib 92] and that deformation under constant flow stress has been reported in plasma sprayed MoSi<sub>2</sub>/SiC at 1300°C [Sam 92]. The former was attributed to large scale microcracking during the compressive deformation of large grain samples due to unaccommodated grain boundary strains possibly resulting from an insufficient number of slip systems at these temperatures. The latter is presumably due to substantial amounts of silica in these materials. While the latter would also lead to high strain rate sensitivities, it seems probable that the deformation in this case is due to liquid enhanced sliding due to the viscous glass phase (Rachinger sliding). Such a scenario could imply the high temperature strength of the material would be indirectly dictated by the strength of the deforming phase, i.e. silica, thereby questioning the viability of the processing routes. Thus, our results on high strain rate sensitivity in silica-free MoSi<sub>2</sub>/SiC composites are thus perhaps the first demonstrable evidence of superplasticity due to diffusionaly accommodated grain boundary sliding in the MoSi<sub>2</sub> system, with the concomitant possibilities of superplastically forming a material with superior properties above 1200°C.

The flow stresses for the CP composite, containing a non-wetting silica phase and having a comparable grain size to the UF composite, are significantly lower than the UF composite at all strain rates, with the magnitude of the difference increasing at higher strain rates. Our results thus run counter to the only known investigation of the effect of a non-wetting phase on the creep properties, where it was reported that the presence of non-wetting intergranular phase had no effect on the deformation mechanisms in experiments conducted in temperature ranges straddling the melting temperature of the non-wetting intergranular phase.

Contrary to the expectation that the *in-situ* SiC reinforcements at the grain boundaries and triple points would enhance high temperature strength by virtue of the pinning effect the SiC particles would have against sliding, this work demonstrates the dominance of the grain size effect over that of reinforcements on the deformation mechanisms, as evidenced by the operation of the grain boundary sliding process in both silica-free and silica-containing materials. It is quite possible that the SiC particles do enhance the resistance to deformation by grain boundary sliding, as evidenced by the higher activation energies for the silica-free material.

Finally, the processing route has a significant bearing on the properties measured in this section of the investigation. As noted in Chapter 2, structural superplastic flow requires uniform deformation which imposes stringent requirements on the material microstructure insofar as near uniform grain sizes and uniform chemical homogeneity are required; otherwise shear bands might be nucleated at heterogeneities which, in turn, would lead to non-uniform deformation and subsequent loss of superplastic characteristics. The current investigation utilized mechanical alloying, characteristically producing fine powders not only of precise and homogeneous composition and stoichiometry, but also of uniform structure; this, in turn, insured the formation of the chemically and microstructurally homogeneous fine grained microstructures so very essential for the properties demonstrated in this work. The use of the fine powders derived from mechanical alloying would also enable the use of lower consolidation temperatures and thence to a fine grain sized material and superplasticity.

#### 4.3.6 Implications of Superplastic Behavior

The possibility of superplasticity in the silica-containing material, while having negating implications in the high temperature regime ( $T > 1200^{\circ}\text{C}$ ), nevertheless has important applications in the processing of  $\text{MoSi}_2$ -based materials for use in the lower temperature regimes below the softening temperature of silica. As has been clearly

demonstrated in this and numerous earlier reports, the presence of the viscous intergranular phase promotes grain boundary sliding, thus enhancing the formability of the material at lower temperatures through superplastic forming mechanisms. This work has also demonstrated that the presence of the non-wetting intergranular phase has a negligible (if not a benetic) effect on the fracture properties extending from room temperature up to the BDTT. Also considering the passivity of the silica to most chemical environments in addition to all the above mentioned facts, it would be well worth considering forming fiber reinforced, silica-containing, fine grained  $\text{MoSi}_2$  based composites for low temperature ( $600^\circ\text{C} < T < 1000^\circ\text{C}$ ) applications, with the fiber reinforcement providing the necessary toughening at the lower temperatures. Such a process would of course exploit the superplastic forming characteristics endowed by the silica on the forming process. Fiber stability and fiber-matrix interactions are important issues at the higher processing temperatures. Hence, lower superplastic forming temperatures are preferred, and these could be obtained by modifying the glass transition temperature through the addition of suitable network modifiers to the silica.

The likelihood of the existence of a viable superplastic forming regime at reasonably low temperatures around  $1200\text{--}1300^\circ\text{C}$  for  $\text{MoSi}_2$  opens up a plethora of processing-related opportunities. For instance, it would be possible to perform a whole range of operations ranging from sinter forging to net shape extrusion and diffusion bonding of  $\text{MoSi}_2$ -based composites, besides unlocking avenues in the superplastic forming of  $\text{SiC}$  fiber reinforced composites. The major drawback limiting the use of  $\text{SiC}$  fibers such as Nicalon<sup>®</sup> in the reinforcement of high temperature materials has been their poor elevated temperature stability due to their high oxygen content. This imposes severe processing constraints in attempts to incorporate them into matrices. For instance, Nicalon<sup>®</sup> can withstand a processing temperature of  $1425^\circ\text{C}$  for a maximum of 20 minutes of infiltration by silicon, before suffering irrecoverable degradation. Consequently, the use of fibers is restricted to relatively low temperature processes such

as CVD, CVI, RVI, plasma spraying, reactive melt infiltration, and similar net-shape capable processes, which do not expose the fibers to such high processing temperatures, but are nevertheless plagued by such factors as slow deposition/reaction rates and incomplete reactant conversion, which consequently limit their utility in scale-up efforts. With the apparent superplastic phenomenon in the silica-free  $\text{MoSi}_2/\text{SiC}$  composites, it should be possible to form SiC fiber reinforced  $\text{MoSi}_2/\text{SiC}$  composites by the alternate stack-up of  $\text{MoSi}_2/\text{SiC}$  laminates interspersed with layers of SiC fiber tows, followed by a diffusion bond operation at a relatively benign temperature ( $\sim 1350^\circ\text{C}$ ) in the superplastic flow regime, where the fibers are apt to retain their stability for prolonged periods of time. The vast difference in the CTE between the SiC fibers and the  $\text{MoSi}_2$  would require precautions while processing to eliminate cracking. As has been demonstrated earlier, the cracking problem could be tackled by adopting a two-pronged approach as follows: (a) lowering the effective CTE of the  $\text{MoSi}_2/\text{SiC}$  laminates through control of the composition, as has been demonstrated elsewhere and (b) use of fine diameter fibers (diameter  $\sim 1\ \mu\text{m}$ ), since the magnitude of the CTE mismatch stresses (and hence cracking) is significantly reduced at fine reinforcement sizes. Fine diameter fibers also have the added advantage of possessing higher strength and hence, better ease in handling and processing operations. Caution should be exercised, however, while applying the principle of superplastic forming to the net shape processing of fiber reinforced composites, as the nature of the forming process would considerably distort and alter the fiber inter-layer and intra-layer spacings, thereby leading to variations in the material properties, in addition to the likelihood of fiber damage. These challenges could nevertheless be tackled through appropriate reverse-engineering of the fiber layup and forging processes.

The present study also serves as a case-in-point to demonstrate that significant improvements in the high temperature strength can be derived through a proper understanding and control of the matrix microstructure, and that such additional

improvements in strength could be obtained without blind recourse to compositing approaches. While it is an undeniable tenet that compositing approaches are necessary in order to impart the strength and toughness required for futuristic materials applications, it is equally imperative that the importance of fundamental microstructural parameters such as the grain size and second phase morphology / distribution, and the effect of artificial / *in-situ* reinforcements on the above-mentioned microstructural parameters be reemphasized and carefully manipulated in the successful optimization of the microstructural design of such composites, aside from the thermodynamic stability and interface design considerations that govern composite design.

#### 4.4 Application of the Flow Property Measurements to Process Development

Based on our understanding of the results discussed in the previous sections, it should be possible to manufacture high strength Mo-Si-C alloys to near-net shape, using a multi-step powder metallurgy method involving mechanical alloying, *in-situ* carbothermal reduction reactions, hot consolidation, superplastic forming, and post forming heat treatment operations, in that sequence. Through the process, fully dense, low-silica MoSi<sub>2</sub> alloys consisting of finely dispersed SiC in the MoSi<sub>2</sub> matrix could be readily and reproducibly formed. These alloys could find potential use in the temperature range from 1100°C to 1450°C, provided that their service temperature is lower than the processing temperature. In the following paragraphs, we briefly describe the method of manufacture, and the methodology through which the high temperature strength and related mechanical properties could be tailored through control of the alloy composition and microstructure.

The process of manufacture of low silica, MoSi<sub>2</sub>/ SiC alloys, is as follows. Elemental powders of Mo, Si, and C of the desired composition are subjected to mechanical alloying, with powder compositions chosen so as to result in the formation of MoSi<sub>2</sub> /SiC composites. Subsequently hot consolidated (under conditions described in Chapter 2) would result in the formation of a homogeneous, equiaxed, fine-grained

MoSi<sub>2</sub>/SiC alloys, the microstructures of which would be amenable to superplastic deformation at temperatures around 1200°C and above under specific conditions of strain rate and temperature. The alloys are thus superplastically deformed in this condition (corresponding to UF MoSi<sub>2</sub>/20 SiC in Fig. 4-14). Since the deformation is carried out at very low stress levels without the usual instabilities associated with necking, the process results in the production of near-net shape, dense, crack-free components.

Subsequent to near-net shape forming, the alloys could be heat treated to coarsen the MoSi<sub>2</sub> grain structure and thereby transform them from their temporary superplastic condition (low strength and high ductility) to one of high strength and low ductility (corresponding to UF MoSi<sub>2</sub>/5 SiC in Fig. 4-14).

An important aspect of this processing scheme is the ability to control the final achievable strength in the post-heat treated condition through the indirect control of the grain size in MoSi<sub>2</sub>. The post-heat treatment grain size is determined by the silicon carbide content in the alloy (Zener's theory of grain boundary drag by second phase particles) which is in turn controlled by the starting composition of the powders, as described in Chapter 3. The process thus would afford compositional control to tailor the final strengths of MoSi<sub>2</sub>/SiC alloys. The grain size distribution and the overall microstructure are anticipated to be reasonably uniform and homogeneous throughout the component cross section, thereby resulting in better reliability in the ambient and high temperature properties.

Yet another important aspect of this process is that it results in the production of MoSi<sub>2</sub>/SiC alloys with very low silica content. As alluded to earlier in this chapter, silica elimination would result in significant enhancements to the elevated temperature strength.

In addition for adaptation in conventional forming operations such as extrusion and forging, the UF process could also be used in conjunction with alternative synthesis processes such as plasma spraying. In addition to being able to accurately tailor the strength levels in the alloy, the production of components of intricate shapes and close

tolerances would be facilitated, with the resulting cost reductions due to reduced machining operations.

#### 4.5 Property Comparisons with Other Materials Systems

In this section, we describe the performance characteristics of UF MoSi<sub>2</sub> derived through the process described earlier in this thesis and provide comparisons against existing materials currently being considered for potential high temperature applications.

The yield strength of a material is a benchmark for comparison of high temperature performance. To be considered viable for structural applications as in engine components, yield strength requirements exceeding at least 300 MPa are needed. For example, aluminum alloy components currently used in airframe applications possess yield strength values in the range of ~500 MPa.

Clearly, the data in Fig. 4-15 show that the UF material (UF MoSi<sub>2</sub>/ 5 SiC in the figure) possesses bend strength values that are at least 10 fold higher than the conventionally processed MoSi<sub>2</sub> materials, in the high temperature regimes. Furthermore, the strength values are in the regime where they could be realistically used as high temperature structural materials. Furthermore, as shown in Fig. 4-16 they compare very favorably against MoSi<sub>2</sub> based materials which have been alloyed or composited with whiskers.

Figure 4-17 shows a comparison of the high temperature bend strength characteristics of the UF MoSi<sub>2</sub> material with commercially available structural materials such as Norton Company's Silicon Nitride, Coors's Silicon Carbide, and the French-made SEP (Society for European Aerospace Propulsion systems) Silicon Carbide fiber reinforced Silicon Carbide material. Clearly, the UF material possesses comparable properties to these materials at least upto 1350°C.



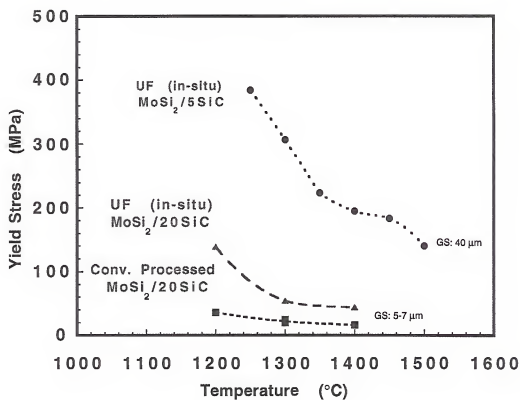


Figure 4-15 Temperature dependence of yield strength of  $\text{MoSi}_2/\text{SiC}$  composites from four-point bend tests.

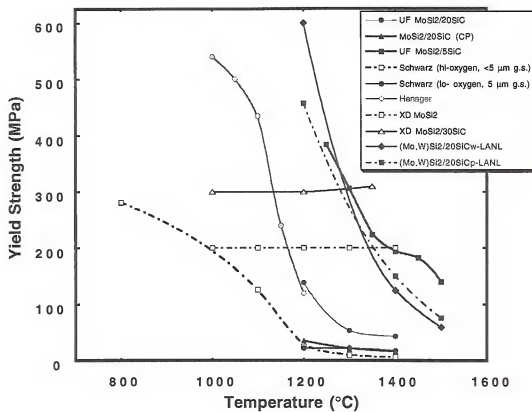


Figure 4-16 Yield strength (four-point bend) comparisons of UF MoSi<sub>2</sub>/ 5 SiC with other MoSi<sub>2</sub> based systems.

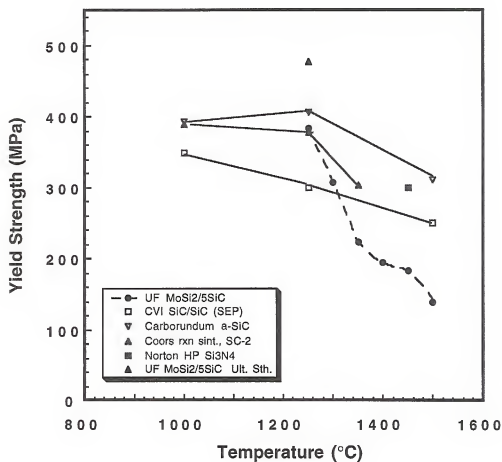


Figure 4-17 Comparison of the yield strength of UF MoSi<sub>2</sub>/5 SiC with the Ultimate strength of competitive ceramic systems.

Dimensional stability of the material under sustained loads, over prolonged periods is another matter of utmost concern in the performance of high temperature aircraft engine components. These are characterized through creep measurements. As clearly seen from Fig. 4-18, the creep rates of the UF material are at least four orders of magnitude lower than the conventional  $\text{MoSi}_2$  material. This roughly translates to a four order of magnitude improvement in the operational life of the component over the conventionally available  $\text{MoSi}_2/\text{SiC}$  material.

Finally, as illustrated in Fig. 4-19, the creep characteristics of the near monolithic UF material (UF  $\text{MoSi}_2/5\text{ SiC}$ ) also place it in the same performance bracket as other commercially available potential high temperature engine component materials such as the Carborundum Company's SiC, Allied Signal's Silicon Nitride and Oak Ridge's Alumina, although significant improvements are warranted.

It should be pointed out that a distinguishing characteristic of the molybdenum disilicide based materials, as opposed to other ceramic materials, is its elevated temperature ductile characteristics. This implies that the material is more 'forgiving' to naturally occurring defects in it such as cracks, which would otherwise prove catastrophic during service and handling. Such damage tolerant characteristics would make it especially attractive from a design and service life perspective. None of the available ceramic materials under consideration in this temperature regime of operation (between  $1200^\circ\text{C}$  and  $1450^\circ\text{C}$ ) exhibit substantial ductility.

Thus, it has been shown in this section that significant operating temperature improvements (to the order of  $300^\circ\text{C}$ ) have been obtained in the  $\text{MoSi}_2$  based materials as a result of the processing methods described in this thesis. In addition, significant improvements have been attained in the creep resistance as well, to at least four orders of magnitude improvement.

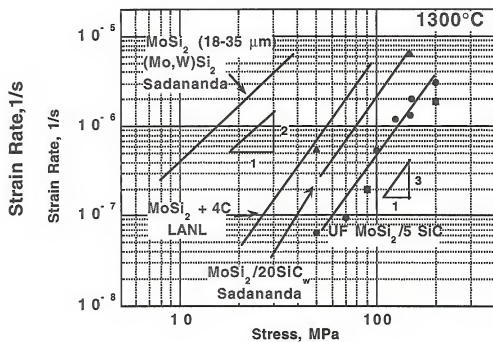


Figure 4-18 Comparison of the creep rates of UF MoSi<sub>2</sub>/5 SiC with other MoSi<sub>2</sub>-based materials at 1300°C.

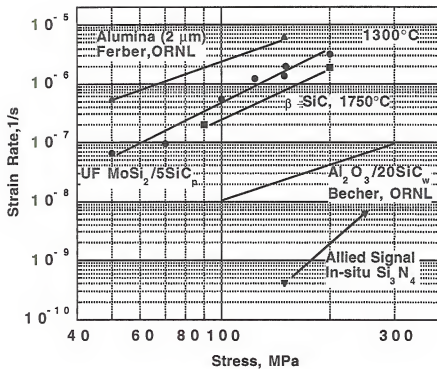


Figure 4-19 Comparison of the creep rates of UF MoSi<sub>2</sub>/5 SiC with other ceramic systems.

## 4.6 Summary and Conclusions

### 4.6.1 Fracture

Indentation measurements indicate that the peak room temperature fracture toughnesses for the silica-free MoSi<sub>2</sub>/SiC composites are similar to those of the CP composites, indicating that microstructural uniformity, rather than the presence or absence of silica, controls the toughnesses in this composite system.

### 4.6.2 Flow

Data on the deformation behavior of MoSi<sub>2</sub>/20 v/o SiC composites suggest the likely existence of superplasticity in this material at temperatures in the vicinity of 1250°C and strain rates in the neighborhood of  $10^{-4}$  s<sup>-1</sup> to  $10^{-3}$  s<sup>-1</sup>, irrespective of the oxygen (silica) content in the material, for matrix grain sizes in the range of 5-8 μm. The presence of the silica phase is, however, found to improve the formability of the material. This result is based on a one-third reduction in the flow stresses, as well as the higher peak values of strain rate sensitivity index exhibited by the materials containing higher oxygen contents. The range of high strain rate sensitivity extends from roughly  $10^{-4}$  s<sup>-1</sup> to  $10^{-3}$  s<sup>-1</sup>. The presence of the glassy phase also leads to a five to ten fold increase in the strain rate, compared to the low-oxygen material, for the range of grain sizes investigated.

Two chief microstructural effects, namely, the silica and the matrix microstructural scale (i.e. grain size) control the high temperature deformation through a host of thermally activated mechanisms operating in the temperature range of 1200-1400°C. The operating deformation mechanisms have been studied as a function of temperature and microstructural variables such as grain size and silica, through an analysis of stress exponents, activation energies, and post-deformation microstructural evidence derived

from compression tests. In the grain size regimes of 5-7  $\mu\text{m}$ , the non-wetting intergranular silica phase has been shown to exhibit stress exponents of unity, characteristic of liquid enhanced grain boundary sliding or viscous sliding aided by solution-precipitation creep. This study further postulates that the initially spheroidal and non-wetting silica undergoes forcible spreading along the grain boundaries due to the local boundary shear stresses associated with the grain switching events, and thus influences the creep properties. For the silica-free  $\text{MoSi}_2/\text{SiC}$  composites in a similar grain size regime, interface reaction-controlled grain boundary sliding has been identified as a probable deformation mechanism. For silica-free composites with matrix grain sizes in the regime of 40  $\mu\text{m}$ , interface controlled grain boundary sliding operates at temperatures below 1330°C, while climb-controlled dislocation creep predominates above this temperature. The study thus shows that a host of deformation mechanisms operate in this material within this relatively narrow temperature range, thus influencing the flow stress, creep rates, and strain rate sensitivities. We note that conventional powder processing routes result in microstructures that are susceptible to a host of boundary deformation processes, which, while being desirable from formability considerations, are not preferred for high temperature strength. A prime factor in prompting the consideration of the silicide as a structural material is its potential for high temperature strength retention, which is anticipated to be developed by the lattice resistance to deformation by its crystal structure. Thus, deformation mechanisms such as climb controlled dislocation creep best utilize the intrinsic resistance offered by the lattice to deformation, while the operation of boundary mechanisms defeat this objective. However, with an understanding of the intricate inter-relationship between the processing and properties, we note that the processing route can be tailored so as to advantageously control the microstructural scale and the intrinsic intergranular phases, and so as to tailor the deformation mechanisms, and, hence, strength and fabricability of the material.



## CHAPTER 5 CONCLUSION

Monolithic  $\text{MoSi}_2$  and  $\text{MoSi}_2$  /  $\text{SiC}$  composites have been synthesized through the mechanical alloying (MA) of elemental molybdenum and silicon powders with and without carbon additions. The interplay between the phase formation sequence in the powders and the microstructural evolution in the consolidated samples has been elucidated. It is shown that the glassy  $\text{SiO}_2$  phase characteristic of conventional powder processed  $\text{MoSi}_2$  can be effectively eliminated by combining mechanical alloying, carbon additions, and an *in-situ* carbothermal reduction reaction. Using this approach, composites consisting of homogeneous, uniformly distributed micron-size  $\text{SiC}$  particulate in an  $\text{MoSi}_2$  matrix have been formed. The ability to vary the reinforcement loading through the control of the nominal starting compositions has also been demonstrated, with  $\text{SiC}$  contents of up to 40 v/o. Along with the ability to effect changes in the reinforcement content, it has also been demonstrated that such compositional control can be used as an effective means of controlling the matrix grain size.

The structural and morphological evolution of the mechanically alloyed powders has been studied as a function of milling time. It has been shown that complete attrition is achieved after 29 hours of alloying. The resultant powders are micron-sized and contain 4 to 7 nm crystallites of molybdenum,  $\alpha\text{-MoSi}_2$  and traces of  $\beta\text{-MoSi}_2$ . The addition of carbon to the starting elemental powder mixture suppresses the formation of  $\alpha\text{-MoSi}_2$  in the fully milled powders. Minor amounts of iron impurities were also found in the powders due to the contamination from the milling media.

The phase evolution studies of the binary and ternary MoSi<sub>2</sub> powders indicated that  $\beta$ -MoSi<sub>2</sub> is stable to 1020°C at heating rates of 10°C/min, in contrast to previous studies on the isothermal annealing of Mo-Si multilayers which demonstrated stabilities to only 800°C. While minor amounts of tetragonal Mo<sub>5</sub>Si<sub>3</sub> were evolved as an intermediate transformation product in the binary MA MoSi<sub>2</sub> powders, the evolution of the ternary MoSi<sub>2</sub> powders showed the formation kinetics of the Nowotny phase C<sub>1Mo<sub>5</sub>Si<sub>3</sub> to dominate that of tetragonal  $\alpha$ -MoSi<sub>2</sub> at lower temperatures. However, temperatures above 1000°C resulted in the progressive decrease in the amount of these higher molybdenum phases.

Indentation measurements indicate that the peak room temperature fracture toughnesses for the silica-free MoSi<sub>2</sub>/SiC composites are similar to those of the CP composites, indicating that microstructural uniformity, rather than the presence or absence of silica, controls the toughnesses in this composite system.

High temperature deformation behavior of silica-containing and silica-free (CP and UF) MoSi<sub>2</sub>/ 20 v/o SiC composites suggest the likely existence of superplasticity in this material at temperatures in the vicinity of 1300°C, irrespective of the oxygen (silica) content in the material, for matrix grain sizes in the range of 5-8  $\mu\text{m}$ . The presence of the silica is found to improve the formability of the material, through a one-third reduction in the flow stress levels, as well as through enhancing the peak values of strain rate sensitivity. The window of high strain rate sensitivity corresponding to superplastic deformation, occurs at reasonably high strain rates extending from roughly  $10^{-4} \text{ s}^{-1}$  to  $10^{-3} \text{ s}^{-1}$ , thus opening up possibilities for economic shape-forming. The presence of the non-wetting glass phase in the MoSi<sub>2</sub>/ 20 SiC material also leads to a five to ten fold enhancement in the strain rates, for the grain size ranges of 5-7  $\mu\text{m}$ .

Thus, the study shows that silica degrades the high temperature compressive and bend strengths at temperatures above 1200°C, with a threefold reduction in flow stress levels in the silica-containing materials compared to the silica-free materials.

Two chief microstructural effects, namely the silica and the grain size are shown to control the high temperature deformation through a host of thermally activated mechanisms operating in the temperature range of 1200-1400°C. In the grain size regimes of 5-7  $\mu\text{m}$  and in the presence of the non-wetting intergranular silica phase,  $\text{MoSi}_2$  exhibits stress exponents of unity, thus indicating the occurrence of liquid enhanced grain boundary sliding or viscous sliding aided by solution-reprecipitation creep. For the silica-free  $\text{MoSi}_2/\text{SiC}$  composites in a similar grain size regime, interface reaction-controlled grain boundary sliding is the probable deformation mechanism. For silica-free composites with larger matrix grain sizes ( $\sim 40 \mu\text{m}$ ), interface-controlled grain boundary sliding operates at temperatures below 1330°C, while climb-controlled dislocation creep predominates above this temperature. A host of deformation mechanisms operate within a relatively narrow temperature range, thereby influencing the flow stress, creep rates, and strain rate sensitivities.

The addition of SiC weakens the high temperature strength of the material, contrary to expectations of strengthening due to their presence at the grain boundaries. The grain refinement effect and the resultant creep strength degradation due to the addition of the SiC overweighs the potential resistance to grain boundary sliding offered by the SiC particles at the grain boundaries.

Conventional powder processing routes result in microstructures which, while being desirable from formability considerations, are not preferred for high temperature strength. Thus, deformation mechanisms such as climb controlled dislocation creep best utilize the intrinsic resistance offered by the lattice to deformation, while the operation of boundary mechanisms defeat this objective. Thus, the importance of developing processing methodologies which result in large grain-sized, silica-free matrices, which utilize the intrinsic properties of the material has been underscored. Through an understanding of the processing- structure- property relationship, the processing route can be tailored to control the strength and fabricability of the material to levels that are

comparable, if not better than those achieved using alloying or traditional compositing approaches.

APPENDIX  
STRESS-STRAIN CURVES OF SELECTED SPECIMENS

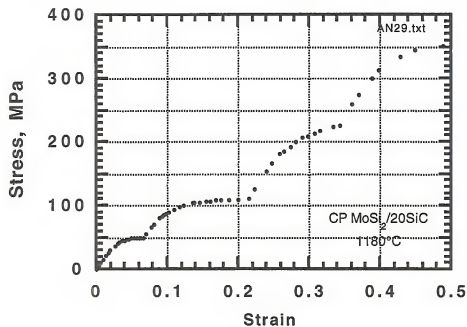


Figure A-1 True stress-strain curves of strain rate change compression tests of CP MoSi<sub>2</sub>/ 20 SiC at 1180°C, at nominal strain rates of  $1 \times 10^{-4} \text{ s}^{-1}$ ,  $2 \times 10^{-4} \text{ s}^{-1}$ ,  $4 \times 10^{-4} \text{ s}^{-1}$ , and  $8 \times 10^{-4} \text{ s}^{-1}$ .

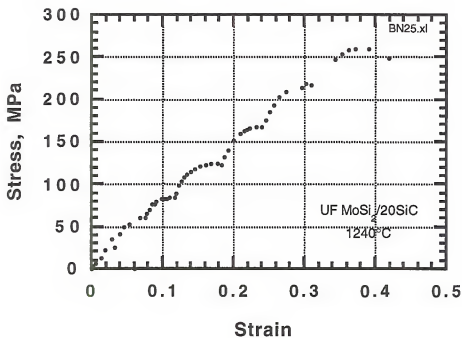


Figure A-2 True stress-strain curves of strain rate change compression tests of UF MoSi<sub>2</sub>/ 20 SiC at 1240°C, at nominal strain rates of  $4 \times 10^{-5} \text{ s}^{-1}$ ,  $7 \times 10^{-5} \text{ s}^{-1}$ ,  $1.225 \times 10^{-4} \text{ s}^{-1}$ ,  $2.14 \times 10^{-4} \text{ s}^{-1}$ ,  $3.75 \times 10^{-4} \text{ s}^{-1}$ ,  $6.56 \times 10^{-4} \text{ s}^{-1}$ ,  $1.149 \times 10^{-3} \text{ s}^{-1}$  and  $2.01 \times 10^{-3} \text{ s}^{-1}$ .

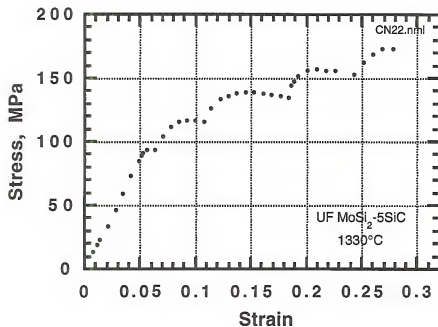


Figure A-3 True stress-strain curves of strain rate change compression tests of UF MoSi<sub>2</sub>/ 5 SiC at 1330°C, at nominal strain rates of  $2 \times 10^{-6} \text{ s}^{-1}$ ,  $4 \times 10^{-6} \text{ s}^{-1}$ ,  $8 \times 10^{-6} \text{ s}^{-1}$ ,  $1.6 \times 10^{-5} \text{ s}^{-1}$  and  $3.2 \times 10^{-5} \text{ s}^{-1}$ .



# LIST OF REFERENCES

- Aik 92a R. M. Aikin, Jr., *Scripta Met.*, **26**, 1025 (1992).
- Aik 92b R. M. Aikin, Jr, *Materials Science and Eng.*, **A155** , 121 (1992).
- Ald 67 T. H. Alden, *Acta Metall.*, **15**, 469 (1967).
- Ant 91 D. L. Anton and D. M. Shah, *MRS Symp. Proceedings*, **213**, 733 (1991).
- Ari 76 A. Arieli and A. Rosen, *Scripta Metall.*, **10**, 471 (1976).
- Aro 55 B. Aronson, *Acta. Chem. Scand.*, **9**, 1107 (1955).
- Arz 83 E. Arzt, M. F. Ashby and R. A. Verrall, *Acta Metall.*, **31**, 1977 (1983).
- Ash 69 M. F. Ashby, *Scripta Metall.*, **3**, 837 (1969).
- Ash 73a M. F. Ashby and R. A. Verrall, *Acta Metall.*, **21**, 149 (1973).
- Bag 79 J. E. Baglin, J. Dempsey, W. Hammer, F. M. d'Heurle, C.S. Petersson and C. Serrano, *J. Electron. Mater.*, **8**, 641 (1979).
- Bar 64 R. W. Bartlett, P. R. Gage, and P. A. Larssen, *Trans. AIME*, **230**, 1528 (1964).
- Bar 65 C. R. Barrett and W. D. Nix, *Acta Metall.*, **13**, 1247 (1965).
- Bas 91 A. Basu and A.K. Ghosh, *Adv. MMC for Elev. Temp. Conf. Proc.*, 41-47, TMS, Warrendale, PA, 1991.
- Ber 65 J. B. Berkowitz-Mattuck, P. E. Blackburn, and E. J. Felten, *Trans. TMS-AIME*, **233**, 1093 (1965).
- Boe 92 W. J. Boettinger, J. H. Perepezko, and P. S. Frankwicz, *Mater. Sci. Eng.*, **A155**, 33 (1992).
- Bos 92 S. Bose, *Mater. Sci. Eng.*, **A155**, 217-225 (1992).
- Bre 56 L. Brewer and O. Krikorian, *J. Electrochem. Soc.*, **103**, 38 (1956).

- Bre 80 L. Brewer (ed): Atomic Energy Review, Special issue No. 7; 1980, International Atomic Energy Agency, Vienna, Austria.
- Bur 72 B. Burton, Mater. Sci. Eng., **10**, 9 (1972).
- Can 80 R. M. Cannon, W. H. Rhodes and A. H. Heuer, J. Am. Ceram. Soc., **63**, 46 (1980).
- Car 90 D. Carter, M.S. Thesis, MIT, 1990.
- Cha 74 T. G. Chart, Metal Scienc, **8**, 344 (1974) .
- Che 64 G. B. Cherniack and A. G. Elliot, J. Am. Ceram. Soc., **47**, 136 (1964).
- Che 90 I-W. Chen and L. A. Xue, J. Am. Ceram. Soc., **73**, 2585 (1990).
- Che 92 S. C. Cheng, J. Wolfenstine. and O. D. Sherby, Metall. Trans. , **23A**, 1509 (1992).
- Cho 91a A. H. Chokshi, Mater. Sci. Tech., **7**, 469 (1991).
- Cho 91b A. H. Chokshi, Mater. Sci. Tech., **7**, 577 (1991).
- Cho 93 T. C. Chou and T. G. Neih, J. Mater. Res., **8**, 214 (1993).
- Chu 81 C. K. Chyung, Acta Metall., **29**, 159 (1981).
- Cob 63 R. L. Coble, J. Appl. Phys., **34**, 1679(1963).
- Cos 93 A. Costa e Silva and M. J. Kaufman, Scripta Metall. et Mater., **29**, 1141 (1993).
- Cos 94 A. Costa e Silva and M. J. Kaufman, Metall. Trans., **25A**, 5 (1994).
- Cos 95 A. Costa e Silva and M. J. Kaufman, Mat. Sci. Eng., **A195**, 75 (1995).
- Cot 91 J. D. Cotton, Y. S. Kim and M. J. Kaufman, Mater. Sci. Eng., **A144**, 287 (1991).
- Cro 75 F. W. Crossman and M.F. Ashby, Acta Metall., **23**, 225 (1975).
- Dec 91 S. C. Deevi, J. Mat. Sci., **26**, 3343 (1991).
- dHe 80 F. M. d'Heurle, C. S. Petersson, and M. Y. Tsai, J. Appl. Phys., **51**, 5976 (1980).

- Dol 90 C. M. Doland and R. J. Nemanich, *J. Mater. Res.* **5**, 2854 (1990).
- Dru 64 D. C. Drucker, in "High Strength Materials", ed. V.F.Zackay, Wiley, NY, 795, (1964).
- Dry 89 J. R. Dryden, D. Kucеровsky, D. S. Wilkinson, and D. F. Watt, *Acta Met.*, **37**, 2007 (1989).
- Dun 72 G. L. Dunlop and D. M. R. Taplin, *J. Mater. Sci.* **7**, 84 (1972).
- Edi 76a J. W. Edington, *Met. Technol.* **3**, 138 (1976).
- Edi 76b J. W. Edington, K. N. Melton, and C. P. Cutler, *Prog. Mater. Sci.*, **21**, 61 (1976).
- Fit 55 E. Fitzer, in *Plansee Proc.*, 56, 1955, Reutte/Tyrol, Austria.
- Fit 85 E. Fitzer and W. Remmele, *Proc. of ICCM-V*, 515, 1985.
- Fra 91 P. S. Frankwicz and J. H. Perepezko, *MRS Symp. Proceedings*, **213**, 169 (1991).
- Fri 64 J. Friedel, "Dislocations", 312, Pergamon press, 1964.
- Fro 82 H. J. Frost and M. F. Ashby, *Deformation Mechanism Maps*, Pergamon, Oxford, 1982.
- Gac 85 F. D. Gac and J. J. Petrovic, *J. Am. Ceram. Soc.*, **68**, c-200 (1985).
- Gib 92 R. Gibala, *Mat. Sci. Eng.*, **A155**, 147-58 (1992).
- Gif 73 R. C. Gifkins, *J. Australian Inst. Met.* **18**, 137 (1973).
- Gok 91 A. B. Gokhale and G. J. Abbaschian, *J. Phase Equilibria*, **12**, 493 (1991).
- Gre 70 G. W. Greenwood, *Scripta Metall.*, **4**, 171 (1970).
- Gro 69 G. W. Groves and A. Kelly, *Phil. Mag.*, **17**, 977 (1969).
- Gus 93 M. Gust, G. Goo, J. Wolfenstine and M. L. McCartney, *J. Am. Ceram. Soc.*, **76**, 1681 (1993).
- Hal 95 G. P. Halada, C. R. Clayton, H. Herman, S. Sampath and R. Tiwari, *J. Electrochem. Soc.*, **142**, 74 (1995).

- Har 67 E. W. Hart, *Acta Metall.*, **15**, 351 (1967).
- Har 92 D. A. Hardwick, P. L. Martin and R. J. Moores, *Scripta Metall.*, **27**, 391 (1992).
- Har 93 D. A. Hardwick, P. L. Martin, S. N. Patankar and J. J. Lewandowski, 665, in *Structural Intermetallics*, Proc. of Seventh International Symp. on Structural Intermetallics, Seven Springs, PA, Eds. R. Darolia, J.J. Lewandowski, C.T. Liu, P.L. Martin, D.B. Miracle and M.V. Nathal, TMS, Warrendale, PA, 1993.
- Hel 75 P. Hellman and M. Hillert, *Scand. J. Metall.*, **4**, 211 (1975).
- Hen 92 C. H. Henager, J. L. Brimhall and J. P. Hirth, *Mater. Sci. Eng.*, **A155**, 109 (1992).
- Hen 93 C. H. Henager, Jr., J. L. Brimhall and J. P. Hirth, 799, in *Structural Intermetallics*, Proc. of Seventh International Symp. on Structural Intermetallics, Seven Springs, PA, Eds. R. Darolia, J.J. Lewandowski, C.T. Liu, P.L. Martin, D.B. Miracle and M.V. Nathal, TMS, Warrendale, PA, 1993.
- Hen 95 C. H. Henager, Jr., J. L. Brimhall and L. N. Brush, *Mat. Sci. Engr.*, **A195**, 65 (1995).
- Her 50 C. Herring, *J. Appl. Phys.*, **21**, 437 (1950).
- Hig 95 K. Higashi, T. G. Nieh and J. Wadsworth, *Acta Metall. Mater.*, **43**, 3275 (1995).
- Hwa 90 C. J. Hwang and I. W. Chen, *J. Amer. Cer. Soc.*, **73**, 1626 (1990).
- Hyn 91 A. P. Hynes, M. S. Wilenski and R. H. Doremus, *Proc. American Society for Composites*, Technonic, Lancaster, PA, 591 (1991).
- Ima 92 R. M. Imaev, O. A. Kaibyshev and G. A. Salishchev, *Acta Metall. Mater.*, **40**, 581 (1992).
- Ish 90 K. Ishizaki, *Acta Metall. Mater.*, **38**, 2059 (1990).
- Ito 95 K. Ito, H. Inui, Y. Shirai and M. Yamaguchi, *Philos. Mag.*, **72**, 1075 (1995).
- Iva 67 V. E. Ivanov, E. P. Nechiporenko, V. I. Zmii, and V. M. Krivoruchko, in "Diffusion Cladding of Metals", ed. G.V. Samsonov, Consultants Bureau, Plenum, New York, 25 (1967).

- Jac 93 N. S. Jacobson, K. N. Lee, S. A. Maloy and A. H. Heuer, *J. Amer. Ceram. Soc.*, **76**, 2005 (1993).
- Jay 92 S. Jayashankar and M.J. Kaufman, *Scripta Met.*, **26**, 1245 (1992).
- Jay 93 S. Jayashankar and M. J. Kaufman, *J. Mater. Res.*, **8**, 1428 (1993).
- Jay 94 S. Jayashankar, S.E. Riddle, and M. J. Kaufman, *Mat. Res. Soc. Symp. Proc.*, **322**, 33 (1994).
- Jen 93 Y. Jeng, J. Wolfenstein and E. Lavernia, *Scripta Met.*, **28**, 453 (1993).
- Kaj 93 K. Kajihara, Y. Yoshizawa and T. Sakuma, *Scripta Metall. et Mater.*, **28**, 559(1993).
- Kaj 95 K. Kajihara, Y. Yoshizawa and T. Sakuma, *Acta Metall. Mater.*, **43**, 1235 (1995).
- Kim 90 K. Kimura, T. Hirano and M. Nakamura, *J. Mat. Sci.*, **25**, 2487 (1990).
- Koc 96 C. C. Koch and J. D. Whittenberger, *Intermetallics*, **4**, 339 (1996).
- Kuc 70 J. Kucera and B. Million, *Metall. Trans.*, **1**, 2603 (1970).
- Langd 70 T. G. Langdon, *Phil. Mag.*, **22**, 689 (1970).
- Langd 82 T. G. Langdon and P. Yavari, *Acta Metall.*, **30**, 2181 (1982).
- Langd 83 T. G. Langdon, *J. Mat. Sci.*, **18**, 1 (1983).
- Lange 80 F. F. Lange, B. Davis, and D. Clark, *J. Mat. Sci.*, **15**, 601(1980).
- Lap 93 R. Lappalainen, A. Pannikkat and R. Raj, *Acta Metall. Mater.*, **41**, 1229 (1993).
- Lat 62 J. D. Latva, *Metals Progress*, **82**, .97 (1962).
- Lon 50 R. Long, *NACA RM E50 F22*, 1950.
- Loo 88 O. B. Loopstra, W. G. Sloof, th. H. de Keijser, E. J. Mittemeijer, S. Radelaar, A. E. T. Kuiper and R. A. M. Wolters, *J. Appl. Phys.*, **63**, 4960 (1988).
- Malon 92 M. J. Maloney and R. J. Hecht, *Mater. Sci. Eng.*, **A155**, 19 (1992).

- Mal 91 S. Maloy, A. H. Heuer, J. J. Lewandowski and J. J. Petrovic, *J. Am. Ceram. Soc.*, **74**, 2704 (1991).
- Maloy 92 S. Maloy, A. H. Heuer, J. J. Lewandowski and T. E. Mitchell, *Acta Metall.*, **40**, 3159 (1992)
- Mal 95 S. A. Maloy, T. E. Mitchell, A. H. Heuer, *Acta Metall. Mater.*, **43**, 657 (1995).
- Mar 83 A. G. Marion and D. Clarke, *Acta Metall. Mater.*, **31**, 431 (1983).
- Max 49 W.A. Maxwell, NACA RM E9 G01, 1949.
- Max 52a W. A. Maxwell, NACA RM E52B06, 1952.
- Max 52b W. A. Maxwell, NACA RM E52 D09.
- Max 52c W. A. Maxwell, NACA RM E52A04, March 1952.
- Mck 92 C. G. McKamey, P. F. Tortorelli, J. H. DeVan and C. A. Carmichael, *J. Mater. Res.* **7**, 2747 (1992).
- Mes 92 P. J. Meschter, *Met. Trans.*, **23A**, 1763 (1992).
- Mou 60 G. A. Moudry, R. B. Simpson and A. Toy, AMC TR 60-5-577, July 1960.
- Nab 48 F. R. N. Nabarro, "Report of a conference on the strength of solids" , **75**, The Physical Society, London, 1948.
- Nab 67 F. R. N. Nabarro, *Philos. Mag.*, **16**, 231 (1967).
- Nak 90 M. Nakamura, S. Matsumoto and T. Hirano, *J. Mat. Sci.*, **25**, 3309 (1990).
- Nau 90 M. Nauer and C. Carry, *Scripta Metall. et Mater.*, **24**, 1459 (1990).
- Nec 73 E. P. Nechiporenko, N. S. Poltavtsev, V. L. Kapustin and Y. T. Kondratov, *Izv. Akad. Nauk. SSSR, Noorg. Mater.*, **9**, 1829 (1973).
- Now 54 H. Nowotny, E. Parthe, R. Kieffer and F. Benesovsky, *Monatsh. fur Chemi*, **85**, 255 (1954).
- Oro 47 E. Orowan, J. W. Scotland, *I.S.I* , **54**, 45 (1947).

- Pad 80 K. A. Padmanabhan and G. J. Davies, *Superplasticity*, Springer Verlag, Berlin, 1980.
- Par 65 E. Parthe, W. Jeitschko, and V. Sadagopan, *Acta Cryst.*, **19**, 1031 (1965).
- Pha 83 G. M. Pharr and M. F. Ashby, *Acta Metall.*, **31**, 129 (1983).
- Pha 89 G. M. Pharr, P. Godavarti, and B. L. Vandraager, *J. Mat. Sci.*, **24**, 784 (1989).
- Rah 86 M. N. Rahaman, Y. Boiteux, L. C. De Jonghe, *Am. Ceram. Soc. Bull.*, **65**, 1171 (1986).
- Raj 81 R. Raj and C. K. Chyung, *Acta Metall.*, **29**, 159 (1981).
- Ram 93 U. Ramamurthy, A. S. Kim, S. Suresh and J. J. Petrovic, *J. Amer. Ceram. Soc.*, **75**, 1953 (1992).
- Ray 85 G. V. Raynor and V. G. Rivlin, *Int. Metals Rev.*, **30**, 68 (1985).
- Rod 85 P. D. Rodrigo and P. Boch, *High Tech. Ceram.*, **1**, 3 (1985).
- Ros 96 E. N. Ross, P. D. Eason and M. J. Kaufman, "Processing and Fabrication of Advanced Materials V", TMS, Warrendale, PA, in press.
- Sad 92 K. Sadananda, C. R. Feng, H. Jones, *Mat. Sci. Eng.*, **A155**, 227 (1992).
- Sam 59 G. V. Samsonov, M. S. Kovalchenko, and T. S. Verkhoglyadova, *Dopovidi Akademii Nauk URSR*, **1**, 32 (1959).
- Sch 54 H. Schachner, E. Cerwenka, and H. Nowotny, *Monatsh. Chem.*, **85**, 245 (1954).
- Sch 78 J. Schlichting, *High Temp High Press.*, **10**, 241 (1978).
- Sch 83 J. H. Schneibel and P. M. Hazzledine, *J. Mater. Sci.*, **18**, 562 (1983).
- Sch 92 R. B. Schwartz, S. R. Srinivasan, J. J. Petrovic and C. J. Maggiore, *Mater. Sci. Eng.*, **A155**, 75-84 (1992).
- Sea 60 A. W. Searcy and A. G. Tharp, *J. Phys. Chem.*, **64**, 1539-42 (1960).
- She 63 P. G. Shewmon, p. 65 in *Diffusion in Solids*, McGraw Hill, New York, 1963,
- She 89 O. Sherby and J. Wadsworth, *Prog. Mater. Sci.*, **33**, 169 (1989).

- Sin 92 M. Singh, presented at the 94th Annual Meeting of the American Ceramic Society, Minneapolis, MN, 1992.
- Sri 92 S. R. Srinivasan and R. Schwarz, *J. Mater. Res.*, **7**, 1610 (1992).
- Sri 93 S. R. Srinivasan, R.B. Schwarz and J. D. Embury, *Mater. Res. Soc. Proc.* **288**, 213 (1993).
- Sto 73 R. A. Stocker and M. F. Ashby, *Rev. Geophys. Space Phys.*, **11**, 391 (1973).
- Tho 82 O. Thomas, T. G. Finstad, F. M. d'Heurle, *J. Appl. Phys.*, **67**, 2410 (1982).
- Tod 64 G. Todd and E. Parry, *Nature*, **203**, 967 (1964).
- Uma 89 Y. Umakoshi, T. Hirano, T. Sakagami, and T. Yamane, *Scripta Met.*, **23**, 87 (1989).
- Uma 90 Y. Umakoshi, T. Sakagami, T. Hirano and T. Yamane, *Acta Metall. Mater.*, **38**, 909 (1990).
- Una 90 O. Unal, J.J. Petrovic, D.H. Carter, and T.E. Mitchell, *J. Am. Ceram. Soc.*, **73**, 1752 (1990).
- Van 82 F. J. J. Van Loo, F. M. Smet, and G. D. Rieck, *High Temperature High Pressure*, **14**, 25 (1982).
- Vil 85 P. Villars and L. D. Calvert, *Pearson's Handbook of Crystallographic Data for Intermetallic Phases*, Vol. **1** and **2**, ASM, 1985.
- Wee 57a J. Weertman, *J. Appl. Phys.*, **28**, 362 (1957).
- Wee 57b J. Weertman, *J. Appl. Phys.*, **28**, 1185 (1957).
- Wee 68 J. Weertman, *Trans. ASM*, **61**, 681 (1968).
- Wee 75 J. Weertman, p. 315 in "Rate processes in plastic deformation of materials", ed. J. C. M. Lee and A. K. Mukherjee, ASM, 1975.
- Wei 83 G. C. Wei, *J. Am. Ceram. Soc.*, **66**, C111 (1983).
- Wei 92 S. M. Weiderhorn, R.J. Gettings, D.E. Roberts and C. Ostertag, *Mat. Sci. Eng.*, **A155** 209 (1992).



- Wes 64 J. H. Westbrook and D. L. Wood, J. Nucl. Mater., **12**, 208 (1964).
- Wir 66 C. D. Wirkus and D.R. Wilder, J. Amer. Ceram. Soc., **49**, 173 (1966).
- Wol 94 J. Wolfenstine, Y.-L. Jeng and E. J. Lavernia, Mater. Sci. Eng., **A189**, 257- (1994).
- Xia 92 L. Xiao and R. Abbaschian, Mater. Sci. Eng., **A155**, 135 (1992).
- Yos 90 Y. Yoshizawa and T. Sakuma, J. Amer. Ceram. Soc., **73**, 3069 (1990).
- Zen 92 J. Zeng, I. Tanaka, Y. Miyamoto, O. Yamada and K. Niihara, J. Am. Ceram. Soc., **75**, 195 (1992).

## BIOGRAPHICAL SKETCH

Sethuraman Jayashankar was born on May 29, 1966, in the village of Adivala Farm in Chitradurga District in Karnataka State, India. His formative years were spent in the mining and electricity town of Neyveli in the southern indian state of Tamil Nadu, where he obtained his primary and secondary schooling in St. Josephs of Cluny and Jawahar Higher Secondary School. Jay finished his schooling at Jawahar in 1983, securing the eighth position in the country in his high school leaving examinations held under the auspices of the Central Board of Secondary Education.


Turning down offers from medical schools in favor of an engineering education, he enrolled at the Regional Engineering College in Tiruchirapalli, from where he graduated first class with honors in mechanical engineering in 1987. After a brief stint with computational fluid dynamics at the Morgantown Energy Technology Center in West Virginia between 1987 and 1988, he entered the master's program at the University of Houston, where he majored in mechanical engineering with materials specialization.

Desirous of widening his professional horizons, Jay enrolled in the Ph.D. program in materials science and engineering at the University of Florida in 1990. Under the tutelage of Michael Kaufman, he has since pursued his interests in advanced materials development in the intellectually rich environs of Rhines Hall. In the course of his doctoral research, he has published six articles with his major advisor thus far, enumerating various aspects of structural silicide technology.

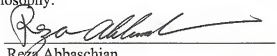
An avid fan of Carnatic classical music and a consummate practitioner of palmistry, astrology and culinary science, Jay is a member of the American Ceramic Society, The Metallurgical Society, and the Materials Research Society. A practical man

who believes in creative solutions to life's little challenges, Jay has been awarded three U.S. patents to his credit, with at least one more in the pipeline. He has also been recently elected to the Who's Who in Science and Engineering. Upon graduation, Jay plans to focus his endeavors in the successful application of science and technology to the greater betterment of humanity.

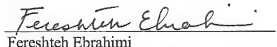
I certify that I have read this study and that in my opinion it conforms to acceptable standards of scholarly presentation and is fully adequate, in scope and quality, as a dissertation for the degree of Doctor of Philosophy.

  
Michael J. Kaufman, Chair  
Professor of Materials Science and  
Engineering

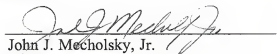
I certify that I have read this study and that in my opinion it conforms to acceptable standards of scholarly presentation and is fully adequate, in scope and quality, as a dissertation for the degree of Doctor of Philosophy.

  
Reza Abbaschian  
Professor of Materials Science and  
Engineering

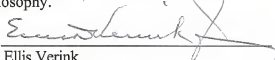
I certify that I have read this study and that in my opinion it conforms to acceptable standards of scholarly presentation and is fully adequate, in scope and quality, as a dissertation for the degree of Doctor of Philosophy.

  
Fereshteh Ebrahimi  
Associate Professor of Materials Science  
and Engineering

I certify that I have read this study and that in my opinion it conforms to acceptable standards of scholarly presentation and is fully adequate, in scope and quality, as a dissertation for the degree of Doctor of Philosophy.

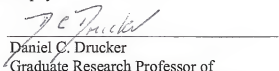
  
John J. Mecholsky, Jr.  
Professor of Materials Science and  
Engineering

I certify that I have read this study and that in my opinion it conforms to acceptable standards of scholarly presentation and is fully adequate, in scope and quality, as a dissertation for the degree of Doctor of Philosophy.



Ellis Verink  
Distinguished Service Professor of  
Materials Science and Engineering

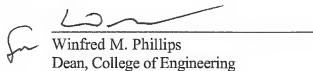
I certify that I have read this study and that in my opinion it conforms to acceptable standards of scholarly presentation and is fully adequate, in scope and quality, as a dissertation for the degree of Doctor of Philosophy.



Daniel C. Drucker  
Graduate Research Professor of  
Aerospace Engineering, Mechanics,  
and Engineering Science

This dissertation was submitted to the Graduate Faculty of the College of Education and to the Graduate School and was accepted as partial fulfillment of the requirements for the degree of Doctor of Philosophy.

December, 1996



Winfred M. Phillips  
Dean, College of Engineering

---

Karen A. Holbrook  
Dean, Graduate School